

Circuits and Systems for Integrated Metal-Oxide Sensors Towards Artificial Olfaction

June 2023

Yohsuke Shiiki

Circuits and Systems for Integrated Metal-Oxide Sensors Towards Artificial Olfaction

Yohsuke Shiiki

Graduate School of Science and Technology

Keio University

A thesis submitted for the degree of Ph.D. in Engineering

June 2023

Circuits and Systems for Integrated Metal-Oxide Sensors
Towards Artificial Olfaction

All rights reserved by Yohsuke Shiiki. June 2023.

This thesis is dedicated to my parents.

Abstract

The realization of artificial olfaction has been pursued for decades of years. While chemical analysis of gas molecules is feasible, achieving the technology to replace the mammalian nose with an artificial nose capable of portable, low-energy, real-time recognition of over 10,000 odors poses various research challenges. Unlike other sensory organs such as vision or hearing, olfaction possesses hardware-related challenges that make its realization difficult. As the hardware platform, a metal-oxide sensor is highly promising because they have the desirable characteristics of low cost, integrability, and high sensitivity. To treat metal-oxide sensors as an electronic nose, circuits and systems are indispensable to maximize the utilization of the sensors by controlling the integrated sensors and reading their responses. In this study, techniques of sensor modeling, sensor integration, and sensor emulation are focused on from the perspective of circuits and systems. The research on sensor materials and the fabrication of the sensor chips were conducted with the collaboration and support of Yanagida Laboratory at the University of Tokyo, our research partner. A final goal of this research is to make the hardware of an electronic nose using integrated sensors. The integrated sensors are supposed to be composed of several types of sensors and operated under different temperature conditions for each sensor. The operating temperatures are intentionally varied to emulate different types of sensors by the same type of sensors.

In order to subdivide the challenges in circuits and systems, two types of sensor chips are fabricated and tested. A self-heated metal-oxide sensor is a promising sensor as it consumes a small amount of power to control the sensor's

temperature. A new compact model of the self-heated sensor is developed to estimate the sensor's conductance behavior and design an elaborated interface circuit in Chapter 3. Output from the simulation model and experimental data from a fabricated self-heated sensor are compared for verification. Although challenges remain in reproducing sensor resistance affected by drift in an inert gas, we have successfully replicated the response characteristics of the sensor to the target gas.

The integration of sensors is a challenging task for both sensor designers and circuit designers. To decrease the number of accessing electrodes to integrated metal-oxide sensors, a matrix array of the sensors is designed in a chip. The sensor array is also designed in a cross-point structure to make its fabrication cost low. A critical problem for the readout circuit is sneak-path current, which interferes with accurate sensor measurement. Since conventional interface circuits to suppress sneak currents were evaluated with a smaller array, the simulation shows that readout accuracy largely degraded. To address the problem, a calibration method is proposed to eliminate the effects of op-amp's nonidealities in Chapter 4. Furthermore, we propose an amp-less readout method. In contrast to the conventional interface circuit, the proposed method does not suppress sneak currents. Instead, they control the flowing currents, and each sensor resistance is calculated with a matrix equation. Two readout methods are designed based on the idea: "Sneak-path-controlled readout" and "Accurate sneak-path-controlled readout". Their readout accuracy is systematically evaluated with simulations, and we achieve around 1% of readout error for a 32×32 sensor array.

It is possible to acquire different sensing responses with the same type of metal-oxide sensor by operating them at different temperatures. Sensory emulation is an attractive technique to integrate various sensors in a chip. An interface circuit is required to precisely control temperature. Since the temperature is controlled by a self-heating effect, the circuit monitors the Joule-heating of the sensors. Besides, the sensor resistances are dynamically changed by surrounding gas molecules and temperature, and the sensors should be

operated simultaneously. It is also important to minimize the circuit scale and power consumption, as the technique is applied to an electronic nose. To fulfill all the requirements, we created a new measurement system for the self-heated metal-oxide sensor, called “constant-power and pulse-measurement system for a self-heated sensor array” in Chapter 5. The performance of the implemented circuit is evaluated by measurements. To verify that the emulation is functioning properly, an array of 16 self-heated sensors is fabricated in a sensor chip and tested with a reactive gas. The experimental results are compared with other experimental results using conventional continuous-heating measurements. Although measured sensitivity decreases, the sensor temperature dependency can be observed from the pulse-heating measurement, and power consumption per sensor is successfully suppressed.

The techniques of sensors, circuits, and systems mutually influence the overall performance. In addition, setting clear target specifications for interface circuits are difficult because the sensors are in ongoing development. However, the research and development of the three core aspects are suitable as a starting point for circuits and systems to realize artificial olfaction. Furthermore, conducting them in parallel with sensor research and development enables circuit-related challenges and findings feedback to the sensor’s developers.

Acknowledgements

I would first like to thank my thesis advisor Prof. Hiroki Ishikuro. He guided and encouraged me to be professional and do the right thing even when the road got tough. Without his guidance and persistent help, this thesis would not have been possible.

I also would like to give my thanks to the three professors who have reviewed this thesis; Prof. Nobuhiko Nakano, Prof. Takeshi Yanagida, and Prof. Kentaro Yoshioka. Their advice was practical and improved the readability of this thesis.

Next, I would also like to express my deep and sincere gratitude to Prof. Takeshi Yanagida, and his research group members Prof. Tsunaki Takahashi, and Prof. Kazuki Nagashima at the University of Tokyo. During my time working with them, I received invaluable guidance, which aided this research. Without their kind provision and warm encouragement, this research would not be worthy to support this thesis successfully. I express immense gratitude to his students, Zeng Hao, Haruka Honda, and Shintaro Nagata for their genuine support throughout this work.

During the early stage of my research, Prof. Ken Uchida at the University of Tokyo, and his research member Prof. Takahisa Tanaka gave me insightful comments and suggestions when we exhibited our collaborative works. This was a valuable experience to create a great demonstration. I cannot thank both of them enough.

I would like to express my special gratitude to Prof. Takayasu Sakurai at the University of Tokyo and his research members Tokihiko Mori and Mai Kuroda. It was a remarkable experience to join Trillion-Node Study as a member of the

development team. I enjoyed solving a lot of practical problems for IoT systems and I had wonderful experiences discussing how to spread IoT-platform hardware around the world.

I must offer my esteem to Prof. Masahiro Yukawa at Keio University. He connected me to the opportunity to enter Imperial College London as a visiting student. Without this chance he offered me, I would have been without the valuable research experience. I would also express my gratitude to Prof. Danilo Mandic at Imperial College London for accepting me as a member of his research group. He kindly instructed me and gave thoughtful advice about signal processing and research direction. I also would like to give special thanks to Harry Davies and his colleagues for providing me with his research in signal processing, which broadened my perspective for my own research.

Special thanks to Prof. Kentaro Yoshioka and his students Yuki Hayakawa and Ryo Suzuki at Keio University, and Takami Sato at University of California, Irvine. I had great experiences by joining with LiDAR security subject. I could gain an alternative perspective of science technology through this research field, and I am pleased to have used this field to expand my knowledge and understanding.

Without the mutual encouragement of Shuya Nakagawa, I would not have had the same motivation to endure to the end of this academic career. And to my Sensor Team: Kohei Tatehara, Shoo Saga, Yuya Fuketa, and Nobuhiro Toneyama, I am appreciative of their assistance in the Ishikuro laboratory. I also offer my appreciation to other members of the laboratory, Yi Tan, Chia-Wei Pai, Peter Toth, Kaoru Yamashita, and Masafumi Matsuura and for supporting my Ph.D. activities.

Finally, I am extremely grateful to my parents for their love, prayers, caring and sacrifices in educating, and preparing me for my future.

Contents

Abstract	v
Acknowledgements	ix
Contents	xi
List of Figures	xv
List of Tables	xxi
Chapter 1 Introduction	1
1.1 Overview of an Electronic Nose	1
1.1.1 Olfactory Application.....	3
1.1.2 Electronic Nose Hardware	5
1.2 Research Goal	12
1.3 Thesis Outline	14
Chapter 2 Overview of Integrated Sensors and Interface Circuits	17
2.1 Integration of Metal-Oxide Sensors	17
2.1.1 Cross-Point Resistive Sensor Array	18
2.1.2 Circuits for a Cross-Point Resistive Array	20
2.2 Self-Heated Metal-Oxide Sensor.....	24
2.2.1 Temperature Dependency	25
2.2.2 Temperature Modulation System	26
2.2.3 Low-Power System for the Integrated Self-Heated Sensor....	29

Chapter 3 Compact Model of a Metal-Oxide Sensor	33
3.1 Developed Sensor.....	33
3.2 Compact Modeling	35
3.3 Experiment and Simulation Results	37
Chapter 4 Readout Circuits for a Cross-Point Resistive Array	39
4.1 Op-Amp Output Impedance Effects	39
4.1.1 Feedback Error Evaluating Model.....	41
4.1.2 Feedback Error Analysis.....	44
4.2 Calibration by Op-Amp Nonidealities	46
4.2.1 Calibration	46
4.2.2 Simulation Results	48
4.2.3 Prototype Design.....	53
4.3 Readout Methods without Op-Amps	55
4.3.1 Readout Scheme	56
4.3.2 Sneak-Path-Controlled Readout	58
4.3.3 Calculation of Resistance	59
4.3.4 Calibration of Switch Resistance	61
4.3.5 Accurate Sneak-Path-Controlled Readout	63
4.3.6 Simulation Results	66
4.4 Demonstration.....	71
4.4.1 Designed PCB	72
Chapter 5 System for Integrated Self-Heated Sensors	77
5.1 Circuit Design.....	78
5.1.1 Thermal Control Circuit	79
5.1.2 Readout Circuit	80
5.1.3 Overall Circuit Design.....	81
5.2 Operation Flow	86
5.3 Measurements	92
5.3.1 Developed PCB	93
5.3.2 Readout Accuracy	93

5.3.3 Input Power Accuracy	96
5.3.4 LC Filter	101
5.3.5 PID Control.....	101
5.3.6 Power Consumption	102
5.4 Experimental Results.....	105
5.4.1 Setup.....	105
5.4.2 PID Control Monitor	106
5.4.3 Sensor Measurement.....	108
Chapter 6 Conclusion	115
6.1 Thesis Summary	115
6.2 Future Works	117
Reference	119

List of Figures

Figure 1.1	Simple illustration of a biological nose.	2
Figure 1.2	Schematic diagram of the experimental low-cost electronic nose (a) and picture of the actual system (b) (OD, Outer Diameter; ID, Inner Diameter). Reproduced from [21].	5
Figure 1.3	System diagram of the multi-channels electronic nose module. Reproduced from [53].	7
Figure 1.4	The 3D structure of the proposed nose-on-a-chip. Reproduced from [29].	9
Figure 1.5	Chip micrograph of the nose-on-a-chip. Reproduced from [62].	10
Figure 1.6	Conceptual image of hardware of proposed electronic nose.	12
Figure 1.7	The research structure.	13
Figure 1.8	Graphical outline of this thesis.	14
Figure 2.1	A cross-point structure sensor and its graphical image to react various types of gases.	18
Figure 2.2	Equivalent circuit of the sensor chip.	19
Figure 2.3	Fundamental readout circuits for a resistive array called Voltage Feedback Methods (VFM) and Zero Potential Methods (ZPM).	21
Figure 2.4	Large current load from an op-amp.	23
Figure 2.5	Expected sensor reaction depending on sensor's temperature.	25

Figure 2.6 Simulated sensor response.	26
Figure 2.7 Temperature control by self-heating.....	28
Figure 2.8 Conventional continuous heating operation and the proposed sensor operation.....	30
Figure 2.9 Simple illustration of resistance change of the self-heated sensor.	31
Figure 3.1 (a) Microscope image of the self-heated sensor device. (b) I-V curve of the self-heated sensor.....	34
Figure 3.2 Thermal simulation results run in COMSOL	35
Figure 3.3 Self-heated metal-oxide sensor model	35
Figure 3.4 Comparison of the static responses between the simulated values with the fitting parameters and experiment data.	36
Figure 3.5 Comparison of the dynamic responses between the simulated values with the fitting parameters and experiment data.	38
Figure 4.1 A op-amp model to analyze a readout error (a) The sneak currents due to finite gain and output impedance of an op-amp. (b) A simplified circuit. The resistors causing readout error are represented by the three resistors, R_Y and R_X and $R_{i,j}$	40
Figure 4.2 Feedback voltage Error of VF-NSE method, in which the reference resistance is parameterized. Dashed line indicates example numbers.	42
Figure 4.3 Read error of VF-NSE method, in which the reference resistance is parameterized. Dashed line indicates example numbers.....	43
Figure 4.4 Readout error of VF-NSE method, in which the size of matrix array is parameterized. Dashed line indicates example numbers.	44
Figure 4.5 Dependency of feedback voltage error on op-amp output voltage. The negative voltage is defined as $-n \cdot V_{REF}$. Dashed line indicates example numbers.....	45

Figure 4.6 Model to calculate a combined conductance in the Y group.....	46
Figure 4.7 An equivalent circuit to calculate the array resistance removing the effects of a finite gain and an output resistance of the op-amp.....	48
Figure 4.8 Readout error when calibration applied to resistance distributed array comparing with the non-calibrated VF-NSE method.....	49
Figure 4.9 Readout error comparison with the non-calibrated VF-NSE method.	50
Figure 4.10 Readout error dependency on an op-amp offset voltage.	51
Figure 4.11 Prototype system (a) PCB (b) Gas Sensor chip.	52
Figure 4.12 (a) Measured positions in the developed sensor chip (b) A heatmap graph of measured sensor resistances.....	54
Figure 4.13 Circuit diagram with i -th row and j -th column selected.....	56
Figure 4.14 Flow of acquiring resistance.	57
Figure 4.15 Sneak-path-controlled circuit.....	59
Figure 4.16 Simplified circuit with resistors with no sneak current removed .	60
Figure 4.17 Simplified circuit considering switch resistance.....	62
Figure 4.18 Case study with different resistances on selected column and selected row. The equivalent circuit indicates that the bias voltage applied to the sensor differs on selected row and column electrodes.	63
Figure 4.19 Circuit for accurate control of readout and (b) equivalent circuit.....	65
Figure 4.20 Comparison of readout accuracy when SPCR is used. RMSE is improved by the switch-resistance-calibrated readout. (a) Simulation results obtained with parameterized switch on-resistance	

and (b) Simulation results obtained with parameterized switch off-resistance.	67
Figure 4.21 Degradation of accuracy of SPCR due to ADC quantized error. Max. input voltage of ADC is 3.3V when VREF is set to 3.3 V....	68
Figure 4.22 Tested resistance patterns: pattern A, generated by the randn() function in MATLAB, is normally distributed; pattern B is an image converted from the picture of a person's face; pattern C contains the same sensor resistances as pattern B, but it is randomly rearranged. Pattern D contains the same sensor resistances as pattern B, except the resistances are sorted. The histograms for each pattern are shown.	69
Figure 4.23 Block design of a developed system	72
Figure 4.24 Pre-complementation	73
Figure 4.25 Schematic of a designed PCB.....	74
Figure 4.26 A developed PCB and a sensor chip	75
Figure 4.27 Heatmap of measured resistances with SPCR	75
Figure 5.1 Thermal control circuit.	79
Figure 5.2 Readout circuit.	80
Figure 5.3 Overall circuit design for a constant-power and pulse-measurement system.....	82
Figure 5.4 Schematic of constant-power and pulse-measurement system.	85
Figure 5.5 Operation sequence.....	86
Figure 5.6 Functional block.....	87
Figure 5.7 Idle state, which is right after the V_{in} is inputted.	88
Figure 5.8 Circuit for the first readout operation.....	88
Figure 5.9 Example of power rearrangement.....	89

Figure 5.10	PMIC wake-up.....	90
Figure 5.11	Heating operation.	91
Figure 5.12	Readout operation.....	91
Figure 5.13	PCB of constant-power and pulse-measurement system with dummy sensors mounted.....	92
Figure 5.14	dummy sensor's resistances and their positions.	93
Figure 5.15	Histograms of output values of ADC in the readout circuit.	94
Figure 5.16	Error evaluation in the readout circuit.....	95
Figure 5.17	Circuit configuration to evaluate current sensing.....	96
Figure 5.18	Current sensing accuracy.	97
Figure 5.19	Circuit configuration to evaluate specification of controlling output voltage.	98
Figure 5.20	Accuracy of output voltage of a DC-DC converter configured by DAC.	99
Figure 5.21	Noise level of DC-DC output and LC filter output.....	100
Figure 5.22	Block design of PID controller.....	101
Figure 5.23	PID controller operation	102
Figure 5.24	Sensor connection.....	106
Figure 5.25	Experimental setup of PCB.	107
Figure 5.26	Overall experimental setup.	108
Figure 5.27	Measurement of monitoring the PID controller with an actual sensor.	110
Figure 5.28	Measured resistance by pulse-heating measurement.....	111
Figure 5.29	Comparison results between the proposed pulse measurement and continuous measurement.....	113

Figure 5.30 Sensor responses measured by the constant-power, pulse-heated measurement. 114

List of Tables

Table 1.1 Application examples of an electronic nose.....	4
Table 4.1 Readout error with SPCR	70
Table 4.2 Readout error with ASPCR	70
Table 5.1 Possible sensor states in measurement operation.....	81
Table 5.2 Initial parameters used for resistance calculation.....	94
Table 5.3 Fitted parameters for resistance calculation.....	94
Table 5.4 Expected power-consumption during each operation according to IC data sheets.....	103
Table 5.5 Results of power consumption measurements.	104
Table 5.6 Sensors' information used in the experiment about position, resistance, and target power.....	109

Chapter 1

Introduction

Complete replacement of a biological nose is a desired technology but has not been realized although many researchers have attempted it for decades. By reviewing the mechanism of a biological nose and the history of an artificial nose, it is possible to gradually reveal the technological constraints to achieve artificial olfaction. This chapter describes applications and hardware implementation of electronic noses, and our research goal is shared. This thesis structure is also given at the end of this chapter.

1.1 Overview of an Electronic Nose

Artificial olfaction is a measuring system that mimics biological nasal system. At first, efforts to realize it were made to discriminate various gases. In 1961, the early development of artificial olfaction was reported [1], which detects odorants using a mechanical nose. The early developments did not have intelligent functions to classify different odorants [2]. According to a review paper [3], the concept of an intelligent chemical sensor array emerged by Persaud *et al.* at Warwick University in the UK [4] in 1982, and Ikegami *et al.* at Hitachi in Japan in 1985 [5], [6]. Then around late 1980s, the term ‘electronic nose’ appeared as CMOS and other semiconductor technologies have been attractive for many researchers. Now that artificial olfactory systems have been studied over 40 years.

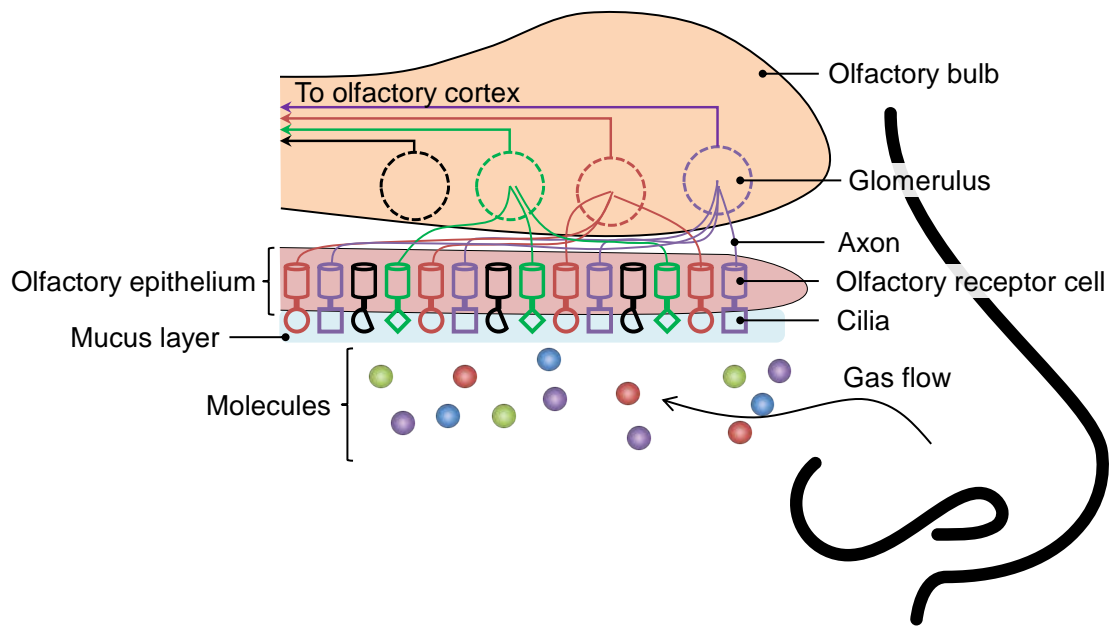


Figure 1.1 Simple illustration of a biological nose.

However, the progress of development is slow compared with other biomimetic technologies. The significant difference is the complexity of the way of recognition. For example, human visual information is collected by three types of receptors, that is, red, green, and blue. Light power received by each receptor exactly is visual information. On the contrary, it is necessary to detect millions of different odorants for most mammalian species to survive. Figure 1.1 shows a nasal model of a human. The olfactory epithelium contains millions of olfactory sensory neurons (OSN), where specific odor molecules cause stimulation. The olfactory neurons extend cilia into a nasal lumen to detect gas molecules dissolved in the nasal mucus. The olfactory cortex is a part of the brain to process electrical signals from the olfactory neurons. The chemical stimulation with molecules is converted to electrical stimulation through the OSN. Olfactory receptor (OR) cells work as a sensor. Each OR cell expresses an exclusive OR gene, and various OR cells scatter in the olfactory epithelium. The axons from the same kind OR cell are gather in an identical glomerulus. Humans have around 400 types of functional receptor genes while mice have about 1,000 [7]. The number of types of functional receptors relates to the ability of olfaction. It is essential that a single OR cell can react with multiple types of molecules, and

vice versa. It means that different odorants are classified from different combinations of ORs. Therefore, humans and other mammals can detect 10,000 or more smells [8], [9].

Even though many gas sensors are commercialized, state-of-art gas sensors are not as good as mammalian noses which have balanced specifications of integration, long-term stability, molecular selectivity, sensitivity, and so on. Moreover, many mysteries remain about how mammals recognize smells in their brain. Many researchers have studied to create biomimetic technologies for noses. To realize artificial olfaction, electrical implementation has been widely chosen for its portable, low-cost, and easy hands-on features [10], [11]. Most electronic noses consist of main three parts: a sensor array, sensory circuits, and gas recognition. This article mainly focuses on sensory circuits with touching sensor techniques. It is noted that “sensory circuits and systems” means the combination of sensor and circuit techniques in this paper.

1.1.1 Olfactory Application

A remarkable work in the early stage of the electronic nose was reported in 1982 by K. Persaud *et al* [4]. They used three gas sensors to detect four different molecules. Their assumptions are the basis of a present electronic nose: there is no requirement for odor transducers; and the ratio of the signals from the transducers can be processed to identify an odor. Up to the present time, a wide variety of usage of electronic noses has emerged, such as healthcare, food management, environmental monitoring, and so on. Unlike gas detection systems using a single gas sensor [12]–[15], an electronic nose can detect complex gas mixtures. For example, L. Dutta *et al.* proposed a hand-held tea flavor estimation system using four gas sensors [16]. The four sensors mainly react to 8-type molecules contained in Assam crush, tear, and curl (CTC) tea. The molecules are related to tea grades, and they classified tea samples into different grades from sensor responses and artificial neural networks (ANNs). In addition to this

example, there are a variety of applications as listed in Table 1.1. Classification algorithms are required in each application since most gas sensors react with multiple types of molecules, and their target molecules overlap intricately. They show that electronic noses are becoming practical in many ways. To our knowledge, a portable and commercial electronic nose uses at most around 32 sensors. Compared to a human having about 400 types of functional genes, the number of sensor integration is small. It is obvious that the ability to distinguish multiple odors is limited to the number. Therefore, their application demands specific sensors and classification. However, a single mammalian nose can be used for general purposes, with detecting numerous odors.

Table 1.1 Application examples of an electronic nose.

Application		Work
Food	Tea flavor estimation	[16]–[18]
	Alcohol classification	[19]
	Fruit classification	[20]
	Different food classification	[21]
	Food freshness monitoring	[22]–[27]
Health	Diseases detection	[28]–[33]
	Drugs classification	[34]
Environment	Outdoor gas monitoring	[35]–[37]
	Indoor gas monitoring	[38]
	Car exhausting gases detection	[39], [40]
	Fire detection	[41]
	Explosion gas detection	[42], [43]

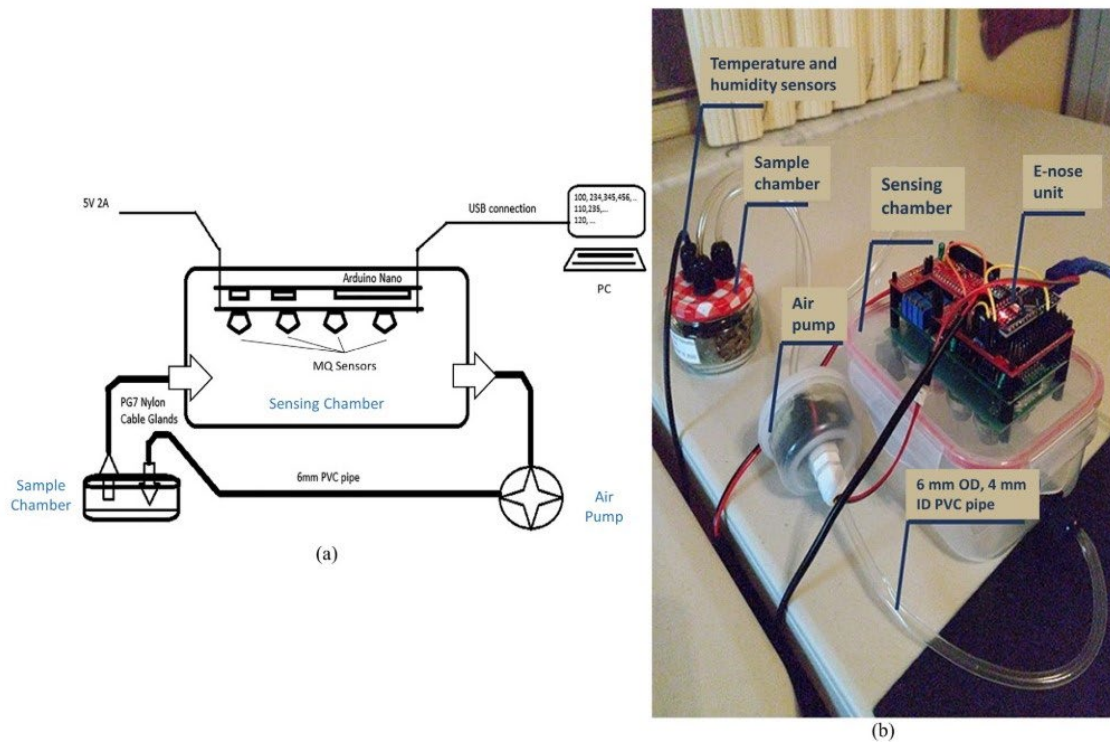


Figure 1.2 Schematic diagram of the experimental low-cost electronic nose (a) and picture of the actual system (b) (OD, Outer Diameter; ID, Inner Diameter). Reproduced from [21].

1.1.2 Electronic Nose Hardware

In many electronic nose applications, commercial and discrete gas sensors have been embedded because most of the sensors are cheap and small. In [21], different foodstuffs were sensed by tin dioxide MQ series gas sensors. They mounted 8 sensors on a printed circuit board (PCB), and the size of the system was apparently around postcard size as shown in Figure 1.2. On the contrary, [37] mounted six metal-oxide gas sensors from Figaro Inc. (Osaka, Japan). They developed a portable measurement device of an electronic nose including sensors, a microcontroller, an LCD panel, an air pump, and a sensor chamber. The microcontroller measured the sensor responses and sent the acquired value to a PC to collect and process the data. As a practical application, the device monitored an indoor air quality of an animal farm. Not limited to this research, the Figaro gas sensors have been widely utilized in many studies [4], [16], [25].

As alternative discrete gas sensors, [41] reported a fire detection system using eight metal-oxide gas sensors from FIS Inc. (Osaka, Japan). They created a compact instrument box containing the gas sensors, gas pathway mechanics (inlet/outlet valves, tubes). These discrete gas sensors are useful because the company has offered a diverse lineup of metal-oxide gas sensors and ensured ease of hands-on experience. However, there is a limitation to the decrement of the size of an electronic nose when it comes to integrating various sensors. As a portable instrument of an electronic nose, some commercial devices have appeared. In [32], Cyranose 320 (Sensigent®, California, USA) was used to classify volatile organic compounds (VOCs) in urine. 32 chemical sensors, including conductive polymer and carbon nanotube, were contained in a handheld device. The device has been widely applied in various applications, such as medical applications [28], [33], and food industrial applications [27]. PEN-3 or PEN-2 (Airsense Analytics, Schwerin, Germany) is an alternative portable electronic nose, which contains ten different metal-oxide thick film gas sensors [44]. A. Nake *et al.* monitored VOCs at five different outdoor locations of a wastewater treatment plant and compared performances between metal-oxide sensors (PEN-2) and conducting polymer sensors (Cyranose 320) [36]. Those performances of gas discrimination were compared by the results of principal component analysis (PCA). They concluded that the metal-oxide sensors are applicable for their usage. Other works reported that different tea flavors were successfully discriminated by using PEN-2/PEN-3 [17], [18].

Apart from the implementation of discrete gas sensors, efforts towards the miniaturization of an electronic nose have been made for decades using a semiconductor manufacturing process. In 1994, J. V. Hatfield *et al.* reported an application specific integrated circuit (ASIC) chip using BiCMOS technology to measure sensor resistance. They developed 20 conducting polymer sensors, and the sensors were connected to the chip on PCB. In 1999, M. Cole *et al.* developed a CMOS current drive chip using the Alcatel Mietec 2.4 μm CMOS process [45]. The circuit was implemented to measure six conducting polymer sensors, which

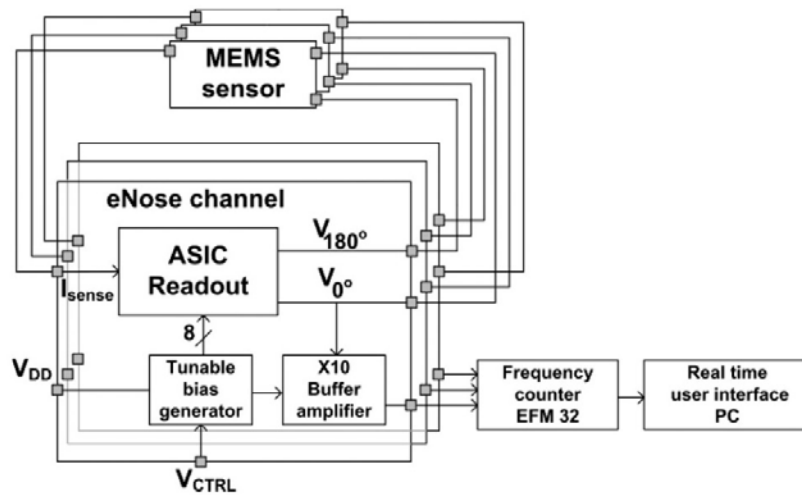


Figure 1.3 System diagram of the multi-channels electronic nose module. Reproduced from [53].

were fabricated with a CMOS-compatible process by J.W. Gardner *et al* [46]. Five years later, J. García-Guzmán, *et al.* designed and simulated a chip of an interface circuit for two polymer sensors [47]. The chip was basically designed to sense the gas presence and concentration and control the temperature of two gas sensors. The designed chip used an Alcatel Microelectronics 0.7 μm CMOS technology, and the chip size was 3,300 μm \times 3,750 μm . They confirmed a ratiometric configuration of the sensory interface circuit increased the readout performance under the variations of temperature, humidity, and sensor resistance in simulations. In addition, they proposed a measurement technique that applied pulsed bias voltage to the sensor alternately in the forward and reversed directions to avoid polarization effects on the sensor. In 2010, they reported that duo-type and carbon black/polymer sensors were successfully deposited on the fabricated chip [48]. Even though only two sensors were mounted on a chip, the system discriminated between toluene and ethanol with a notable performance of the common mode rejection of humidity response.

From the perspective of miniaturization with low-power operation and high sensitivity, an electronic nose using CMOS-compatible micromechanical resonant sensors has also attracted many researchers [49]. The resonant sensors

change an oscillating frequency when the target molecules are adsorbed. In 2002, C. Hagleitner *et al.* embedded mass-sensitive microsensors into a single-chip gas detection system with two different sensors [50]. The chip were fabricated in 0.8 μm CMOS technology and contained three (mass-sensitive, capacitive, and calorimetric) sensors, which sensing principles were different. Therefore, three interface circuits for each sensor were developed with analog-to-digital converters (ADCs) and a digital serial interface. From the analysis of measured data using three different sensors, different molecular properties or different aspects of the coating molecules were found [51]. Their demonstration of the monolithic CMOS gas microsystem is a unique achievement compared to other gas sensory systems. In contrast, resonant sensors can own different sensitivities by coating different polymers. In [52], an array of two identical resonant sensors was implemented. They created a prototype PCB where a chip containing two different polymer-coated resonators was mounted. Although its interface circuit was not implemented on the prototype, it showed the capability to distinguish gases. J. Pettine *et al.* proposed an oscillator-based readout circuit for three polymer-coated MEMS resonators in [53], [54] as depicted in Figure 1.3. The readout circuit was designed to measure a resonant frequency of MEMS sensors in 0.25 μm CMOS technology and the chip size was 330 μm \times 217 μm . They measured the static power consumption of the readout circuit, and it was 1.35 mW/channel. Even though low-power readout was achieved in those systems, the number of measured sensors was limited to a few sensors. Additionally, since the interface circuit needs to read a frequency shift for resonant sensors, it is challenging to integrate tens or hundreds of sensors in a small CMOS system. In 2021, A. Murray *et al.* implemented a 16-channel oscillator-based sensor array [55]. Although they achieved high sensitivity using three different polymer coatings, an independent oscillator was equipped to drive the sensors.

A CMOS process has taken large advantage of circuit integration. The circuit has an important role in an electronic nose as it corresponds to synapses in a biological nose. Moreover, CMOS-compatible sensors are attractive for small-

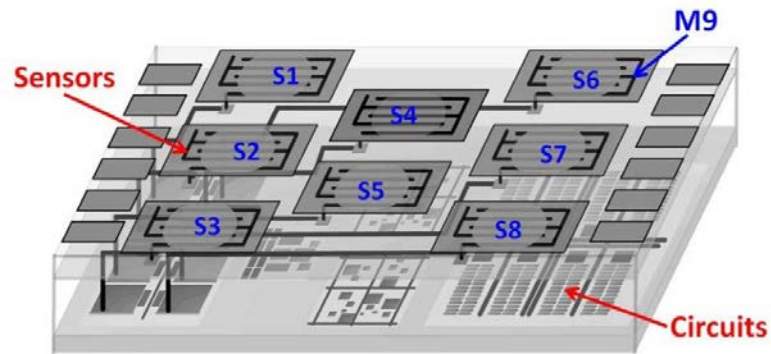


Figure 1.4 The 3D structure of the proposed nose-on-a-chip. Reproduced from [29].

size and highly integrated electronic noses. On-chip sensors were fabricated on a CMOS circuit by K. T. Tang and R. M. Goodman in 2001 [56]. Unlike other works which integrated only sensing circuits, they developed a nose chip that included the sensor stage, signal-processing core, database stage, and classifier stage. The chip was fabricated by 1.2 μm 2-poly 2-metal (2P2M) process at MOSIS and its size was 2,117 $\mu\text{m} \times 2,117 \mu\text{m}$. Three different carbon black-organic polymer off-chip sensors were measured to evaluate the performance of the chip. Their results showed that eight different odors were distinguished. They measured the power dissipation of the chip in their further work in 2006 and they found that 7.6 mW was consumed when the sensor resistance changed. In 2011, K. T. Tang *et al.* implemented another signal-processing chip for an electronic nose using TSMC 0.18 μm 1P6M CMOS technology [57]. They classified three different odors with eight multi-walled carbon nanotubes (MWNTs) conducting polymer sensors [58]. The signal processing chip was 2,058 $\mu\text{m} \times 1,952 \mu\text{m}$ and a chip of the sensor array was 34 mm \times 20 mm. The signal-processing chip included an interface circuit, ADC, memory, and microprocessor. A k -nearest neighbor algorithm was executed in a microprocessor. Low-power operation at 2.81 mW was achieved in total with the 10 MHz system clock and 1.8 V supply voltage. In 2014, S.-W. Chiu, et al. reported a fully integrated nose-on-a-chip for the diagnosis of ventilator-associated pneumonia [29]. Eight different polymer sensors were implemented on the chip which had a sensory interface, a learning

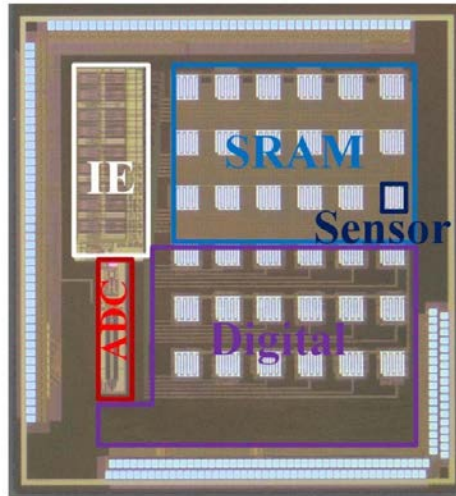


Figure 1.5 Chip micrograph of the nose-on-a-chip. Reproduced from [62].

kernel of continuous restricted Boltzmann machine (CRBM), and a RISC-core with low-voltage SRAM as shown in Figure 1.4. The chip was fabricated using TSMC 90 nm 1P9M CMOS technology, and the chip area was $3,254 \mu\text{m} \times 3,223 \mu\text{m}$, which consumed only 1.27 mW at 0.5 V. The same research group used the nose-on-a-chips in different applications [59]–[61]. Their recent work [62] presented that they developed a fully integrated nose-on-a-chip with 36 on-chip sensors. The chip was designed with a 180 nm CMOS process and consumed 2.6 mW at 1 V operation.

There is another approach to implement nasal hardware using a bio-inspired computation, called spiking neural network (SNN). SNN is one of the neural networks mimicking biological synapses. There are many achievements for it since it was first proposed in 2006 [63]–[69]. Most works of SNN-based electronic noses focus on classification algorithms. An overview of SNN-based olfaction is summarized in the review paper [70]. However, the recognition ability is clearly limited if small numbers of sensors are available. To our knowledge, the number of utilized gas sensors is at most 32 [64]. Additionally, there is no significant difference to create a sensor array compared to other

methods. Therefore, we defer the explanation of SNN-based hardware to other references as it deviates from this thesis.

As explained above, many researchers have focused on size and power consumption. However, the commercial discrete gas sensors and portable electronic nose have a limit to decrease the size of the system while the implementation as an ASIC chip has constraints on the number of integrated sensors. It is surely a critical problem to realize an electronic nose because most mammals have about ten times larger number of receptor cells. Furthermore, the selection of material for gas sensors is significant for some applications. According to a review article on nanostructure-based gas sensors [71], sensors that are heated by a microheater or self-heating have better sensitivity than electrochemical or calorimetric sensors. Considering nanoscale sensors, a polymer gas sensor that is operated at room temperature is not suitable because of the difficulty in the microfabrication of the polymer. Furthermore, polymer materials suffer from larger deterioration over time than metal-oxide materials. To earn sensitivity, small size, and low-power consumption at the same time, it is mandatory to consider sensor characteristics, CMOS implementation, and the most effective operating method.

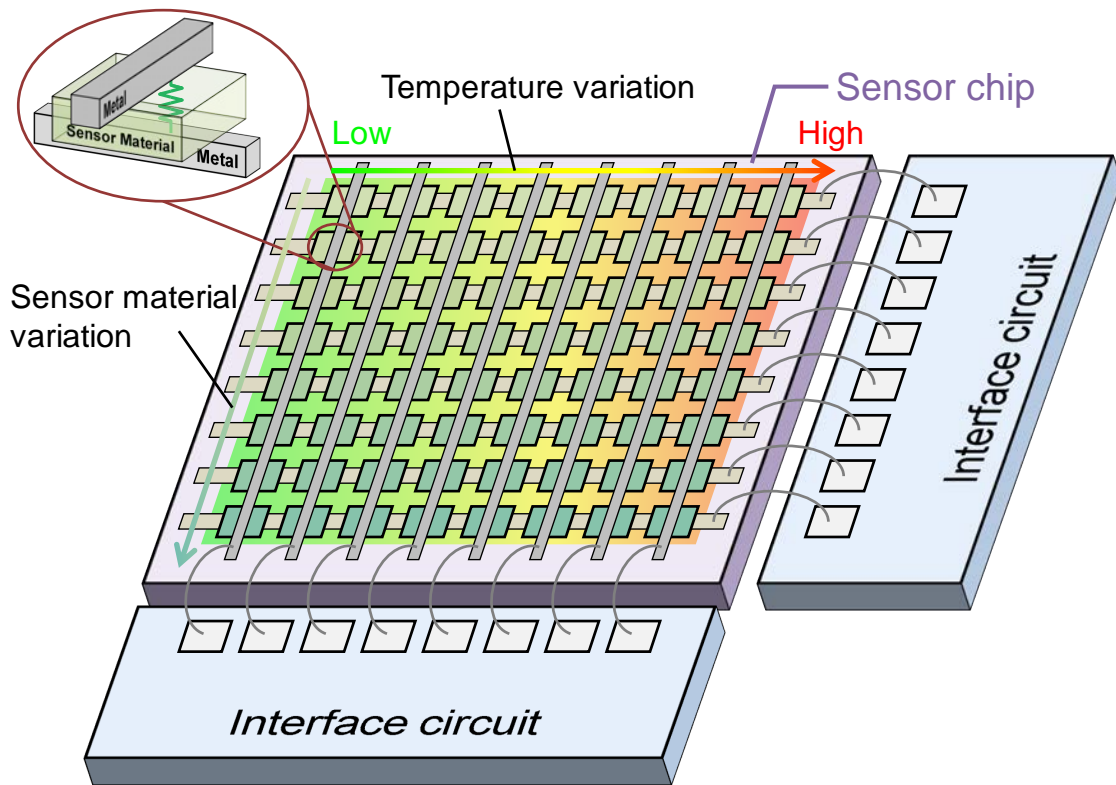


Figure 1.6 Conceptual image of hardware of proposed electronic nose.

1.2 Research Goal

To realize an electronic nose with the same discrimination ability, sensory and circuit techniques are focused. While metal-oxide sensors have the advantages of small size, low cost, and integration, there are challenging obstacles to data acquisition from many sensors. A conceptual image is shown in Figure 1.6. The sensors are arranged in a matrix shape. The sensor response appears in resistance change. The temperatures of the sensors are distributed, as the metal-oxide sensor has temperature dependency. While the operating temperature is controlled, the sensor resistances are measured by the interface circuits. To realize the system, both the sensor materials and sensory interface have been researched. The sensor material has been researched at Yanagida Laboratory at the University of Tokyo and they have developed a large integrated sensor array and self-heated metal-oxide sensors, which sensors are utilized in

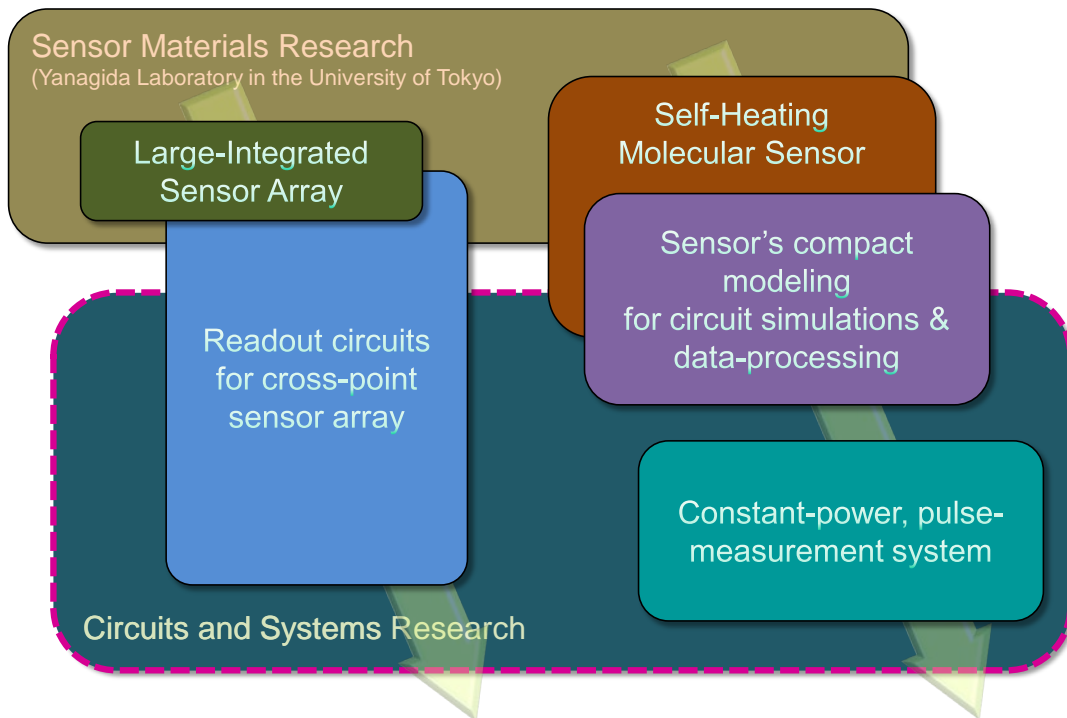


Figure 1.7 The research structure.

this study. On the other hand, the interface system has challenges to be solved. Figure 1.7 shows the themes of this study. For the large-integrated sensor array, a readout circuit is analyzed. The cross-point structure is selected as it has the advantages of fabrication processes. The readout accuracy is mainly evaluated through simulations. While both the large-integrated sensor array and self-heated metal-oxide sensor array are made from the same metal-oxide sensor, the self-heated sensor needs to be researched to endure high voltage, current, and temperature. Thereby, the self-heated sensors are developed independently, and their controller system is studied. Since temperature dependency of molecular responses enables a single type of sensor array to behave as different types of sensors, its compact model is developed to predict sensor responses. Additionally, the compact model is useful to develop a smart sensory system. As well as the compact model, a measurement system for the self-heated sensors is implemented. To make the most of the metal-oxide sensor, the interface system called the “Constant-power and pulse-measurement system” has been developed. As a

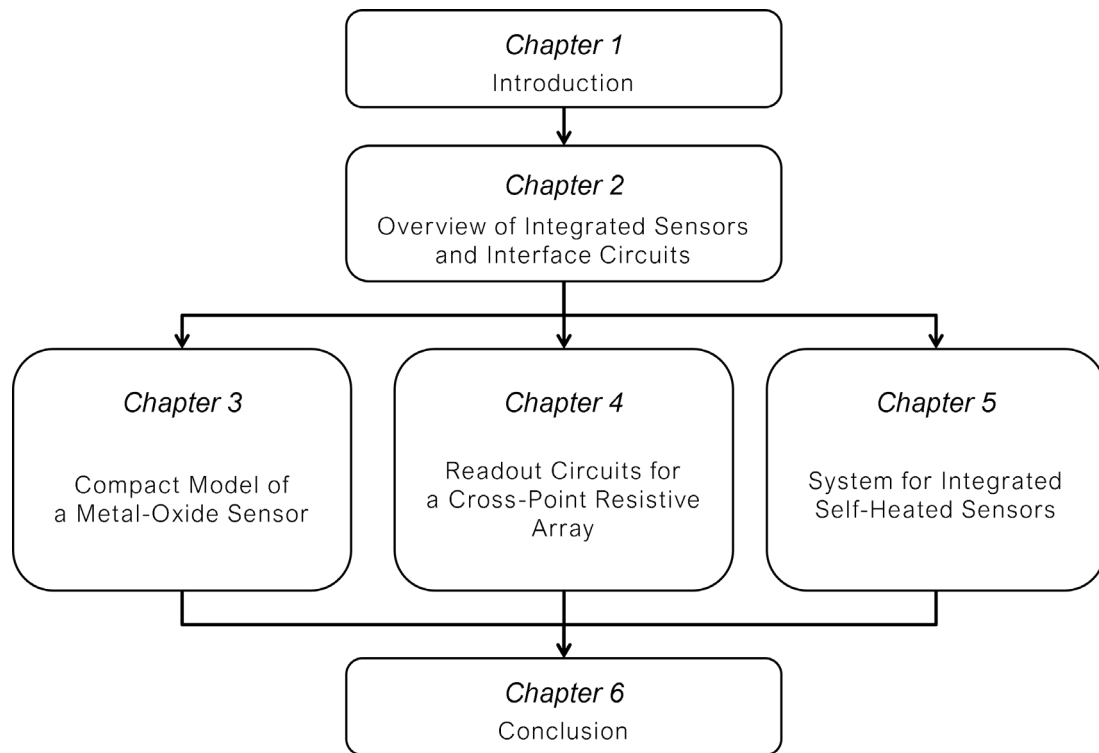


Figure 1.8 Graphical outline of this thesis.

proof-of-concept, the system is implemented, and the self-heated sensors are measured.

1.3 Thesis Outline

The remaining parts of this thesis are organized as follows (Figure 1.8): Chapter 2 describes the practical challenges to realizing an electronic nose from the perspective of circuits and systems. The two types of developing sensors are shown: a cross-point resistive sensor array and self-heated metal-oxide integrated sensors. In Chapter 3, a compact model of the self-heated metal-oxide sensor is described. Extended from previous work, a new sensor model is proposed including a feedback loop for the self-heating effects. Based on the developed self-heated metal-oxide sensors, model parameters are fitted. To show the effectiveness of the model, simulation outputs and experimental results are

compared. Chapter 4 describes readout circuits for the cross-point sensor array. Sneak-current effects and the readout error caused by an op-amp are analyzed and discussed. To improve the readout accuracy, a calibration technique to eliminate the effects of nonidealities of an op-amp is proposed. In Section 4.3, new readout methods called sneak-path-controlled readout (SPCR) and accurate SPCR (ASPCR) are also proposed. Contrary to the conventional readouts using op-amps, those two methods remove an op-amp and calculate all the resistance with matrix equations. Their readout performance is discussed based on simulation results from various viewpoints. Chapter 5 describes a new measurement system to control and measure the self-heated metal-oxide sensor array. To achieve the requirements of the sensory system, dedicated circuits and their operations are designed. The proposed system is called the constant-power and pulse-measurement system in this thesis. The performances of the system are reviewed with detailed measurement results. To check the validity, the self-heated sensors are measured, and the effectiveness of the sensory emulation is discussed. In Chapter 6, the results of the studies are summarized, and future perspectives of this study are given.

Chapter 2

Overview of Integrated Sensors and Interface Circuits

An overview of sensory development to implement an electronic nose is given. Considering the goal design introduced in Chapter 1 from the beginning can lead to complex issues. Therefore, we focus on two types of sensor chips which have core technologies within the goal design. In this chapter, the structures and novelties of each sensor chip are described. In addition, challenges of the implementation of the sensory circuits and systems are discussed.

2.1 Integration of Metal-Oxide Sensors

As a material of gas sensors, metal-oxide sensor is frequently used to detect target molecules. Our developing system integrates more than a thousand types of gas sensors in one chip and mimics mammalian noses to analyze the air complexly. Especially for electric nose applications, metal-oxide gas sensors have been used because of their advantageous features such as low cost, short response time, and easy fabrication process [72]. Their resistance value reactions to target gases were in a range between 0.1% and above 100%. The olfactory systems must meet their physical characteristics to acquire odor information.

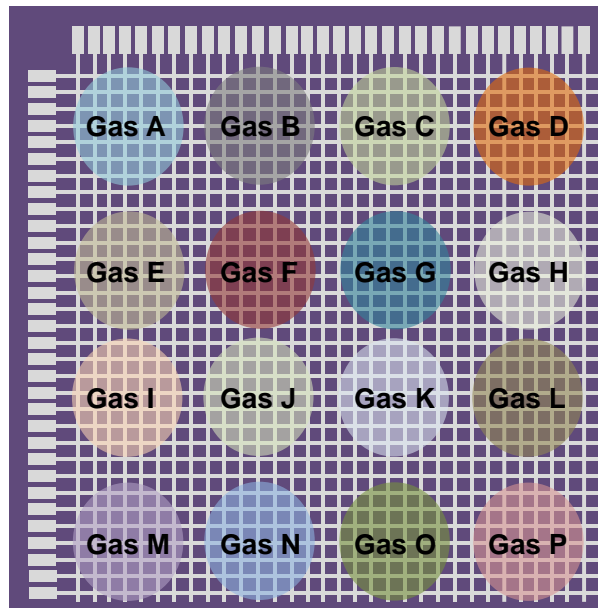


Figure 2.1 A cross-point structure sensor and its graphical image to react various types of gases.

2.1.1 Cross-Point Resistive Sensor Array

Resistive arrays are used in various applications such as tactile sensors [73]–[77], temperature sensors [77], [78], gas sensors [79], [80], and resistive memories [81]–[83]. The shape of a matrix array is an effective way to integrate a lot of sensors in a small area. Only $M + N$ connections are needed to access each sensor for an $M \cdot N$ array. Especially, the structure in which each sensor does not have a selecting switch element is called a cross-point structure. The cross-point structure is beneficial to sensor device development because of its simple fabrication process, and thus it contributes to low-cost development. Although the advantage in terms of a fabrication process is meaningful, it causes alternate issues in the readout circuit. Sensors that are arranged on the same column or row share electrodes so that many of the sneak currents will occur. Thereby, the sensor interface circuit needs to be designed not to be affected by those sneak-path currents.

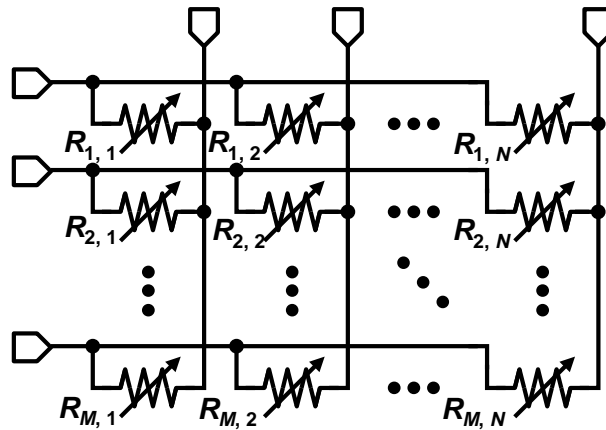


Figure 2.2 Equivalent circuit of the sensor chip.

The model of a developing sensor chip is shown in Figure 2.1. The matrix shape of integrated sensors is 32×32 , which are resistive sensors made with metal-oxide materials. Compared with the conventional systems, the space per sensor can be miniaturized. Each sensor is interconnected. The cross-point structure takes advantage of a sensor chip fabrication cost because it does not require an advanced fabrication process. Besides, if the sensor process is not CMOS compatible, its fabrication process will be constrained so as not to damage the CMOS circuit. Since the sensor chip and its interface circuit are separated physically, unnecessary concerns can be reduced in process developments. Moreover, the separating is also beneficial while running sensors. Most semiconductor sensors usually use external heaters to enhance their chemical response to gases, damaging surrounding circuits. The circuit can be protected from excessive heating.

The structure of a gas sensor chip is a cross-point matrix array. Figure 2.2 shows its equivalent circuit. The shape of the matrix array is 32×32 and the sensors sharing the same column or the same row connect to the same electrode. Those electrodes are made with metal and neither switch elements nor nonlinear elements like diodes are included here. This simple structure is beneficial in several points.

Firstly, the simple structure requires a low cost for fabricating. Integrating different types of sensors is so challenging that many trial fabrications will be needed. Although semiconductor sensors are commonly fabricated with a circuit like CMOS image sensors, it is still highly expensive to make an integrated circuit compared to fabricating sensors. The second reason is that there becomes no need to consider circuit tolerances in any post-processes. It is related to difficulties to create different sensors in the small chip. Thus, those processes like molecular injection will be effective after making a semiconductor base. Additionally, annealing by using high temperatures is often required to refresh sensor conditions. CMOS circuits can be damaged by exposure to high temperatures. If its interface circuit can be separated from the sensor device, various types of post-processes will become free from the physical conditions of CMOS circuits. Furthermore, an external heater to enhance chemical reactions causes similar problems. Most gas sensors made of semiconductor materials change their resistance by gas molecules. To promote reactions, the operation of gas sensors requires 200 °C or higher temperatures in general. However, the circuit usually cannot tolerate it. Therefore, separating a sensor device from the interface circuit is important to ensure the system.

2.1.2 Circuits for a Cross-Point Resistive Array

The performance of a sensing system depends on an interface circuit as well as a sensor. The circuit designer should about care the gain of amplification of sensor signals, the noise level, and the absolute/relative error of readout. In terms of systems that use one gas sensor, the circuit achieving the dynamic range of 153 dB was reported. In addition, its interface which can acquire the concentration of benzene and NO₂ with mW-order of power consumption was reported [84], [85]. In contrast, an odor system integrating lots of sensors needs to consider power efficiency for one sensor, scanning speed, crosstalk between sensors, robustness for readout, the complexity of a circuit implementation, and so on.

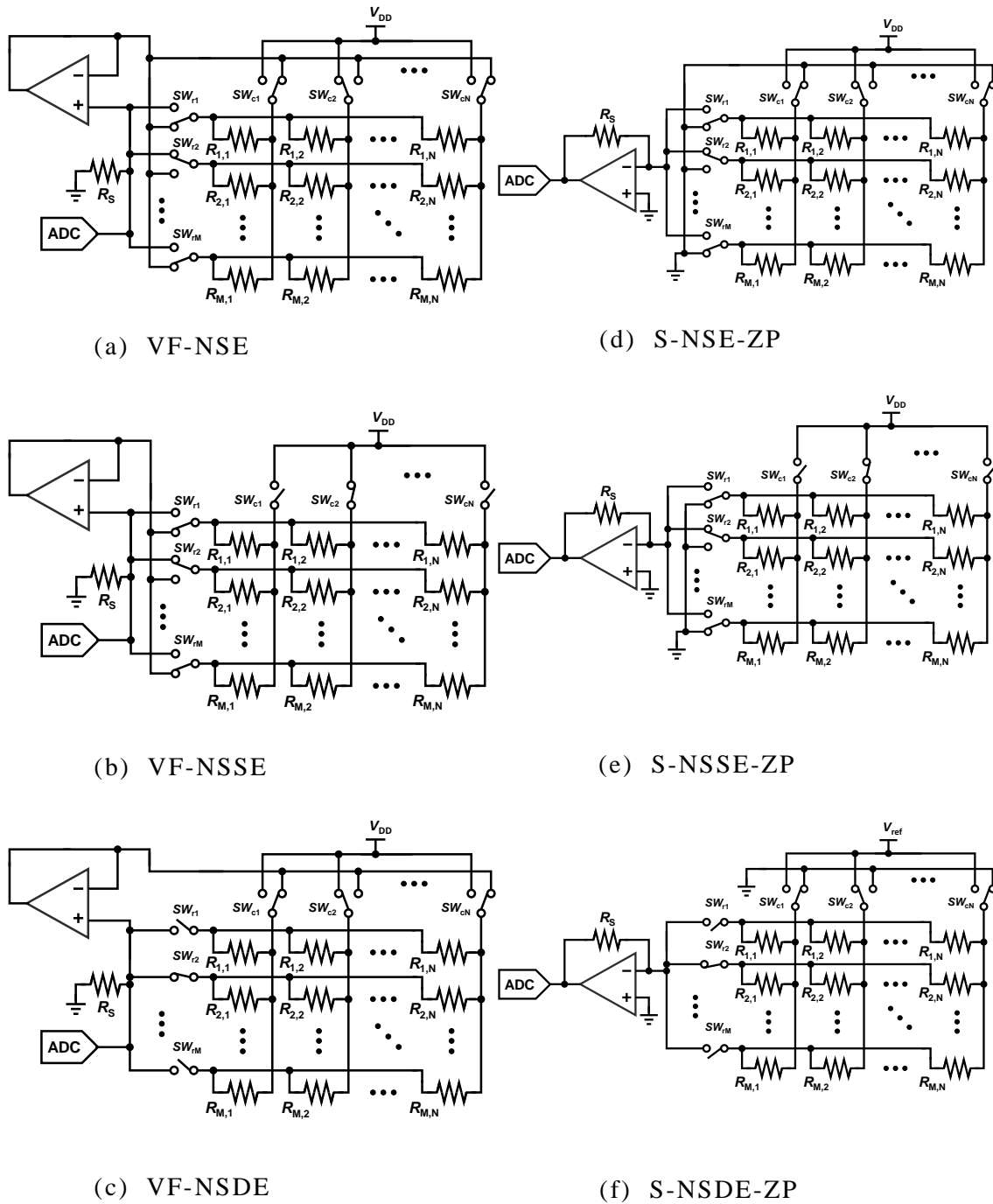


Figure 2.3 Fundamental readout circuits for a resistive array called Voltage Feedback Methods (VFM) and Zero Potential Methods (ZPM).

Several previous works have discussed how to read every resistance value from a resistive matrix array, which is used in tactile sensors or pressure sensors, temperature sensors, and gas sensors. However, the side effects caused by integrating thousands of sensors have not been discussed much enough. In [86], 6 fundamental measurement methods, which are called voltage feedback non-scanned-electrode (VF-NSE) method, voltage feedback non-scanned-sampling-electrode (VF-NSSE) method, voltage feedback non-scanned-driving-electrode (VF-NSDE) method, setting non-scanned-electrode zero potential (S-NSE-ZP), setting non-scanned-sampling-electrode zero potential (S-NSSE-ZP) method and setting non-scanned-driving-electrode zero potential (S-NSDE-ZP) method, for reading a resistive sensor array are mentioned and the error of resistance are shown through measurements for each method. The three circuits using the voltage feedback method are shown in Figure 2.3 (a), (b) (c), and the three circuits using zero-potential method are shown in Figure 2.3 (d), (e), (f). These methods were also simulated in several papers, and it was found that several nonidealities caused a large error, such as switch on-resistance, offset voltage, bias current and a finite gain of an op-amp, and so on. In [87], the error derived from the op-amp was able to be decreased by using double sampling readout techniques from 20% to 0.89%, through simulations and from 84 % to 0.69%, through measurements. However, the operating frequency reduces to about a half by using double sampling, and most of the currents flow through non-measured resistors causing the power dissipation to rise. In [88], a calibration method of adding a known resistor to the resistive array is shown. In this method, adding a known resistance for calibration reduced the error of switch resistance and the op-amp nonideality. The report keeps the error to 2.5×10^{-3} % through simulation. However, the problem with this system is that the area that the circuit takes up is quite large. The important thing to note from these previous works is that none of them have measurement results with a system that contains over 1,000 sensors. The Zero-Potential method (ZPM) is sure to consume large amounts of power due to its circuit topology. Therefore, it will not be suitable for gas detection systems

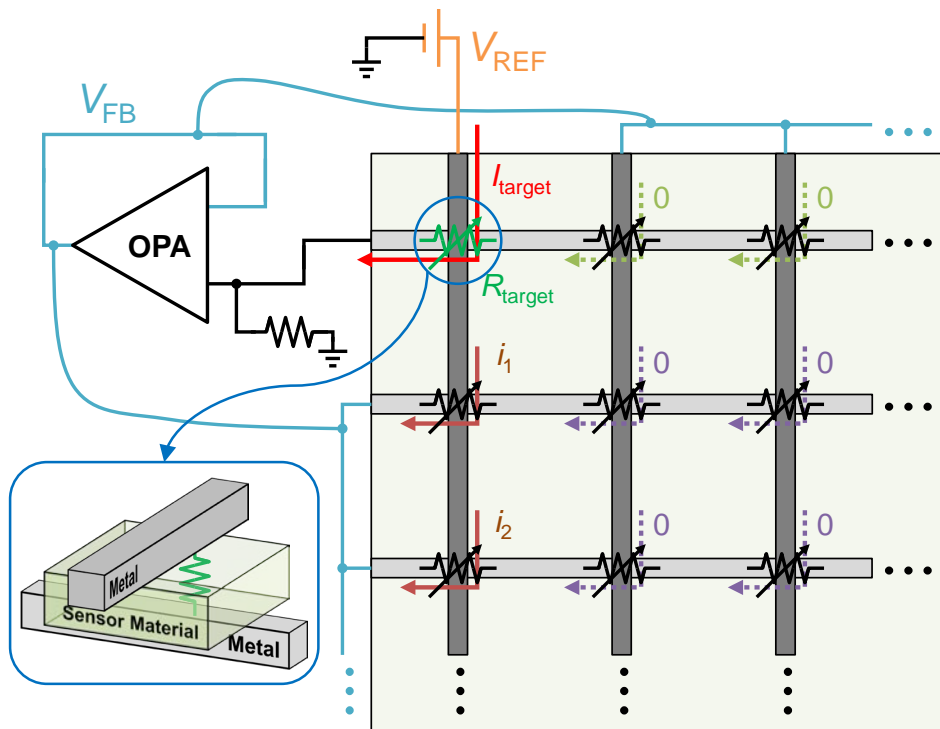


Figure 2.4 Large current load from an op-amp.

for IoT purposes. The Voltage Feedback method (VFM) requires a large driving power for its op-amp with a large load (Figure 2.4).

In the above methods, resistance in the matrix array is calculated with a simple equation for a resistive voltage-divider circuit or a trans-impedance circuit. However, a practical op-amp causes feedback error mainly due to its limited gain, high output impedance [89], [90], and input offset current or voltage [87], [88]; accordingly, elaborate techniques to cancel these characteristics are required. Scanning speed is inherently affected by the op-amp because the settling time of the op-amp is determined by its slew rate. To maintain accurate reading and proper scanning speed, the op-amp must have appropriate performance. To the detriment of obtaining a readout circuit with sufficient performance, an elaborate circuit design is required. As a result, the readout circuit is not robust in regard to variable array size, fluctuation of sensor resistance, and distribution of sensor resistance. One approach uses a simple circuit and calculates sensor resistance

by a matrix computation. For instance, the resistance of a tactile sensor was determined by measuring the voltage of the edges of a square-shaped resistive array in [91], [92]. Another approach calculates a resistance map with electrical-impedance tomography (EIT) solvers or an incident matrix. Both approaches, however, require intricate matrix operations or large computations for the readout operation. In the meantime, the resistance matrix approach (RMA) was proposed [93]. As for RMA, in the readout operation of an $n \times n$ array, n combinations of digital output were successively biased on n row electrodes, and n column voltages were measured by n analog-to-digital converters (ADCs). Compared to the interface circuits proposed in [91], [92], the interface RMA-based interface circuit and the established equation became simple. Moreover, with the quasi-zero potential method [94], resistance is calculated by transfer functions obtained by converting the output voltage for $N \cdot (M+1+(N+1)/2)$ switching conditions. Furthermore, as for an op-amp-less readout [95], a simple circuit consists of analog switches, a reference resistance, and two ADCs. This approach achieved a readout error of 0.06% in the case of a 32×32 array with 16-bit ADCs.

2.2 Self-Heated Metal-Oxide Sensor

In general, a metal-oxide sensor needs an external heater, as the reaction between the sensor and gas molecules is enhanced under the high temperature. However, the heater consumes larger power than the sensor. A self-heated sensor is a promising technology because only the small area is heated, and power consumption is decreased. In addition, self-heating is beneficial for temperature modulation for an independent sensor, considering the whole sensory system. In this section, an overview of the self-heated metal-oxide sensor is given.

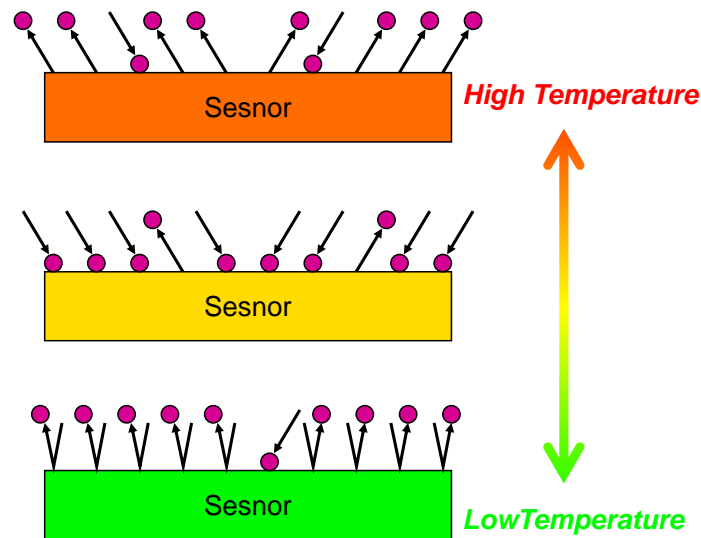


Figure 2.5 Expected sensor reaction depending on sensor's temperature.

2.2.1 Temperature Dependency

Compared with most conventional semiconductor sensors, self-heated metal-oxide sensors are beneficial for developing low-power systems because they consume small power to increase sensing temperature [31], [96]. In addition, there have been some reports that the sensor configured to different temperature reacts to different molecules [97]–[99]. For example, H. Liu, et al. reported the temperature dependency of NiO sensors to some molecules in [97]: If the sensor's temperature is 150 °C, its resistance change rate to ethanol becomes maximum. If the temperature is 190 °C, the change rate to formaldehyde becomes maximum. If the temperature is 210 °C, the change rate to toluene becomes maximum. A simple illustration of temperature dependency is shown in Figure 2.5. Although there are difficulties to build a practical and stable system, it shows the potential possibility to emulate different sensors by using a single sensor with various operating conditions. Conventionally, the temperature dependency has been surveyed with rough temperature settings. They used fixed voltage bias even though sensor resistance is changed during experiments due to reacting molecules and their temperature coefficient. In addition, temperature resolution is not good

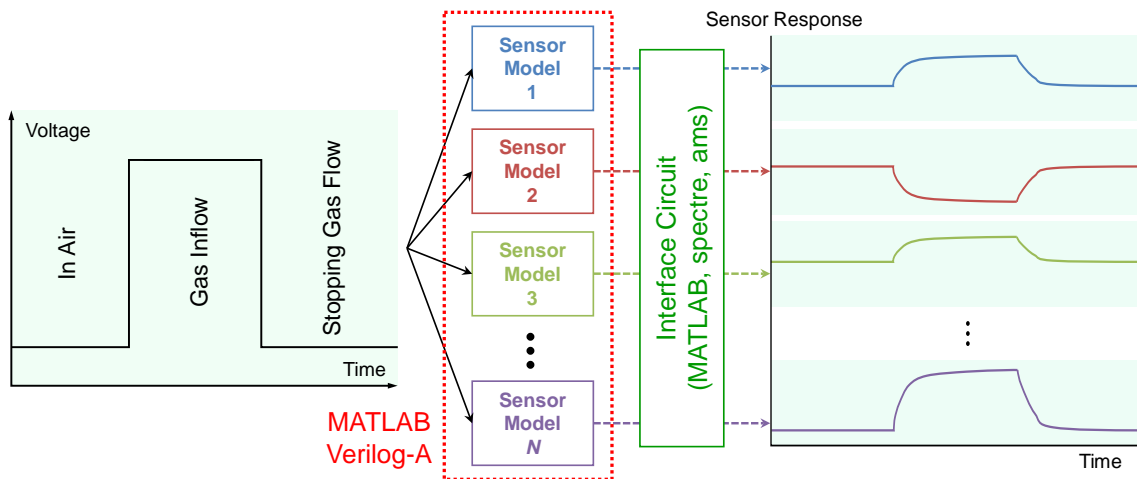


Figure 2.6 Simulated sensor response.

enough. Therefore, it is significantly important to survey this phenomenon precisely with an elaborated measurement system.

Towards developing advanced data processing technologies, compact modeling is highly useful for analyzing sensor data in advance by simulating many sensors' behavior as shown in Figure 2.6. It is not easy to measure the same results through physical experiments because experiments with many different gases require precise and complicated environmental setups. Besides, the sensor's reactions usually take minute-order time. Seeing from another perspective, the temperature modulation has the potential to establish a feedback system to adapt to surrounding environments. The feedback system can be formed by changing the sensory characteristics. Therefore, the compact model helps to create a classification algorithm or application that requires sensory response beforehand.

2.2.2 Temperature Modulation System

Since the advanced sensory systems have strong relation with Internet-of-Things (IoT) applications, gas sensory devices with portable and low-power consumption are often useful and beneficial. In [11], [100], a capacitive

micromachined ultrasonic transducer (CMUT) array was used for gas measurement. Conceptual diagram of wearable gas sensory system is shown, and 1.62 mW was consumed for the measurement. Although six CMUT sensors were implemented, the area occupied by a sensor was larger than 1 mm². In [101], a productive gas sensor, called BME680, was used, and four of them formed a gas sensor array. The operating temperature was configured at the different temperatures to classify three different types of gases. Its power consumption is as low as 0.09 mA × 1.8 V in an ultra-low power mode. However, their heaters to control the operating temperature consumes 17 mA × 1.8 V typically at each sensor. Other works targeting IoT applications [14], [102], [103] were also reported in recent years. However, there is a critical limitation in the trade-off between the number of the mounted sensors and power consumption. In addition, the number of sensor integration is limited to around ten sensors at most, considered the size and power of system.

Among the semiconductor gas sensors, metal-oxide gas sensors have advantages of sensitivity, response time, and cost [104]. In particular, high integration capability is one of the substantial features for IoT or real-time applications. In [105], a gas sensor array made of SnO₂ nanofilm was reported. The sensor was a lateral shape and 200 nm length, and 1,024 sensors were fabricated in a 6 × 6 mm² area. Even though all the 1,024 sensors were the same sensors, it shows the future possibility to implement as many sensors as a mammalian nose. Thus, the notable characteristics make the metal-oxide gas sensors suitable to create IoT applications. To decrease power consumption, low-power gas sensors have been focused. Since most metal-oxide sensors need to be operated at high temperature, power consumption is dominated by a heater. From the perspective of power consumption, low-power gas sensors are investigated in the review paper [71]. According to the paper, metal-oxide gas sensors with a microheater or self-heating are promising techniques for metal-oxide sensors to be sensitive during low-power operation. While the evaluation of the power

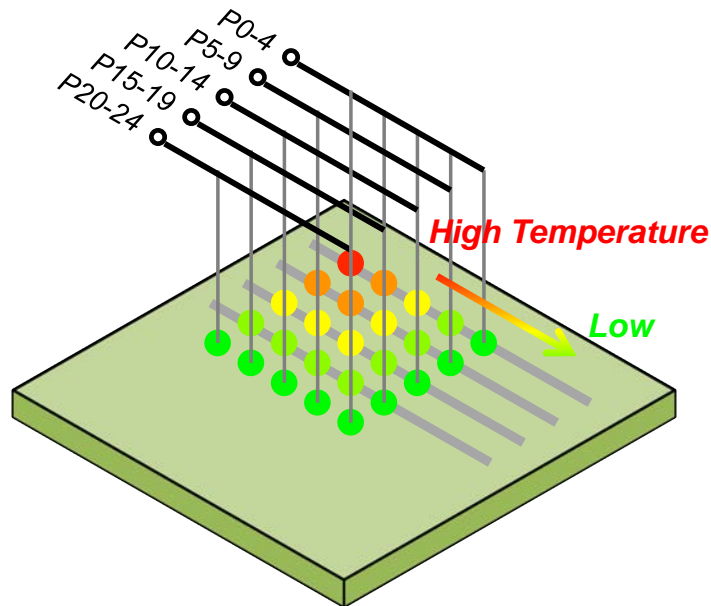


Figure 2.7 Temperature control by self-heating.

consumption of the sensors is required, the sensory system should be evaluated including the interface circuits.

Towards next-generation gas sensory system, it is important to consider the number of sensors, size, and power consumption. Although present process technology does not suit for fabricating a sensory chip using various materials, temperature modulated gas sensors have been researched. Since metal-oxide gas sensors has different temperature dependency with different gases, a single sensor can behave as different sensors [97]. In [106], toluene and butanone multicomponent gases were detected with a single SnO_2 sensor. By changing the temperature conditions of the sensor, different response to the binary component gases were obtained. The temperature modulation is promising technology, as many sensors can be emulated by controlling thermal conditions. However, the way to drive different sensors at different temperature should be considered, keeping low power consumption. To overcome the trade-offs among size, power-consumption, and the number of sensors, a novel sensory system is proposed with combining the self-heating and temperature-modulation techniques as shown in

Figure 2.7. The techniques make it possible to detect various gases with a small number of sensory materials and to configure the sensors at different temperatures even though the distances among the sensors are very narrow. In addition, self-heating will be effective for low-power sensing [107], [108]. Meanwhile, the interface controller of the sensors must equip operating functions with low-power consumption. In the operation, different powers are inputted into the sensors at the same time to control the sensors' temperatures. However, keeping independent temperatures needs multiple power sources, which leads enlargement of the interface circuit and increase of power consumption. Therefore, pulsed-heating method [107], [109], [110] is applied and total power consumption is assessed. As a proof-of-concept, an array of SnO₂ sensors is fabricated and a controller board is implemented in PCB. Considering the usage of portable device, 3.3 V input is assumed as a power source.

2.2.3 Low-Power System for the Integrated Self-Heated Sensors

To emulate multiple sensors by changing operating temperature of the self-heated sensor, it is necessary to implement a dedicated controller system. The controller system must have two fundamental functions of thermal controller and resistance readout. As described in Section 2.2.2, sensor's temperature is controlled by Joule heating consumed within the sensor. However, expected heating voltage is 5-15 V, and it is higher than voltage supplied by a cell of Li⁺ battery, 3.7 V, typically. Thus, up-converters are needed to supply the high voltage. However, many of them would have to be equipped into the controller system if the number of the odor sensors increases. Since many of up-converters consume large implementing area and large power-consumption, new, small-area, and low-power system is desired for the self-heated odor sensor. To address the issue of system power consumption, constant-power, pulse measurement system is proposed in our study. Conventional gas sensory systems use an external heater

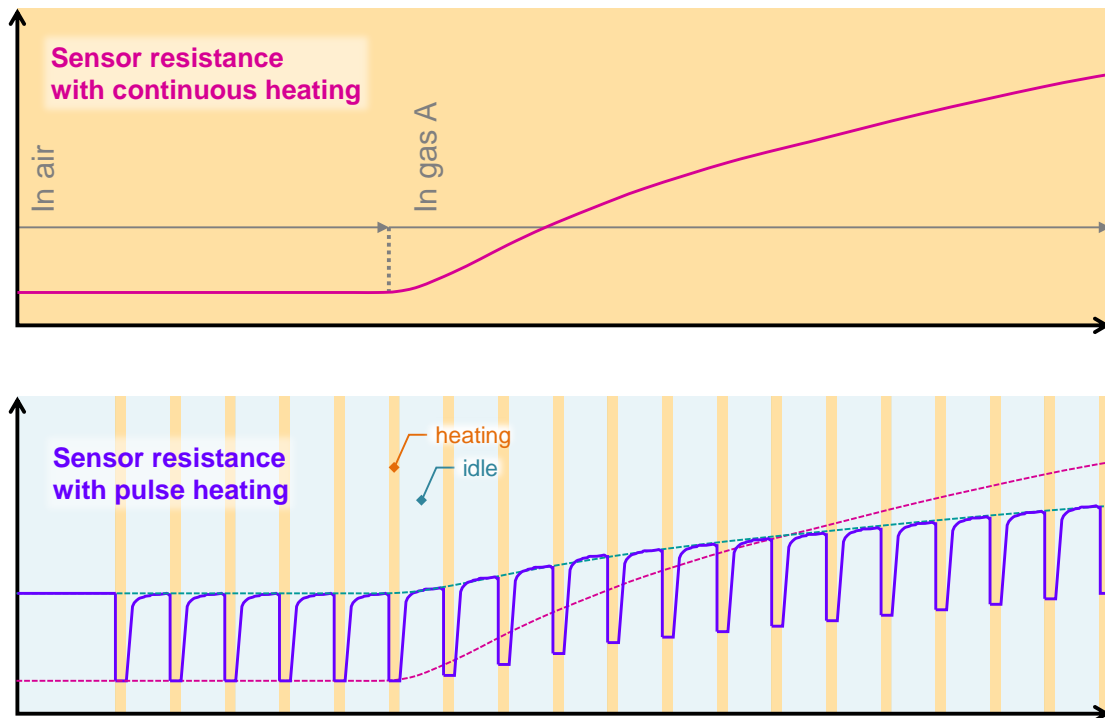


Figure 2.8 Conventional continuous heating operation and the proposed sensor operation.

to promote chemical reactions between the sensor and molecules in the air and the systems continuously heat the sensors with the heater. In contrast, the proposed system heated sensor in a short period but intermittently. In addition, while one sensor is heated, other sensors are not heated. The graphical image of the proposed operation is shown in Figure 2.8. In the figure, a red-line shows the expected measured resistance by heating continuously, and a purple-line shows the expected measured resistance by pulse heating. During heating, sensor resistance is changed rapidly. It depends on a sensor's condition whether the resistance increases or decreases. The heating pulses are biased periodically. By connecting measured resistance in idle timing, a new envelope curve is obtained, which expresses new sensor response that contains molecule information. It is expected that the sensitivity can be adjusted by a duty ratio of pulses. During the pulse heating, some types of molecules are attached to sensor's surface and their chemical reactions begin. After the pulse heating stops, the molecules remain

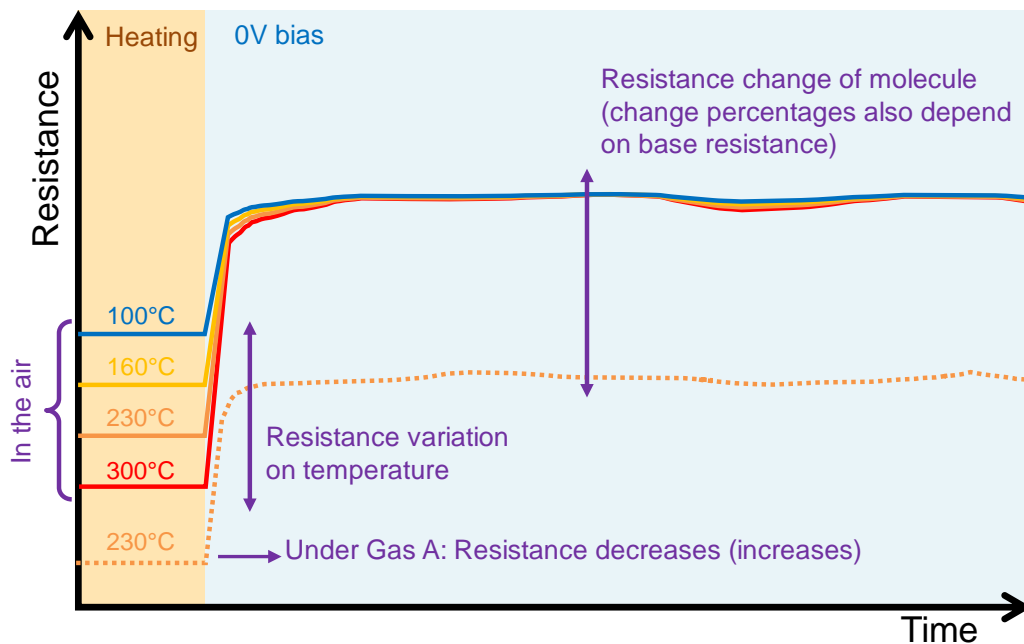


Figure 2.9 Simple illustration of resistance change of the self-heated sensor.

attached on the surface of the sensor. Moreover, since self-heating only affects small-area's temperature, thermal time constant is smaller than resistance change caused by molecule's interaction. An illustration that describes the sensor-resistance change is shown in Figure 2.9.

If the proposed system is achieved, just one or a few up-converters will be needed and power consumption per sensor will be decreased because it will not be necessary to heat all the sensors at the same time. To show its proof-of-concept, 16-sensor array was developed, and the array was experimented with the proposed system.

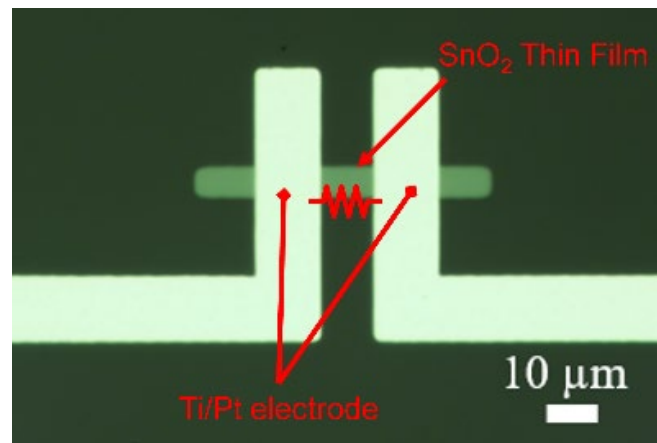
Chapter 3

Compact Model of a Metal-Oxide Sensor

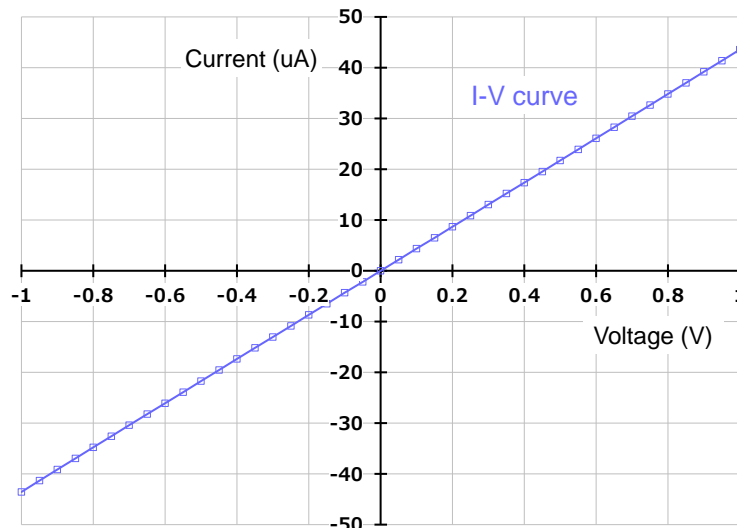
The conductance of a metal-oxide gas sensor is determined by surrounding gas concentration, operating temperature and humidity, activation energy, and so on. However, creating an exact simulation model of chemical sensors by using their dominant equations is difficult because many interactions among different molecules exist. In our study, we created a model to predict the rough behavior of a metal-oxide self-heated sensor. As the sensor conductance expresses the surface and internal condition of the sensor, the model is defined as a compact model. Firstly, the compact model and equations are shown. To identify the parameters of the model, a self-heated metal-oxide sensor is manufactured, and its experimental results are utilized.

3.1 Developed Sensor

In Figure 3.1, the microscope image of developed self-heated sensor and its measured I-V characteristics are shown. The I-V curves indicates that the sensor is an ohmic device. SnO₂ thin film (20nm) is used as the sensing material, and an electrode is made of Ti/Pt. The resistance of SnO₂ film is changed if it adsorbs certain molecules. The narrow sensor shape and 20nm thinness makes it operate



(a)



(b)

Figure 3.1 (a) Microscope image of the self-heated sensor device. (b) I-V curve of the self-heated sensor.

as a self-heated sensor. To verify the self-heated characteristics, thermal simulation was carried out with COMSOL Multiphysics software, and it was verified that only the sensor spot reached high temperature of around 420K as shown in Figure 3.2. In the thermal simulation, the sensor's electrical resistivity was set to $0.05 \Omega \cdot \text{cm}$, and 10 V was biased. The sensor film thickness was 20 nm, the cross-sectional area was $0.1 \times 10^{-8} \text{ cm}^2$, and the length was $10 \mu\text{m}$. Thus, the sensor resistance was calculated as around $50 \text{ k}\Omega$. The resistance value was fixed

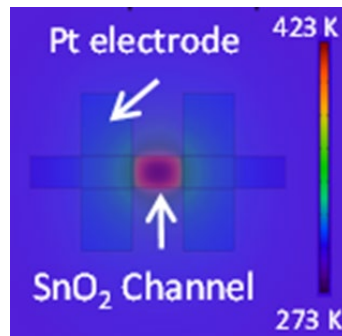


Figure 3.2 Thermal simulation results run in COMSOL

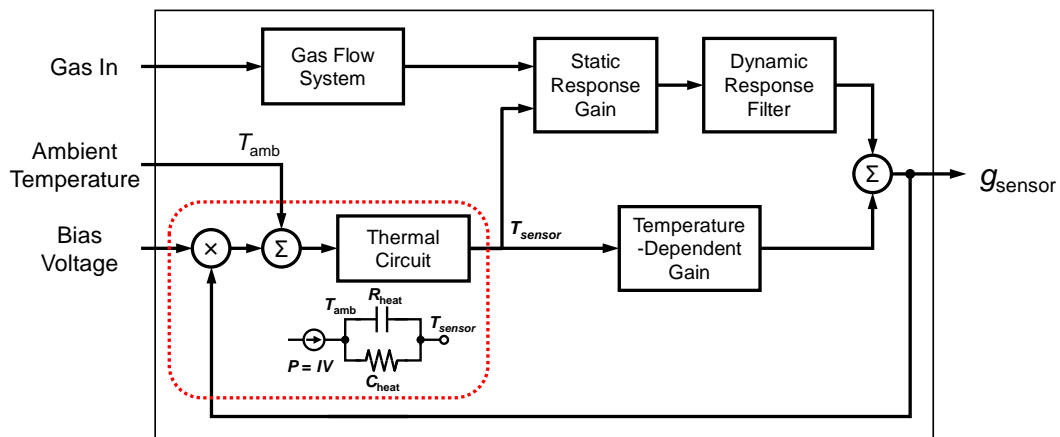


Figure 3.3 Self-heated metal-oxide sensor model

during the simulation, then nearly 2 mW heating was generated in the sensor device.

3.2 Compact Modeling

The developed block diagram of the self-heated sensor is shown in Figure 3.3. While the sensor's temperature was controlled with an external heater in the previous works [111], the feedback loop to cause temperature fluctuation derived from its own resistance change was added. To simplify the model, the number of input gas was limited to one. The gas flow system and the dynamic response filter were represented as low-pass filters. In this work, the gas flow system was removed because the dynamic response filter was dominated filter in our laboratory setup. The dynamic response filter consists of a 2nd-order filter. 2-poles and 1-zero values were fitted with System Identification Toolbox in MATLAB from experiment

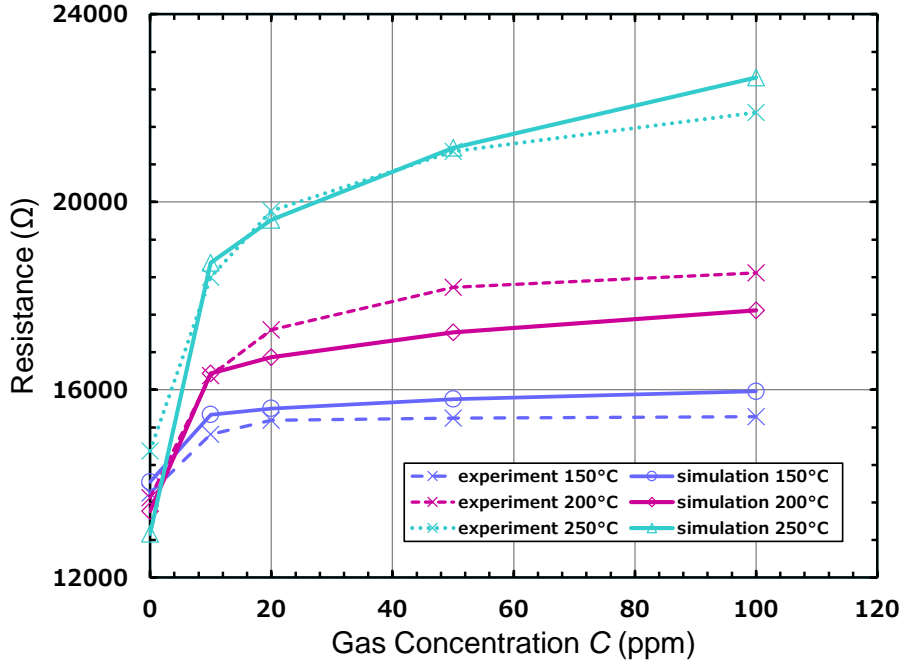


Figure 3.4 Comparison of the static responses between the simulated values with the fitting parameters and experiment data.

data plots. The static response gain and temperature-dependent gain are represented as follows:

$$G_{\text{gas}} = k_{1T} \cdot e^{-E_{A1}/kT} \cdot C^{n_1 kT} \quad (3.1)$$

$$G_{\text{base}} = G_{0T} \cdot e^{-E_{A0}/kT} \quad (3.2)$$

where k and T represent Boltzmann constant and absolute temperature. E_{A0} and E_{A1} are activation energies of the baseline conductance and of the change conductance by a target gas. k_{1T} , G_{0T} , and n_1 are coefficients. C represents the concentration of input gas. The thermal circuit consists of the thermal resistance R_{heat} and the thermal capacitance C_{heat} . Since it is quite difficult to measure the precise thermal circuit parameters, simulation results obtained from COMSOL Multiphysics software were substituted. The input voltage representing 1 ppm gas concentration corresponds to 1 V and the voltage follows linearly to the gas concentration. Temperature-dependent gain has a time delay until it is reflected

on the sensor resistance change. However, the time constant was much smaller than that of the molecule's dynamic response because of the small sensor size. Thereby, a filter for the temperature-dependent gain was not taken into account.

3.3 Experiment and Simulation Results

The unknown model parameters: E_{A0} , E_{A1} , k_{1T} , G_{0T} , and n_1 were determined by fitting them to experimental data with Equations 3.1 and 3.2. In the experiment, the target gas was NO_2 , and the surrounding gas was N_2 . In the experiment, resistance was measured under different temperatures of 150 °C, 200 °C, and 250 °C. Since it was difficult to monitor the sensor's surface temperature accurately, an external heater was used. Then, the bias voltage was set to 1V so as not to cause self-heating. In each temperature condition, gas concentration was set to 0 ppm, 10 ppm, 20 ppm, 50 ppm, and 100 ppm, and a steady-state value was measured. TABLE I shows adjusted parameters. In Figure 3.4, the comparison between experimental data and calculated data from the determined parameters is shown.

With determined parameters in the above experiments, the dynamic responses were compared. The ambient temperature was set to 100 °C and the sensor was biased with 9V and 10V. Figure 3.5 shows the resistance comparison between simulation and experiment data. Although the sensor drift effects were seen in the no gas phase, the static sensor response value in the simulation followed the experiment resistance change. It was also shown that sensing temperature in the simulations was fluctuate as high as 90°C when the sensor reacted to NO_2 under a constant bias voltage condition.

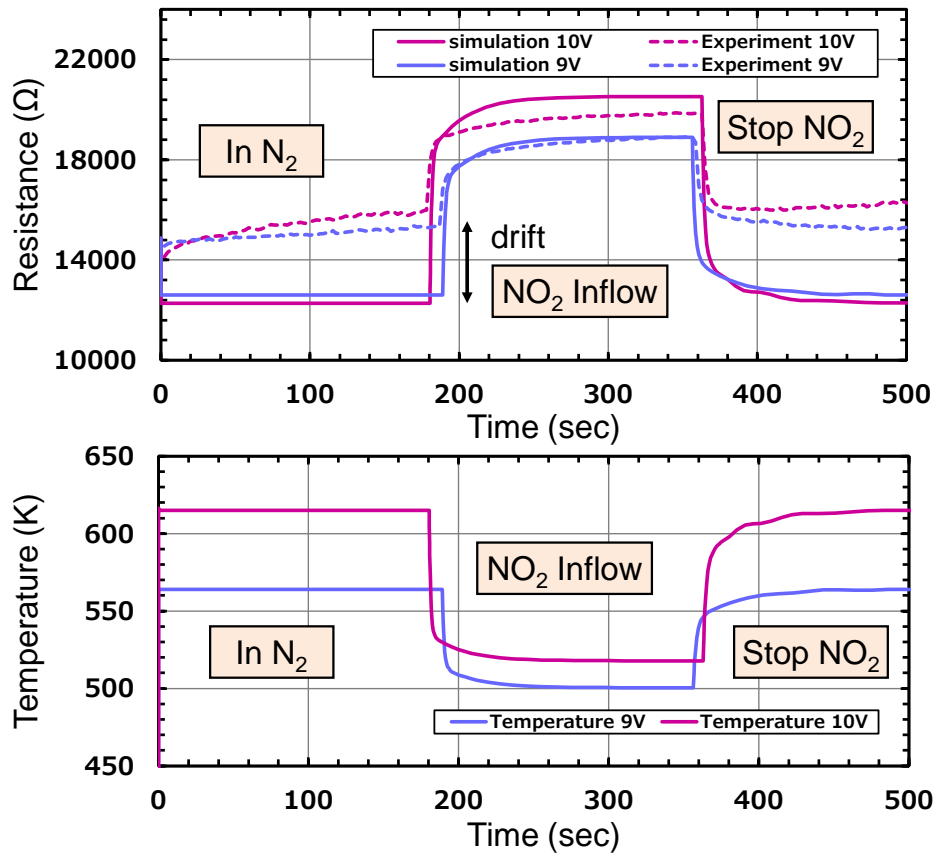


Figure 3.5 Comparison of the dynamic responses between the simulated values with the fitting parameters and experiment data.

Chapter 4

Readout Circuits for a Cross-Point Resistive Array

The voltage-feedback method (VFM) and zero-potential method (ZPM) are the conventional and fundamental techniques to suppress sneak currents. However, readout error that is caused by op-amp nonidealities increases over 10 %, depending on the size of a sensor array. To detect resistance changes of sensor responses, 0.1-1 % accuracy is demanded for the readout circuits according to previous experimental results [112]. In this chapter, software-calibration techniques for the VFM and a new readout technique removing an op-amp is proposed. Based on the structure of readout circuits, this chapter is divided as follows: Section 4.1 and 4.2 describe circuit analysis and the calibration techniques for the VFM. Section 4.3 describes the amp-less readout methods called “sneak-path-controlled readout” (SPCR) and “accurate SPCR” (ASPCR). Section 4.4 shows a demonstration with the developed cross-point resistive sensor array.

4.1 Op-Amp Output Impedance Effects

In VF-NSE, each resistance is measured by suppressing sneak currents with an op-amp. If the voltage feedback is achieved ideally, the current flowing in the

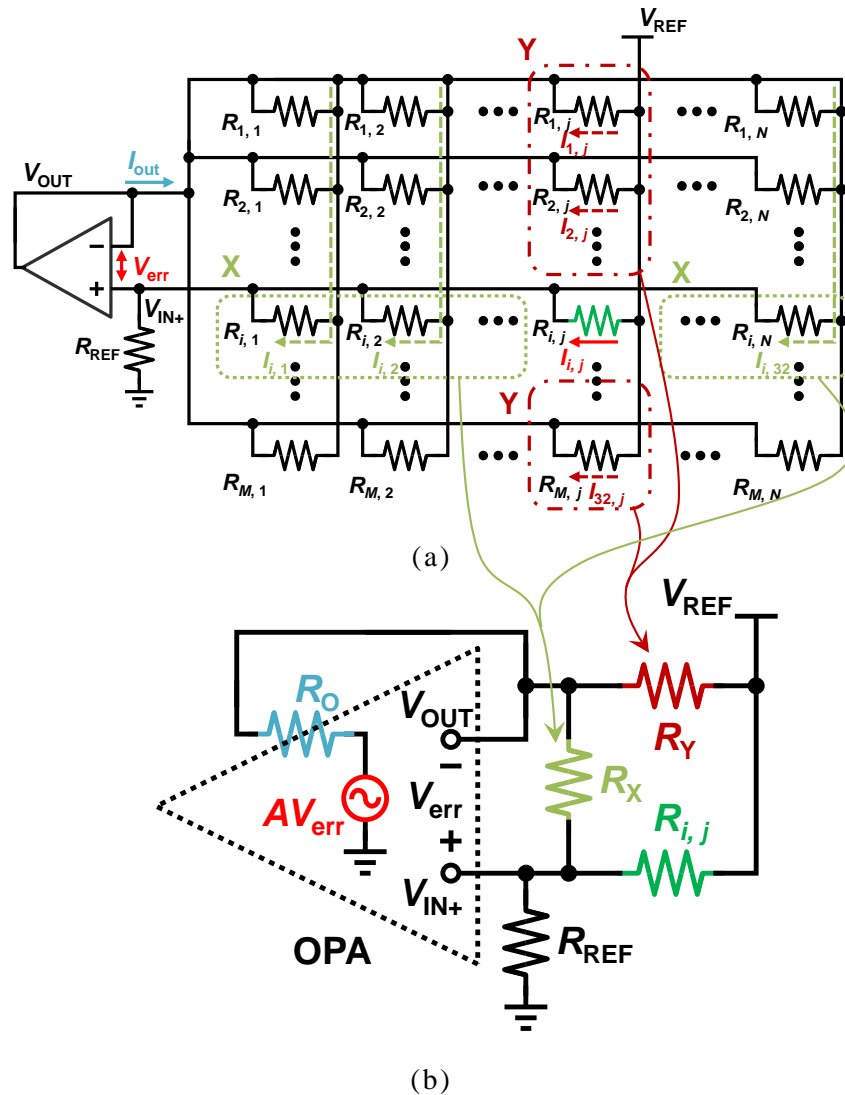


Figure 4.1 A op-amp model to analyze a readout error (a) The sneak currents due to finite gain and output impedance of an op-amp. (b) A simplified circuit. The resistors causing readout error are represented by the three resistors, R_Y and R_X and $R_{i,j}$.

reference is the same amount as that flowing the measured resistance. It constitutes a voltage division circuit, and the measured resistance value is calculated by measuring the op-amp's positive-node voltage. However, the feedback may not be maintained due to the op-amp's output impedance, a finite gain, and offset voltage. It causes unexpected sneak paths, as shown in Figure 4.1 (a). Here, the i -th-row and the j -th-column resistance value are selected. The unmeasured resistors which share the same i -th-row electrode are applied V_{err} ,

and their currents flow into R_{REF} . Regardless of the feedback error, $V_{REF} - V_{OUT}$ is applied to the resistors sharing the same column electrode. Most of the currents will flow into an op-amp output node. The main error of the feedback is an op-amp finite gain. If the gain of the op-amp is large enough, V_{err} keeps zero. However, it is not easy to keep a stable condition of unity gain feedback when a high-gain op-amp is used. The op-amp drivability is also essential for the feedback because a large scale of an array consumes a large amount of current. If the op-amp load becomes large, the output impedance cannot be ignored. In such cases, the feedback error will occur, and the sneak currents flowing into R_{REF} directly increase the readout error.

4.1.1 Feedback Error Evaluating Model

The VF-NSE circuit was simplified to analyze the influence of op-amp nonidealities, assuming all the sensor resistance values were the same and the op-amp was expressed as a voltage-controlled voltage source and output resistance (Figure 4.1 (b)). Here, the sensor resistance value $R_{i,j}$ was selected. The combined resistance of the resistors sharing the same row electrode was expressed as R_X and that sharing the same column electrode was expressed as R_Y . This circuit equation was expressed as follows:

$$\frac{V_{REF} - V_{in+}}{R_{i,j}} + \frac{V_{err}}{R_X} = \frac{V_{in+}}{R_{REF}} \quad (4.1)$$

$$\frac{V_{REF} - V_{OUT}}{R_Y} = \frac{V_{err}}{R_X} + \frac{V_{OUT} - AV_{err}}{R_O} \quad (4.2)$$

If the circuit parameters satisfy the conditions below, V_{err} becomes zero. It appears in Figure 4.2 as the lowest V_{err} value.

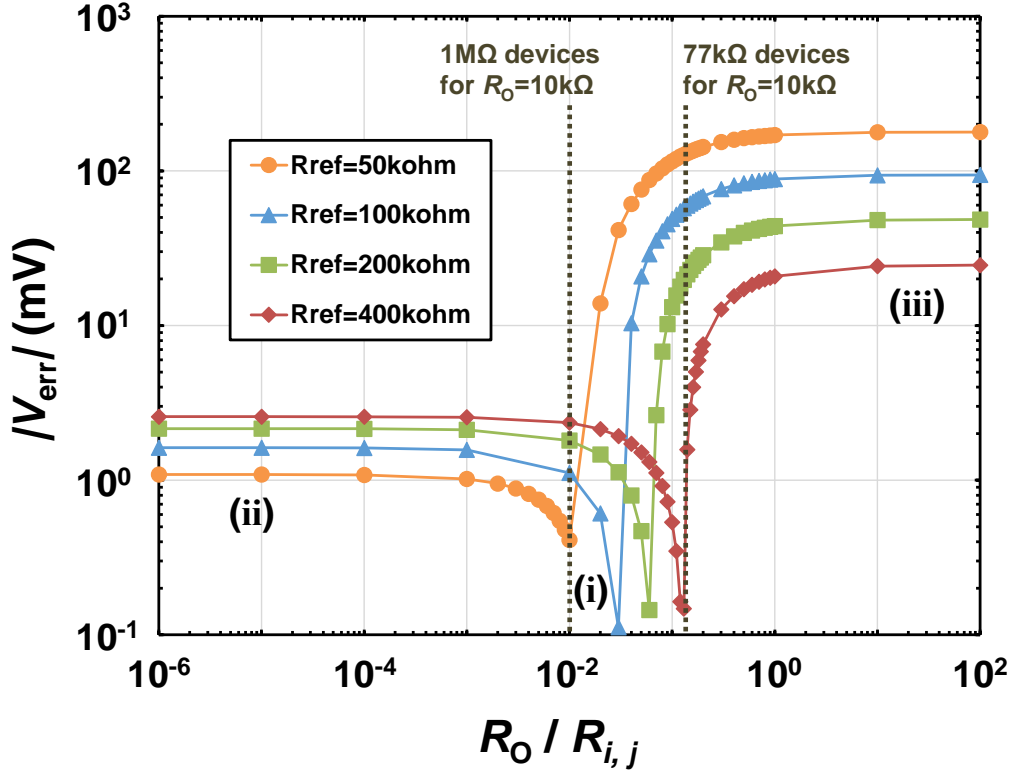


Figure 4.2 Feedback voltage Error of VF-NSE method, in which the reference resistance is parameterized. Dashed line indicates example numbers.

$$R_{i,j} \cdot R_O = R_Y \cdot R_{REF} \quad (4.3)$$

$$V_{in+} = \frac{R_O}{R_O + R_Y} \cdot V_{REF} \quad (4.4)$$

In the following discussion, the behaviors of the RMSE are categorized into three regions: (i) the op-amp output resistance almost satisfies Equation 4.3, (ii) low values (a left side of the graphs), and (iii) high values (a right side of the graphs). V_{REF} is set to 3.3V. The vertical axis corresponds to the V_{err} , and the horizontal axis corresponds to the relative value of R_O . In the region (i), the sneak currents do not flow in the resistors without ones that share the scanning electrode. Therefore, the readout error does not occur by the op-amp limited gain and non-zero output resistance. In the region (ii), the AV_{err} , which is amplified voltage

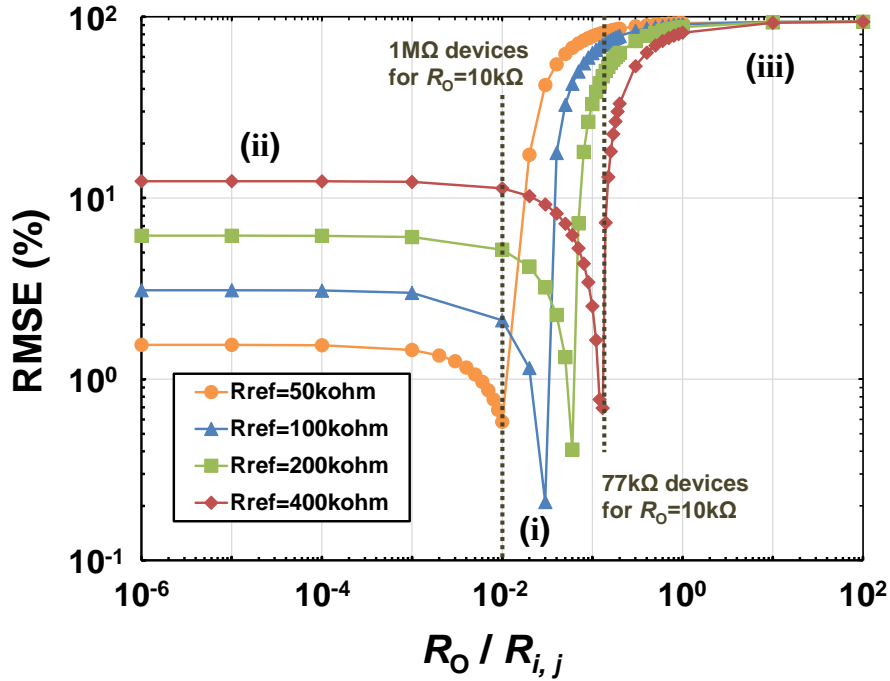


Figure 4.3 Read error of VF-NSE method, in which the reference resistance is parameterized. Dashed line indicates example numbers.

inside the op-amp, and the output voltage V_{OUT} become the same values. Then, V_{err} keeps a constant value, and the following equation is established.

$$V_{err} = \frac{R_{REF} \cdot R_X \cdot V_{REF}}{(A + 1)R_X(R_{i,j} + R_{REF}) + R_{REF} \cdot R_{i,j}} \quad (4.5)$$

This equation implies that V_{err} decreases as the gain A increases. In the region (iii), where the output resistance is large enough, the current in R_X is almost the same amount of that in R_Y as the output current from op-amp hardly flows. Thus, V_{err} is saturated, and the following equation works.

$$V_{err} = \frac{R_{i,j} \cdot R_X \cdot R_{REF}}{(R_X + R_Y) \cdot (R_{i,j} + R_{REF}) + R_{i,j} \cdot R_{REF}} \quad (4.6)$$

V_{err} is no more affected by the op-amp gain, and feedback does not ease the input difference. The error of each resistance readout is derived from the current in R_X .

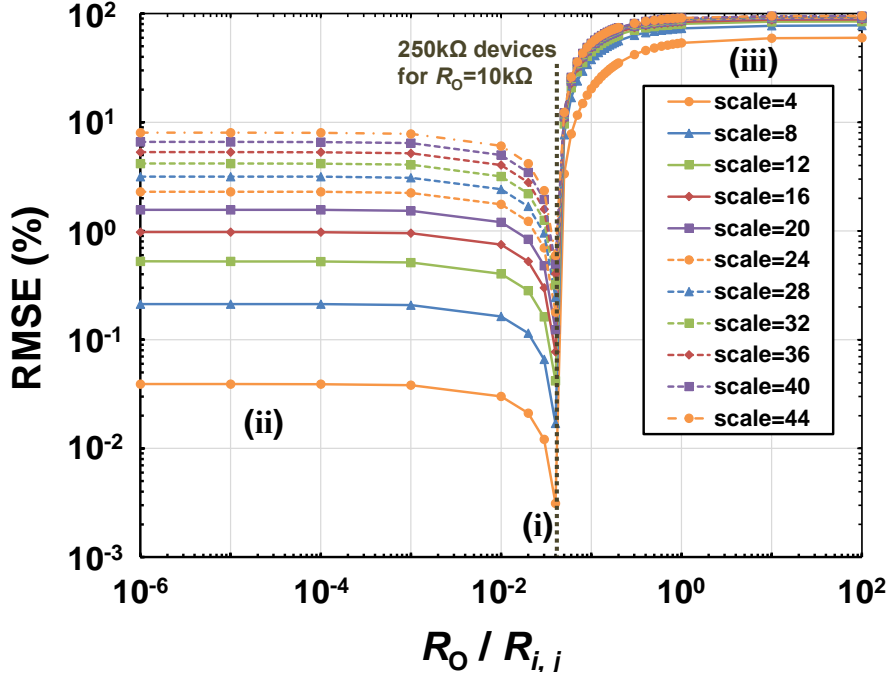


Figure 4.4 Readout error of VF-NSE method, in which the size of matrix array is parameterized. Dashed line indicates example numbers.

Therefore, it is equal to the ratio of the current flowing into R_{REF} and that into R_X : I_X / I_{REF} .

4.1.2 Feedback Error Analysis

The readout error was calculated with the simplified model. MATLAB and Simulink were used for the circuit simulations. Figure 4.3 shows the results of the readout error of VF-NSE, assuming the array size was 32×32 , and an op-amp gain was 1,000. The vertical line corresponds to the readout error, which is defined as the formula below.

$$\text{RMSE}(\%) = 100 \cdot \left| \frac{R_{i,j_true} - R_{i,j_measured}}{R_{i,j_true}} \right| \quad (4.7)$$

The true value of the target resistance is expressed as R_{i,j_true} , and the measured or calculated resistance is expressed as $R_{i,j_measured}$ in Equation 4.7. It

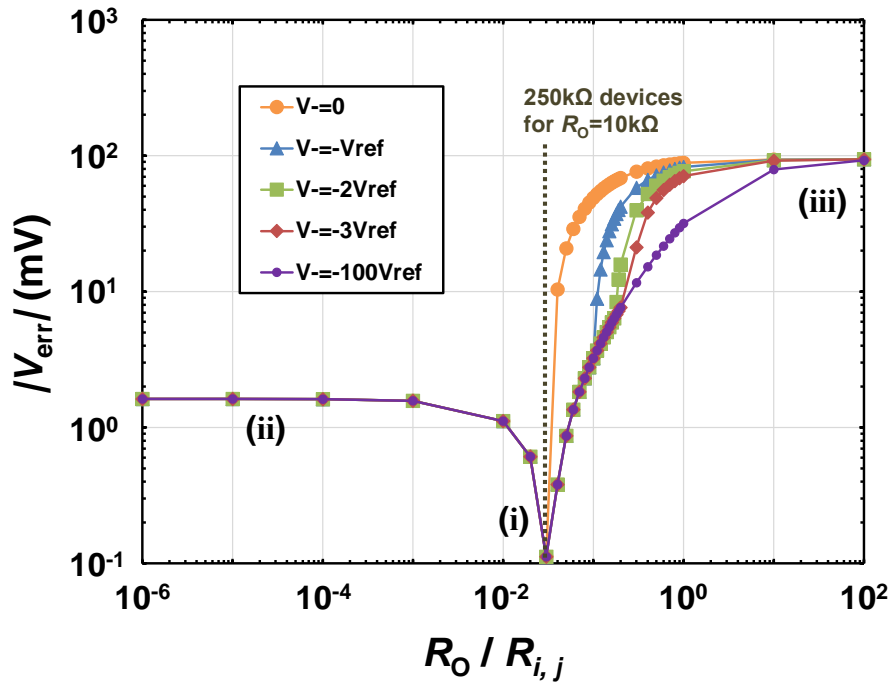


Figure 4.5 Dependency of feedback voltage error on op-amp output voltage. The negative voltage is defined as $-n \cdot V_{REF}$. Dashed line indicates example numbers.

was shown that the error rapidly became worse when the op-amp output resistance value was a larger value than the value satisfied Equation 4.3, Equation 4.4. While the accuracy increases as R_{REF} decreased, the valid range of an op-amp output impedance got narrow. The deterioration due to an array scale should be considered. If V_{err} is the same between different target array, the sum of the current in the area will be large. The error of the scale effects was simulated, and the results are shown in Figure 4.4. Those tested are square arrays, and thus R_X and R_Y were set to $R_{i,j}/N$, in which N expresses the side length of the array. R_{REF} value is set according to Equation 4.3 to keep a constant range of the output resistance. The formula listed above does not include the limit of the op-amp output swing. If the op-amp output resistance is high, the internal voltage source sticks to the ground. If permitting op-amp negative output, the readout error appears like Figure 4.5. The negative voltage is expressed as $-n \cdot V_{REF}$. The retard of the rapid deterioration of the readout error is shown. However, the error is then saturated around 100 mV error.

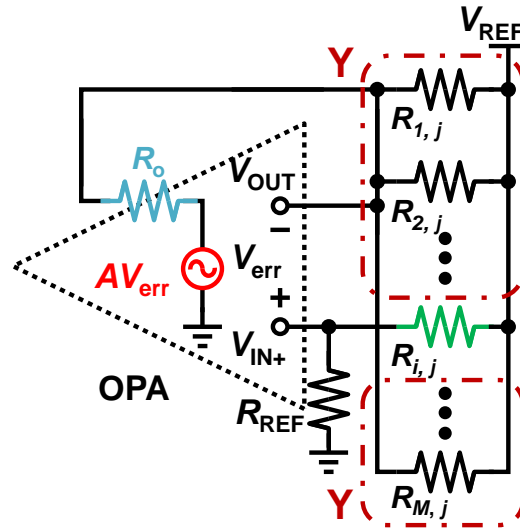


Figure 4.6 Model to calculate a combined conductance in the Y group.

4.2 Calibration by Op-Amp Nonidealities

In the previous section, the causes of the readout error are analyzed. In this section, the calibration method is introduced. It avoids using a higher output resistance than that satisfying Equation 4.3, and the proposed calibration decreases the error due to an op-amp's limited gain and an extensive array scale.

4.2.1 Calibration

Accurate resistance values are calculated by analyzing the effects of the resistors in both the X and the Y groups. However, it would require a large amount of calculation to solve the equation of both two effects so that the calculations are divided into two steps: a rough calculation, and an adjustment calculation. In a rough calculation, $R_{i,j}$ is calculated with the Y resistors. Figure 4.6 shows a schematic in which the circuit equation is established, in which the op-amp is expressed with the voltage source and an output resistor. It is assumed that R_{REF} is set as the value which makes V_{in+} around half V_{REF} and V_{err} is much smaller than V_{REF} . Then, the rest of the resistors are not taken into account. The

combined resistance when the i -th row and j -th column are selected is calculated as follows:

$$R_{Y(i,j)rough} = \frac{V_{REF} - V_{OUT(i,j)}}{V_{OUT(i,j)} - AV_{err(i,j)}} \cdot R_O \quad (4.8)$$

From this value, the sum of the conductance on the j -th column except $1/R_{i,j}$ is obtained. To calculate each resistance, all $R_{Y(i,j)}$ on the same column is required. After obtaining M numbers of $R_{Y(i,j)rough}$, which is to say $R_{Y(1,j)}$, $R_{Y(2,j)}$, \dots , $R_{Y(M,j)}$, $R_{i,j\text{ rough}}$ can be calculated.

$$\frac{1}{R_{i,j\text{ rough}}} = \frac{1}{M-1} \left(\sum_{k=1}^M \frac{1}{R_{Y(k,j)rough}} \right) - \frac{1}{R_{Y(i,j)rough}} \quad (4.9)$$

The sum of $1/R_{Y(1,j)}$, $1/R_{Y(2,j)}$, \dots , $1/R_{Y(M,j)}$ expresses the $(M-1)$ times added total conductance on the j -th column. By dividing it by $(M-1)$, the total conductance on the j -th column is obtained. Then, by subtracting $R_{Y(i,j)}$ from it, the i -th row and j -th column conductance are obtained.

Calculated $R_{i,j\text{ rough}}$ still contains the X resistors' effects. Figure 4.7 shows an equivalent circuit removing the resistors where no current flows. By using the resistance calculated in advance, the current flowing into X resistors can be estimated. Thus, the more accurate combined resistance can be calculated as follows:

$$\frac{V_{REF} - V_{OUT(i,j)}}{R_{Y(i,j)}} = \frac{V_{OUT(i,j)} - AV_{err(i,j)}}{R_O} + \frac{V_{err(i,j)}}{R_{X(i,j)}} \quad (4.10)$$

Here, $R_{X(i,j)}$ is the combined resistance in the X group and it is determined by the following equation.

$$\frac{1}{R_{X(i,j)}} = \left(\sum_{k=1}^N \frac{1}{R_{i,k\text{ rough}}} \right) - \frac{1}{R_{i,j\text{ rough}}} \quad (4.11)$$

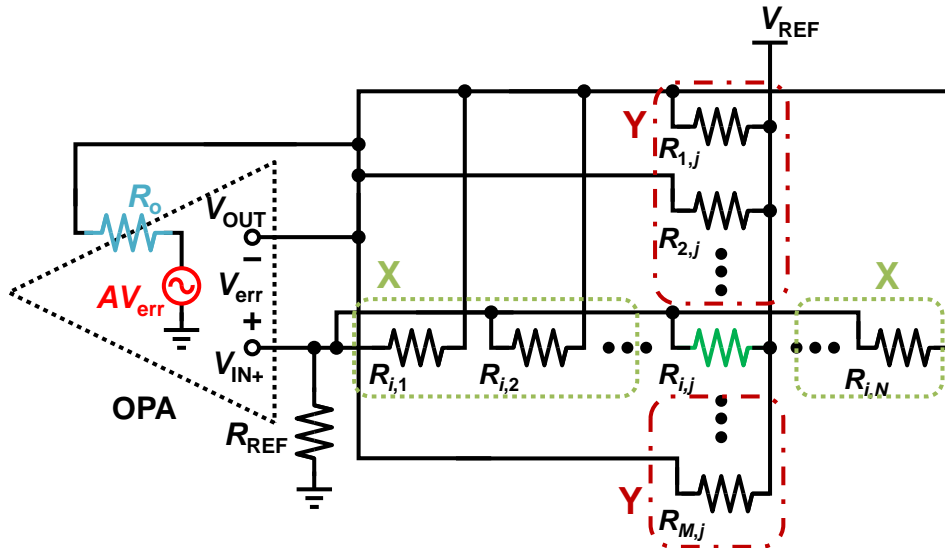


Figure 4.7 An equivalent circuit to calculate the array resistance removing the effects of a finite gain and an output resistance of the op-amp.

The resistance $R_{Y(i, j)}$ is calculated more accurately in Equation 4.10 than that in Equation 4.8. Finally, each resistance can be obtained by substituting $R_{Y(i, j)}$ into Equation 4.9.

4.2.2 Simulation Results

The target resistive array and a VF-NSE circuit were created in MATLAB / Simulink. As a reference voltage in simulations, 3.3 V was set because it was commonly used in the product ICs. Also, the range of an op-amp output voltage was limited from GND to V_{REF} . From the results described later, the reliable reading is not endorsed in the proposed calibration if the output resistance is larger than that satisfying Equation 4.3. Therefore, the negative output range was not necessary for the following simulations.

As for the simulations described in Section 4.1.2, the readout errors were analyzed, assuming all the sensor resistance values were the same. However, the distribution of the sensor resistance affects the X current, and thus the readout error becomes worse as the distribution rises. Thereby, resistance values were

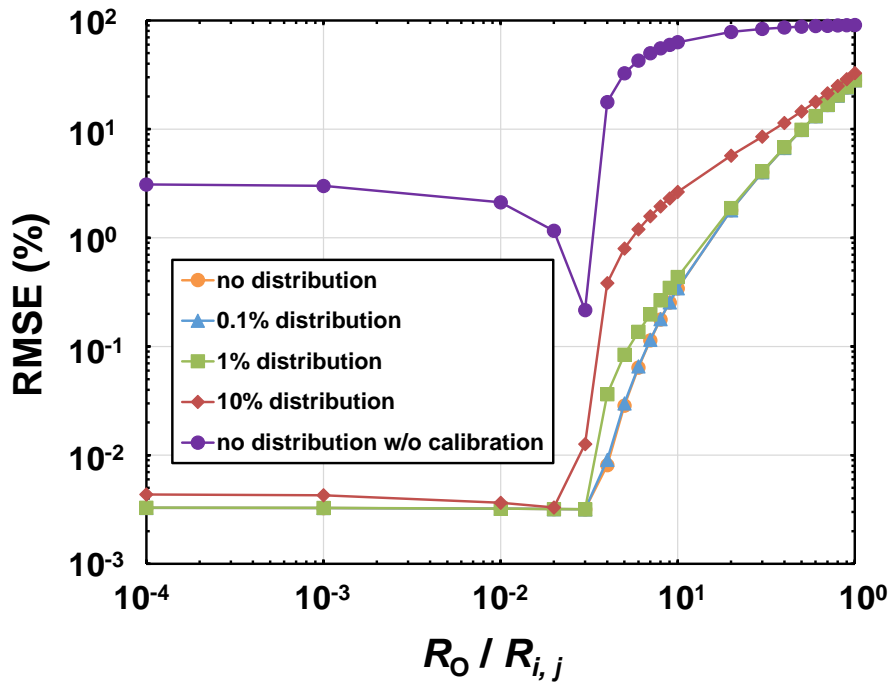


Figure 4.8 Readout error when calibration applied to resistance distributed array comparing with the non-calibrated VF-NSE method

normally distributed, and their variance percentage was parameterized. Figure 4.8 shows readout errors. Here, the readout error of a uniform resistive array without calibration was also evaluated to compare with the simplified circuit results described in Section 4.1. The left side on the graph, the output resistance was set to several orders smaller value than the average of sensor resistance. The results show that the method suppresses the error derived from a limited gain. However, on the opposite side, the RMSE increased even if the calibration was conducted. For reducing the computational complexity, the current of the X resistors is approximated to zero in Equation 4.8. Because the increase of the op-amp output resistance eliminated the output current and the rise of V_{err} , the op-amp output current is no more equivalent amount to the current in Y. Thereby, the approximate combined Y resistance could not be assessed with Equation 4.8. Although the simulation results showed some improvements in readout accuracy, it should be avoided to use the higher output resistance than that satisfies

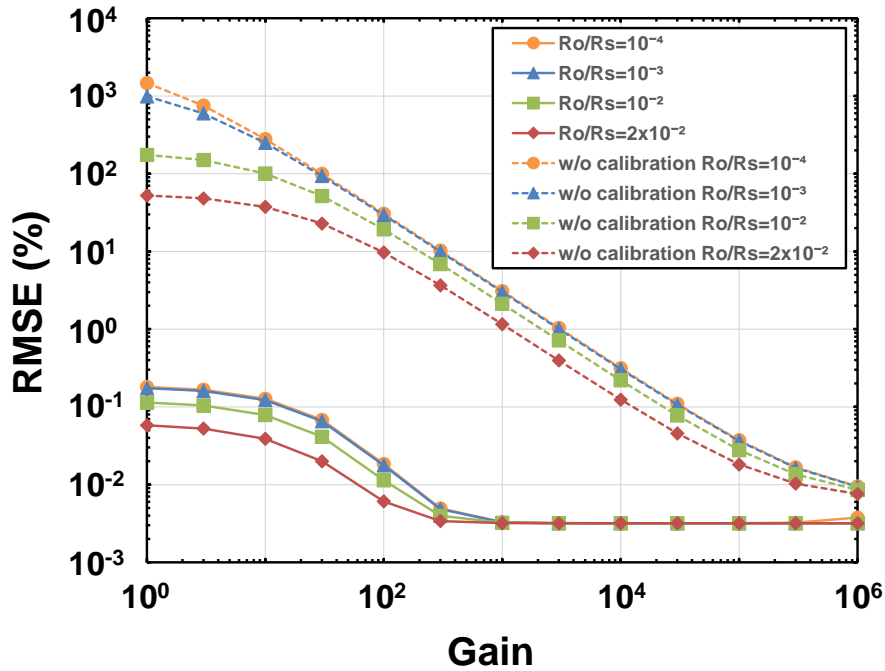


Figure 4.9 Readout error comparison with the non-calibrated VF-NSE method.

Equation 4.3. Especially if the resistance values are widely distributed, the readout accuracy performance becomes unreliable.

V_{err} is also affected by the op-amp gain, as shown in Equation 4.5. In order to decrease V_{err} , using a high gain op-amp is effective. Simulations with several conditions of an op-amp gain between 10^0 and 10^6 were carried out, comparing with the calibration-less results (Figure 4.9). The output values were set according to Equation 4.3. On the right side, where the gain is high, the RMSE results were saturated. Due to nonzero switch resistance was set in the simulations, the saturated value was almost a ratio of sensor resistance and the switch resistance. If the gain is low, the RMSE increases according to the original RMSE value. In the case that the gain is less than 100, the difference voltage of op-amp input nodes is mostly determined by the ratio of the sensor resistance

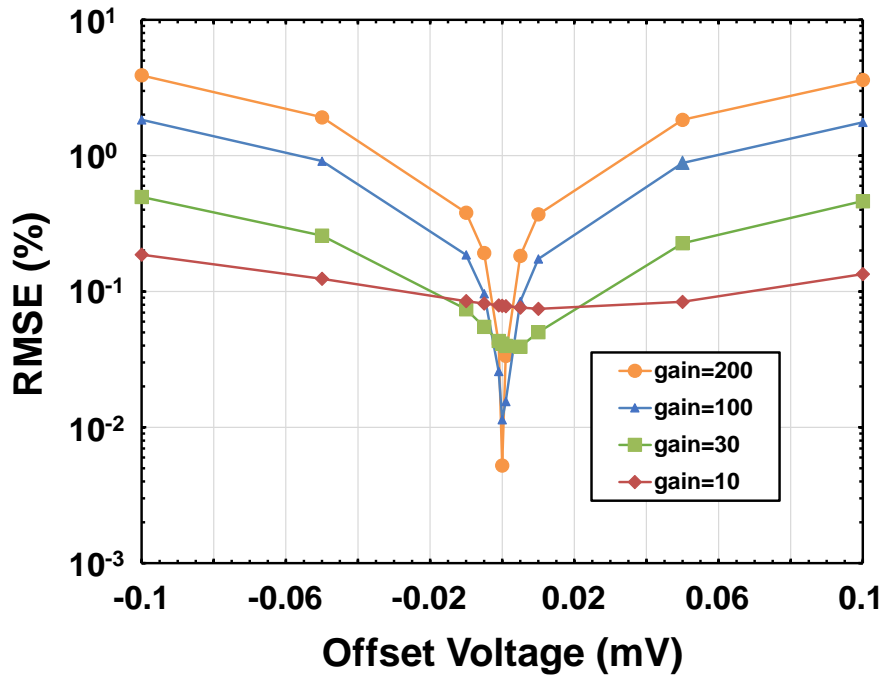


Figure 4.10 Readout error dependency on an op-amp offset voltage.

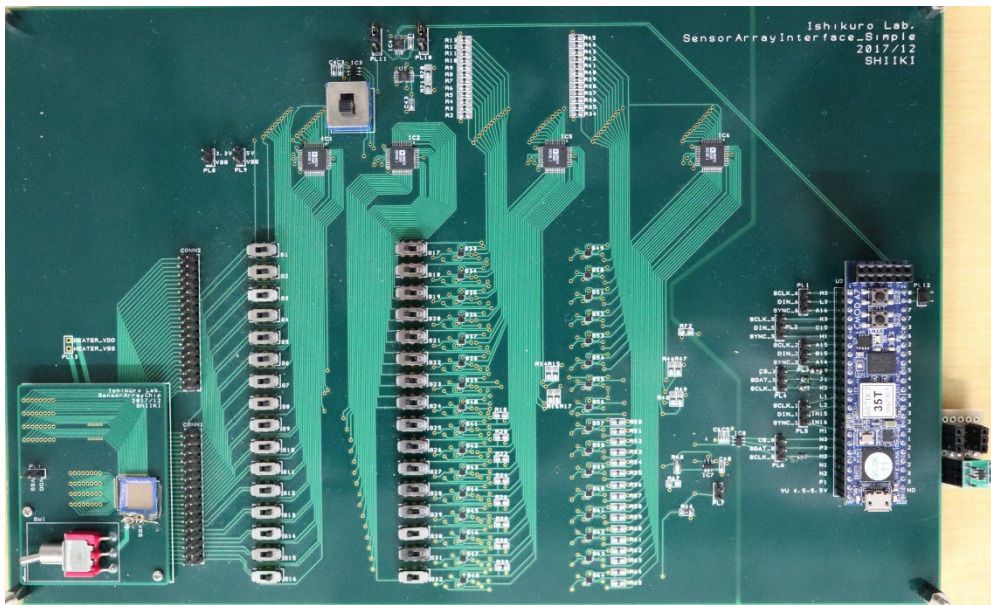
values and op-amp output impedance. Thus, the increasing gradient of the RMSE becomes gentle and they still maintain the RMSE of less than 0.2%. Compared with the RMSE of the noncalibrated readout, which was described in Section 4.1.2, the performance is enhanced.

Meanwhile, if the output resistance is designed with a proper value, the difference between V_{OUT} and AV_{err} keeps so small that the op-amp input offset voltage deteriorates the readout accuracy. The offset effects can be expressed with a correction of Equation 4.8.

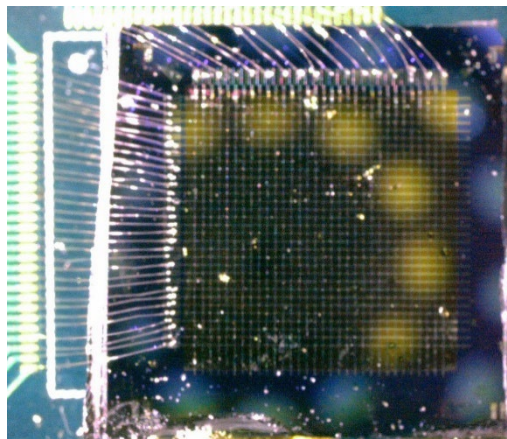
$$R_{Y(i,j)1st} = \frac{V_{REF} - V_{OUT(i,j)}}{V_{OUT(i,j)} - AV_{err(i,j)} + AV_{offset}} \cdot R_O \quad (4.12)$$

V_{offset} expresses the offset voltage, and it can take either a positive or negative value. As far as the op-amp output resistance is appropriately set, V_{OUT} and AV_{err} are almost the same. Thereby, the offset voltage term multiplied by the op-amp gain can significantly affect the calculation. The evaluation of the offset voltage

with some op-amp gain conditions was carried out (Figure 4.10). If the offset is close to zero, the accuracy gets enhanced as the gain takes a higher value. By contrast, if the absolute value of the offset value increases, the accuracy dependencies on the op-amp gain are reversed. Hence, a robust readout to an op-amp offset can be achieved with a low gain op-amp. With a high-performance offset cancel technique, a high gain op-amp is preferable to decrease RMSE.



(a)



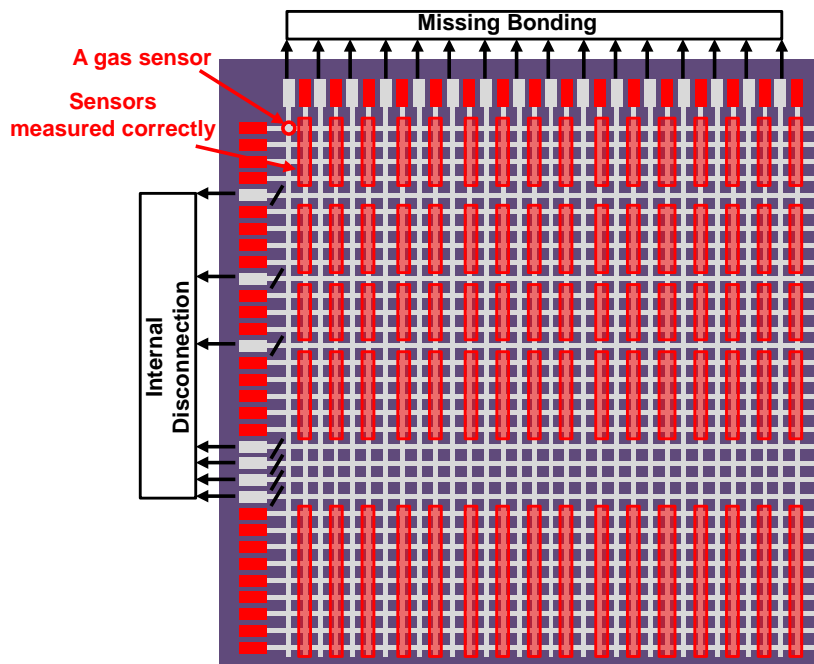
(b)

Figure 4.11 Prototype system (a) PCB (b) Gas Sensor chip.

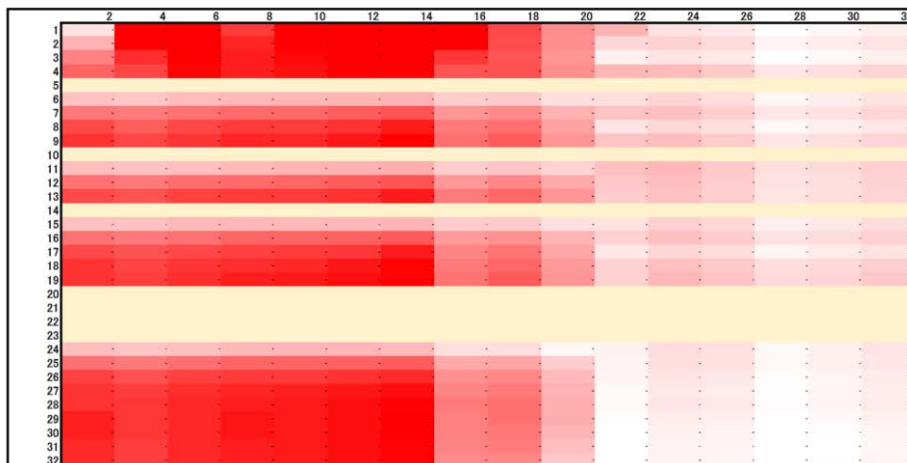
4.2.3 Prototype Design

Figure 4.11 shows the PCB and an actual gas sensor chip. The chip is connected to the interface circuit using a board connector. Discrete ICs of multiplexers (ADG731), switches (TS3A5223), an op-amp (MAX4475), ADCs (ADCS7476), and an FPGA (Cmod-A7) are used.

The actual gas sensor resistance values were measured, and the proposed calibration method was used for those values. Unfortunately, half of the column sensor resistance pads were not able to be obtained because of bonding defects, and some of the sensors which share the same row electrode were not able to be measured because of unexpected internal disconnection on the gas sensor chip. The sensors which were measured by the proposed method are shown in Figure 4.12 (a). Figure 4.12 (b) shows a 2D color map relating to the resistance value corresponding to the position of each sensor. In the 2D map, the unmeasured row sensor values are beige-colored and the unmeasured column sensor values are removed. The white area represents low resistance values, and the red area represents high resistance values. Most of the sensor resistance values are in the range of 300-4,000 Ω . For this measurement, each sensor was switched at a frequency of 62.5 kHz, thus all 1,024 sensors could be measured in around 16.4 msec. The on-resistance of the TS3A5223 switches is approximately 0.45 Ω from its datasheet. The ADCs are sampled at 1MS/sec. To use the proposed calibration method, the op-amp's output impedance was set to 930 Ω . It was based on the datasheet of MAX4475 showing its Frequency-Impedance line graph. The datasheet only shows the impedance up to 10 kHz of operating frequency. Therefore, the output impedance is an estimation calculated from the line graph. Instead of the unmeasured sensors' resistance, we used the interpolated resistances that were calculated from adjacent resistors in the software calibration. This is based on that the adjacent resistances have similar resistance values.



(a)

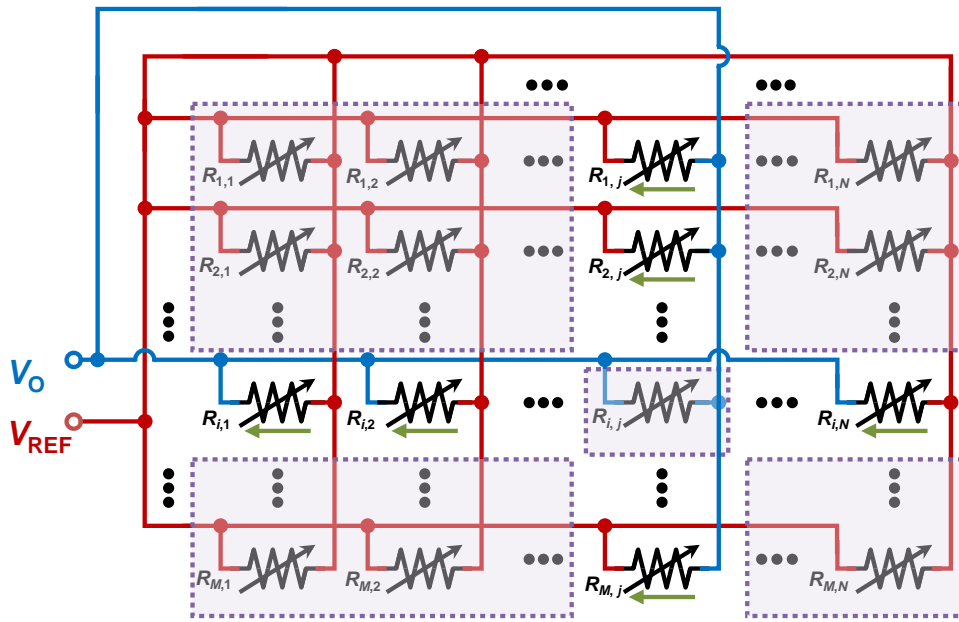


(b)

Figure 4.12 (a) Measured positions in the developed sensor chip
 (b) A heatmap graph of measured sensor resistances

4.3 Readout Methods without Op-Amps

From the above simulations, it was found that the proposed calibration method effectively improves the readout accuracy when the feedback op-amp parameters are properly designed. However, there have been some challenges to apply the calibration. One is the calibration requires the op-amp output resistance value and its gain. However, those factors can be influenced by environmental factors like temperature. Therefore, those effects should be analyzed based on experiments. Another is the ADC resolution. As the op-amp input offset can interfere with the accurate acquisition, the quantized error of sampling data can also influence the calculation results. Like an input offset, it could be solved by adjusting op-amp parameters. If the quantized error is larger than the op-amp input offset, the op-amp gain should be matched to it. If the error is unacceptably large, the ADC resolution should be improved. To address the issue, new readout methods called “Sneak-path-controlled Readout” (SPCR) and “Accurate SPCR” (ASPCR) are proposed. Compared with VFM and ZPM, SPCR and ASPCR do not use an op-amp to suppress sneak-path currents. Each resistance in a resistive matrix array is calculated by an established matrix equation. The interface circuits consist of ADCs and analog switches, which properly control sneak-path currents. The performance of scanning speed or readout accuracy is not affected by the settling time or offset voltage of an op-amp. In Section 4.3.1, the basic concept of the SPCR method is explained. In Section 4.3.2, an SPCR circuit is described, and the calculation of sensor resistance is explained. In Section 4.3.5, the resistance map in the case that the SPCR circuit yields large readout error is explained. An ASPCR circuit for a more robust readout than the SPCR circuit is given. In Section 4.3.6, the results of a simulation to evaluate readout accuracy are shown.

Figure 4.13 Circuit diagram with i -th row and j -th column selected

4.3.1 Readout Scheme

Based on a simple circuit design without an op-amp, the readout scheme is configured as follows. One of the row (m) electrodes of an $m \times n$ array is connected to a reference resistance connected to ground, while one of the column (n) electrodes is connected to a reference voltage. As for this scheme, a sneak current will flow into all the resistors in the array. To determine each resistance, matrix equations are required because the current flowing into target resistor cannot be measured directly. In several reported papers, the resistances are calculated by measuring voltages of all the electrodes, substituting the measured voltages as boundary conditions, and solving the matrix equations.

Even if an op-amp is not used, sneak currents can be controlled to make the matrix equations simple. Hereafter, array size is expressed as M columns and N rows (where M and N are natural numbers greater than 3). All the electrodes of the sensor array can be attached to either reference voltage V_{REF} or an output node (V_O). For different circuit configurations, V_O is measured $M \cdot N$ times. In each configuration, one of the column electrodes and one of the row electrodes

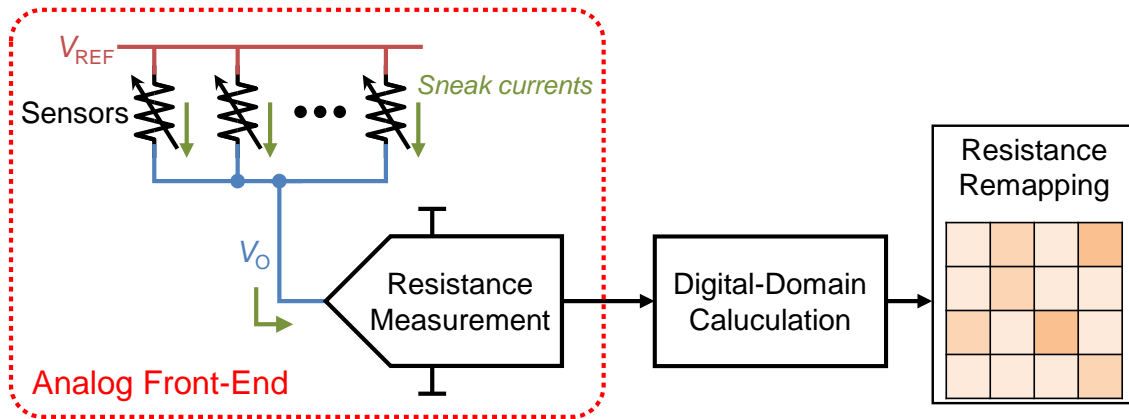


Figure 4.14 Flow of acquiring resistance.

are connected to V_O , and the other electrodes are connected to V_{REF} . A circuit in which the i -th-row and the j -th-column electrodes are connected to V_O is shown in Figure 4.13. (Hereinafter, this connection state is described as the i -th row and j -th column are selected.) The resistors, two ports of which are connected to the same voltage have no current through them. Those resistors can therefore be ignored during the calculation of resistance. If V_{REF} is higher than V_O , a current will flow through the rest of the resistors from V_{REF} to V_O . The resistance between the nodes of V_{REF} and V_O can be expressed as

$$R_{CmbRi} // R_{CmbCj} \quad (4.13)$$

where R_{CmbRi} is the parallel resistance of all the resistors (except $R_{i,j}$) sharing the i -th-row electrode, and R_{CmbCj} is the parallel resistance of all the resistors (except $R_{i,j}$) sharing the j -th-column electrode. These resistances are given as

$$R_{CmbRi} = R_{i,1} // R_{i,2} // \dots // R_{i,j-1} // R_{i,j+1} // \dots // R_{i,N} \quad (4.14)$$

$$R_{CmbCj} = R_{1,j} // R_{2,j} // \dots // R_{i-1,j} // R_{i+1,j} // \dots // R_{M,j} \quad (4.15)$$

By changing the connection state and obtaining the $M \cdot N$ pair of the parallel resistance, each resistance is calculated by the matrix calculation. Sensor resistance can thus be calculated with computational complexity of order N . The

overall flow is described in Fig. 3. Readout accuracy of the calculated resistance depends on the characteristics of switch parasitic resistances and the ADCs.

In this chapter, the effect of the switch on-resistance was compensated by measuring voltage at several points of a readout circuit. When using the switches with low on-resistance and using a high-resolution 16-bit ADC with a readout circuit, the SPCR method can measure each resistance accurately by measuring two ports in each connection state. Moreover, even if ADC quantization is relatively degraded, the resistance can be obtained in the case that all the resistances are normally distributed. As explained in the following sections, the readout error of the readout of two ADCs increases if the resistance distribution becomes large. To solve that problem, we propose a readout method—called accurate SPCR (ASPCR)—using three ADCs.

4.3.2 Sneak-Path-Controlled Readout

The interface circuit for SPCR is shown in Figure 4.15. Single-pole double-throw (SPDT) switches (“main switches”) and single-pole single-throw (SPST) switches (“sub switches”) are attached to the all the electrodes. One port of the main switches is connected to reference voltage V_{REF} , and the other port is connected to reference resistance R_{REF} and the main ADC. The main switches control the connection states for $M \cdot N$ times. In each state, one of the row electrodes and one of the column electrodes are connected to R_{REF} , while the others are connected to V_{REF} . When the i -th-row switch and the j -th-column switch are selected, the sub switches on the same electrode are turned on. Under the assumption that the current flowing through the main switches is larger than that flowing through the sub switches to the extent that the voltage drop across the sub switches can be ignored, the voltage drop across the main switches can be measured as the voltage difference between the main ADC and the sub ADC. R_{SWon} and R_{SWoff} represent on-resistance and off-resistance of the main switches, and $R_{\text{SW'on}}$ and $R_{\text{SW'off}}$ represent on-resistance and off-resistance of the sub

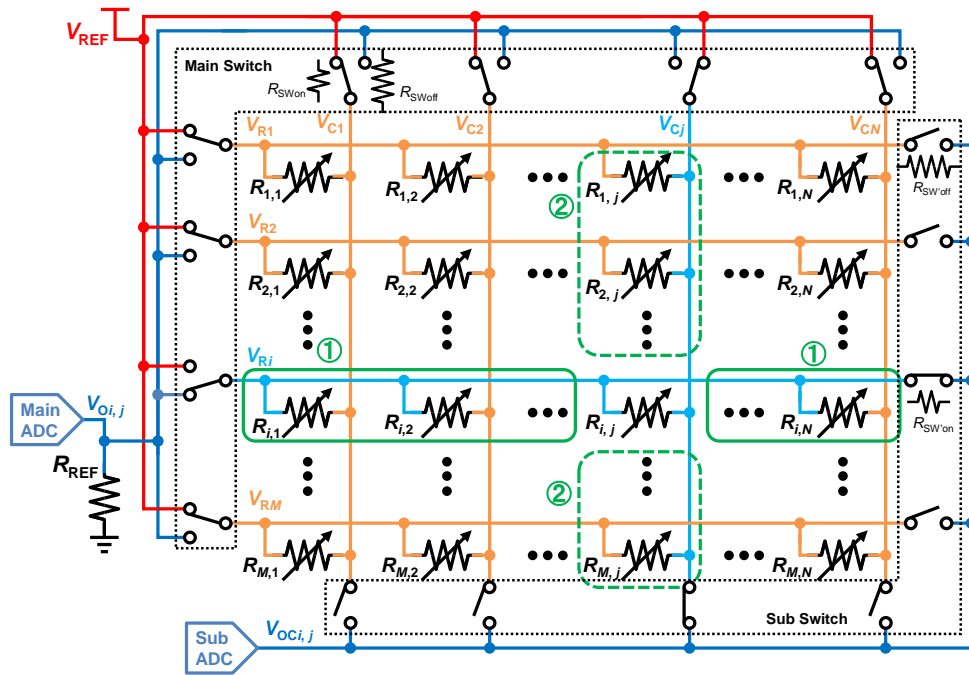


Figure 4.15 Sneak-path-controlled circuit

switches. In the case of ideal switches, compared to the sensor resistance, R_{SWon} is much smaller and R_{SWoff} is much higher. Although current flows through all the switches, the voltage drop of the unselected electrodes is so small that the voltage almost equals V_{REF} . For the same reason, the current does not flow into $R_{i,j}$, and the resistances only $R_{CmbRi,j}$, and $R_{CmbCi,j}$ form a resistive voltage-divided circuit with R_{REF} .

4.3.3 Calculation of Resistance

The equivalent circuit of the interface circuit can be simplified by removing the zero-current resistors and the ideal switches. The simplified circuit, which consists of $R_{CmbRi,j}$, $R_{CmbCi,j}$, and R_{REF} is shown in Figure 4.16. The resistance between V_{REF} and V_O is expressed as Equation 4.13. If the i -th row and j -th column are selected, output voltage $V_{O_{i,j}}$ is expressed as

$$V_{O_{i,j}} = V_{REF} \cdot \frac{R_{REF}}{(R_{CmbRi,j} \parallel R_{CmbCi,j}) + R_{REF}} \quad (4.16)$$

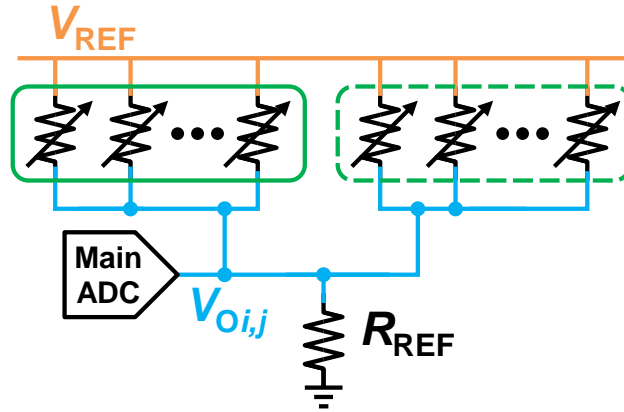


Figure 4.16 Simplified circuit with resistors with no sneak current removed

The $M \cdot N$ switching-circuit configuration establishes $M \cdot N$ equations of Equation 4.16 so that those equations create the following matrix equation:

$$\frac{1}{R_{REF}} \begin{bmatrix} V_{O1,1} \\ V_{O1,2} \\ \vdots \\ V_{OM,N} \end{bmatrix} = \mathbf{V} \mathbf{A} \begin{bmatrix} 1/R_{1,1} \\ 1/R_{1,2} \\ \vdots \\ 1/R_{M,N} \end{bmatrix} \quad (4.17)$$

Matrix \mathbf{V} , which denotes measured output voltage, and matrix \mathbf{A} , which denotes the combination of parallel resistances are expressed as

$$\mathbf{V} = \begin{bmatrix} V_{REF} - V_{O1,1} & 0 & \cdots & 0 & 0 \\ 0 & V_{REF} - V_{O1,2} & \cdots & 0 & 0 \\ \vdots & \vdots & \ddots & \vdots & \vdots \\ 0 & 0 & \cdots & V_{REF} - V_{OM,N-1} & 0 \\ 0 & 0 & \cdots & 0 & V_{REF} - V_{OM,N} \end{bmatrix} \quad (4.18)$$

$$\mathbf{A} = \begin{bmatrix} 0 & 1 & \cdots & 0 & 0 \\ 1 & 0 & \cdots & 0 & 0 \\ \vdots & \vdots & \ddots & \vdots & \vdots \\ 0 & \cdots & 0 & 1 & 0 \\ 0 & 0 & \cdots & 1 & 0 \end{bmatrix} \quad (4.19)$$

If matrix \mathbf{A} has an inverse matrix \mathbf{A}^{-1} , all the resistances can be calculated.

4.3.4 Calibration of Switch Resistance

So far, the situation, in which the effect of switch resistance can be ignored, was focused on. However, if the switch resistance is not calibrated, readout error will increase in accordance with the ratio of sensor resistance and switch resistance. In fact, completely eliminating switch resistance impact requires large computation cost. However, in the case that array resistances are distributed in the range of around 10% of sensor resistance, readout accuracy can be improved. As shown in Figure 4.17, the simplified circuit is modified by adding switch resistance to estimate non-ideal switch effects. As a result, the relation between $V_{O_{i,j}}$ and sensor resistance is given as

$$V_{O_{i,j}} = \frac{V_{\text{REF}} \cdot R_{\text{REF}}}{\left\{ (R_{\text{SWon}} + R'_{\text{CmbR}_{i,j}}) \parallel (R_{\text{SWon}} + R'_{\text{CmbC}_{i,j}}) \parallel \frac{R_{\text{SWoff}}}{M+N} \right\} + R_{\text{REF}}} \quad (4.20)$$

where $R'_{\text{CmbR}_{i,j}}$ and $R'_{\text{CmbC}_{i,j}}$ are the resistances when the sensor resistors and switch resistors are connected in parallel as follows:

$$R'_{\text{CmbR}_{i,j}} = (R_{i,1} + R_{\text{SWon}}) \parallel (R_{i,2} + R_{\text{SWon}}) \parallel \cdots \parallel (R_{i,j-1} + R_{\text{SWon}}) \parallel (R_{i,j+1} + R_{\text{SWon}}) \parallel \cdots \parallel (R_{i,M} + R_{\text{SWon}}) \quad (4.21)$$

$$R'_{\text{CmbC}_{i,j}} = (R_{1,j} + R_{\text{SWon}}) \parallel (R_{2,j} + R_{\text{SWon}}) \parallel \cdots \parallel (R_{i-1,j} + R_{\text{SWon}}) \parallel (R_{i+1,j} + R_{\text{SWon}}) \parallel \cdots \parallel (R_{M,j} + R_{\text{SWon}}) \quad (4.22)$$

Equation 4.20 holds on the assumption that V_{R_1}, \dots, V_{R_M} and V_{C_1}, \dots, V_{C_N} are almost equal to V_{REF} . The effect of switch off-resistance increases in proportion to the number of main switches. Since R_{SWoff} is divided by $M+N$, it is not necessary to consider the R_{SWoff} variation. Thus, the typical value of R_{SWoff} can be utilized effectively to compensate off-resistance impact on readout accuracy. By substituting the typical off-resistance, the setting parameters V_{REF} and R_{REF} , and the measured value $V_{O_{i,j}}$ with Equation 4.20, the value of the rest term $(R_{\text{SWon}} + R'_{\text{CmbR}_{i,j}}) \parallel (R_{\text{SWon}} + R'_{\text{CmbC}_{i,j}})$ can be obtained. On the contrary,

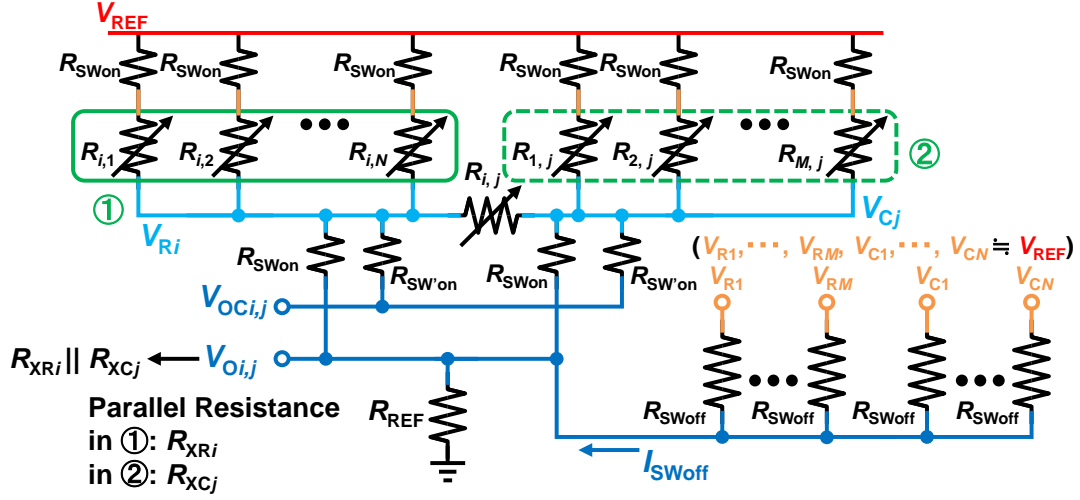


Figure 4.17 Simplified circuit considering switch resistance

R_{SWon} is determined by measuring $V_{OCi,j}$ because on-resistance variance directly affects readout resistance. R_{SWon} is therefore calculated as

$$R_{SWon} = \frac{2(V_{OCi,j} - V_{Oi,j})}{\frac{V_O}{R_{REF}} - I_{SWoff}} \quad (4.23)$$

where I_{SWoff} denotes the current flowing into R_{REF} through R_{SWoff} and is given as

$$I_{SWoff} = (M + N) \cdot \frac{V_{REF} - V_{Oi,j}}{R_{SWoff}} \quad (4.24)$$

If the array resistances are normally distributed, it is assumed that

$$R_{CmbRi,j} \approx R_{CmbCi,j} \quad (4.25)$$

Based on Equation 4.23, the following formula is established:

$$(R_{SWon} + R'_{CmbRi,j}) \parallel (R_{SWon} + R'_{CmbCi,j}) = \frac{R_{SWon} + R'_{CmbRi}}{2} \quad (4.26)$$

If R_{SWon} is subtracted from Equation 4.24, $R'_{CmbRi,j}$ and $R'_{CmbCi,j}$, which can be transformed to $R'_{CmbRi,j} \parallel R'_{CmbCi,j}$, are obtained. Since Equation 4.17 cannot be

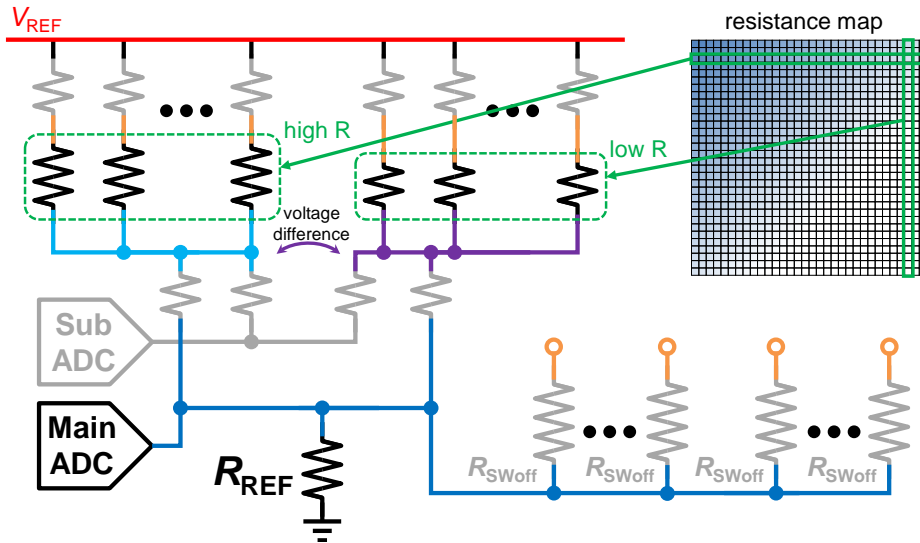


Figure 4.18 Case study with different resistances on selected column and selected row. The equivalent circuit indicates that the bias voltage applied to the sensor differs on selected row and column electrodes.

directly applied due to R_{SWon} , Equation 4.17 is transformed to Equation 4.25 based on Equations 4.21 and 4.22:

$$\frac{1}{R_{REF}} \begin{bmatrix} V_{O1,1} \\ V_{O1,2} \\ \vdots \\ V_{ON,M} \end{bmatrix} = \mathbf{VA} \begin{bmatrix} 1/(R_{1,1} + R_{SWon}) \\ 1/(R_{1,2} + R_{SWon}) \\ \vdots \\ 1/(R_{M,N} + R_{SWon}) \end{bmatrix} \quad (4.27)$$

After acquiring $M \cdot N$ sets of $R'_{CmbRi,j} // R'_{CmbCi,j}$, it is possible to calculate each resistance from Equation 4.25.

4.3.5 Accurate Sneak-Path-Controlled Readout

In SPCR, resistance is precisely calculated without large computation cost only if the switches have ideal characteristics or the array resistances are obtained under the assumption given by Equation 4.23. On the contrary, if the resistance distribution becomes larger, readout accuracy may decrease. In the resistive map shown in Figure 4.18, the combined resistance of the selected row and the combined resistance of the selected column differ significantly. As the voltage

gap between V_{Ri} and V_{Cj} is widened, the relations between output voltage and matrix resistance expressed by Equations 4.16 and 4.20 do not hold. Even if only one sensor has low resistance, the resistors sharing the same electrodes cannot be measured. Moreover, readout error of the combined resistance is propagated among all resistances calculated in the matrix equation.

To avoid readout deterioration and ensure robust measurement, the difference between V_{Ri} and V_{Cj} should be measured and utilized in the following resistance calculation. As shown in Figure 4.19(a), the row's sub-switches and the column's sub-switches of the sensor array are split, and the sub-ADC respectively detects each voltage. When the i -th row and j -th column are selected, the following equations are established on the basis of the simplified circuit shown in Figure 4.19(b).

$$R_{SWon} = \frac{V_{CmbRi,j} + V_{CmbCi,j} - 2V_{Oi,j}}{\frac{V_O}{R_{REF}} - \frac{V_{REF} - V_{Oi,j}}{R_{SWoff}}} \quad (4.28)$$

$$\frac{V_{REF}}{R'_{CmbRi,j}} + \frac{V_{REF}}{R'_{CmbCi,j}} = \frac{V_{Oi,j}}{R_{REF}} - (M + N) \frac{V_{REF} - V_{Oi,j}}{R_{SWoff}} \quad (4.29)$$

A matrix equation for calculating each resistance can be established in the same way with SPCR from Equation 4.29. Although the voltages of the three nodes must be measured, resistance can be acquired stably without relying on the assumption given by Equation 4.25.

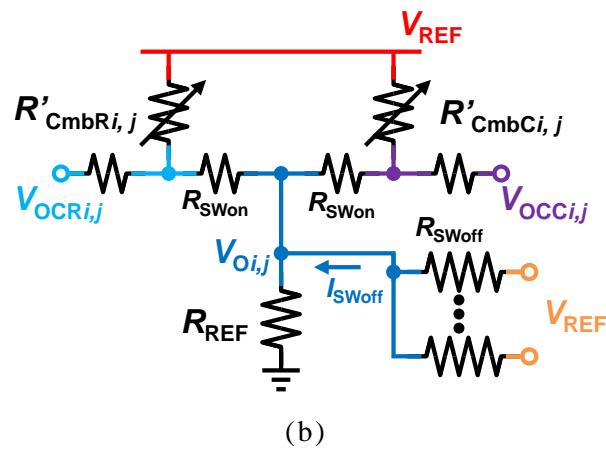
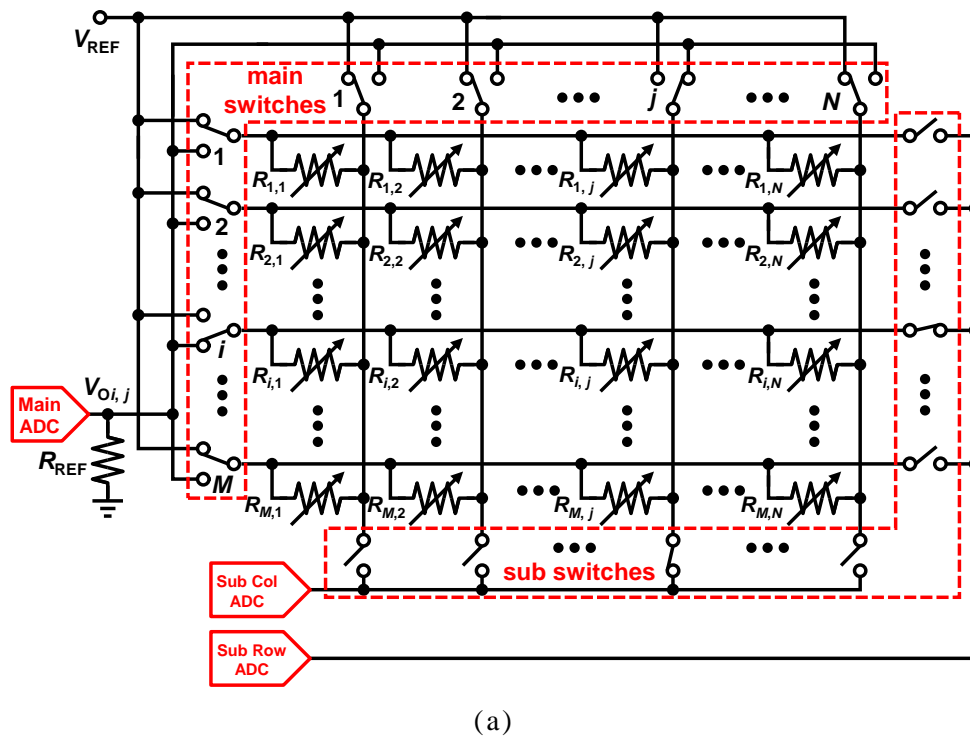


Figure 4.19 Circuit for accurate control of readout and (b) equivalent circuit

4.3.6 Simulation Results

The proposed methods for SPCR and ASPCR were verified by simulations by MATLAB/Simulink. The scale of a matrix array was set to $M = 32$, $N = 32$. Since the analog switches and ADCs were the major cause of readout error, their effects were evaluated first by using SPCR. In the case of SPCR, the main switches have larger current than the sub switches when they are closed. Thus, their switch resistances affect readout error differently. R_{SWon} and R_{SWoff} of the main switches and sub switches were respectively configured. All matrix resistances were set to $100 \text{ k}\Omega$, and R_{REF} was set to $1.5 \text{ k}\Omega$. Readout accuracies of the SPCR calculation without calibration Equation 4.17 and with calibration Equation 4.27 are compared in Figure 4.20. Various values of main-switch resistance and sub-switch resistance were set. The switch calibration was verified by comparing the results obtained without calibration to those obtained with calibration. The horizontal axis denotes switch on-resistance in Figure 4.20(a) and switch off-resistance in Figure 4.20(b). Instead of absolute values, the ratio of the switch resistances and array resistances was used because the relative value is significant for the readout error.

The readout error on the vertical axis is expressed as the root-mean-square error (RMSE), which is quantified as

$$\text{RMSE}(\%) = \frac{1}{M + N} \sum_{i=1}^M \sum_{j=1}^N \left(100 \cdot \frac{|R_{\text{true } i,j} - R_{\text{measured } i,j}|}{R_{\text{true } i,j}} \right) \quad (4.30)$$

where R_{true} is the set resistance value in the simulations, and R_{measured} is the calculated resistance. While resistance of the main switch or the sub switch is parameterized, the other fixed resistances were set as R_{SWon} : $0.1 \text{ }\Omega$ and R_{SWoff} : $10 \text{ G}\Omega$ for main switches and R_{SWon} : $0.1 \text{ }\Omega$ and R_{SWoff} : $100 \text{ G}\Omega$ for sub switches.

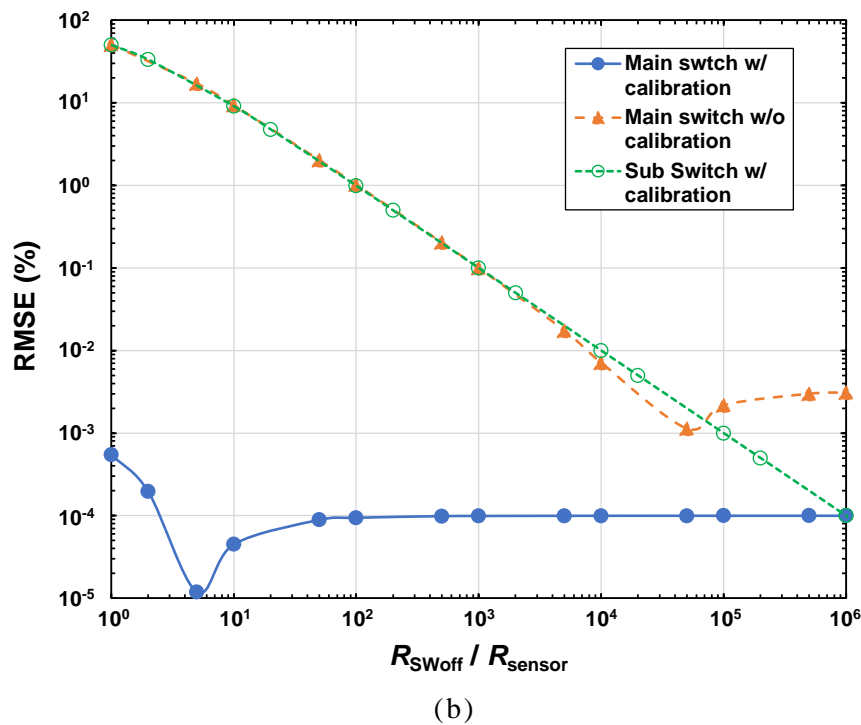
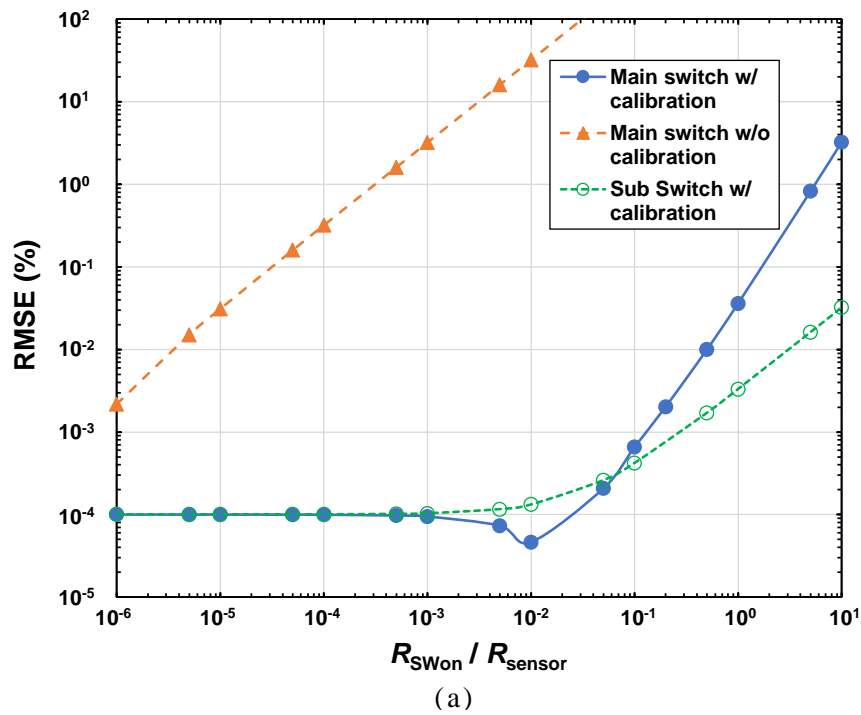


Figure 4.20 Comparison of readout accuracy when SPCR is used. RMSE is improved by the switch-resistance-calibrated readout. (a) Simulation results obtained with parameterized switch on-resistance and (b) Simulation results obtained with parameterized switch off-resistance.

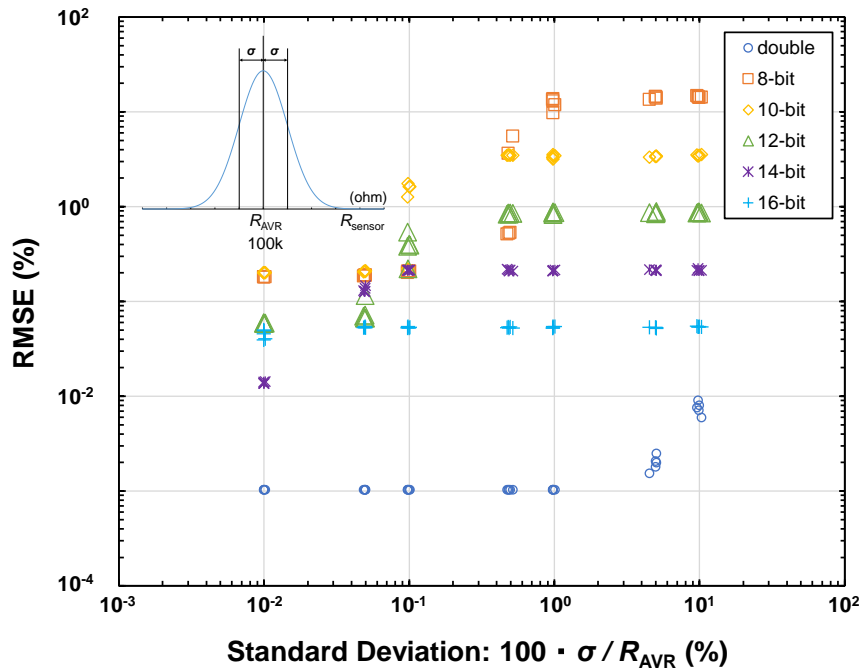


Figure 4.21 Degradation of accuracy of SPCR due to ADC quantized error. Max. input voltage of ADC is 3.3V when VREF is set to 3.3 V.

From the results of the above switch-resistance simulations, the switches can be designed properly according to required accuracy. However, the comprehensive readout accuracy is also affected by the quantized error of the ADCs. For example, if a 12-bit ADC is used, the readout error will be $2.44 \times 10^{-2}\%$ at minimum. Besides, since SPCR requires a matrix equation to calculate each resistance, the quantized error of even one sensor affects all resistances. Since the quantized error should be examined in a general way, the matrix resistance was normally distributed. A random number sequence was generated with a `randn()` function in MATLAB, and the standard deviation was parameterized. The results of the simulations are shown in Figure 4.21. The average value of the matrix resistances was fixed to around 100 k Ω . The horizontal axis indicates the standard deviation, in which 10% means nearly 696 resistances out of 1,024 resistances are within $100 \text{ k}\Omega \pm 10 \text{ k}\Omega$. Quantized resolutions were set to 8-bit, 10-bit, 12-bit, 14-bit, and 16-bit. The almost infinite resolution is also expressed as a double type in MATLAB. The resistances of the analog switch were set to 100 Ω for on-resistance and 10 G Ω for off-resistance.

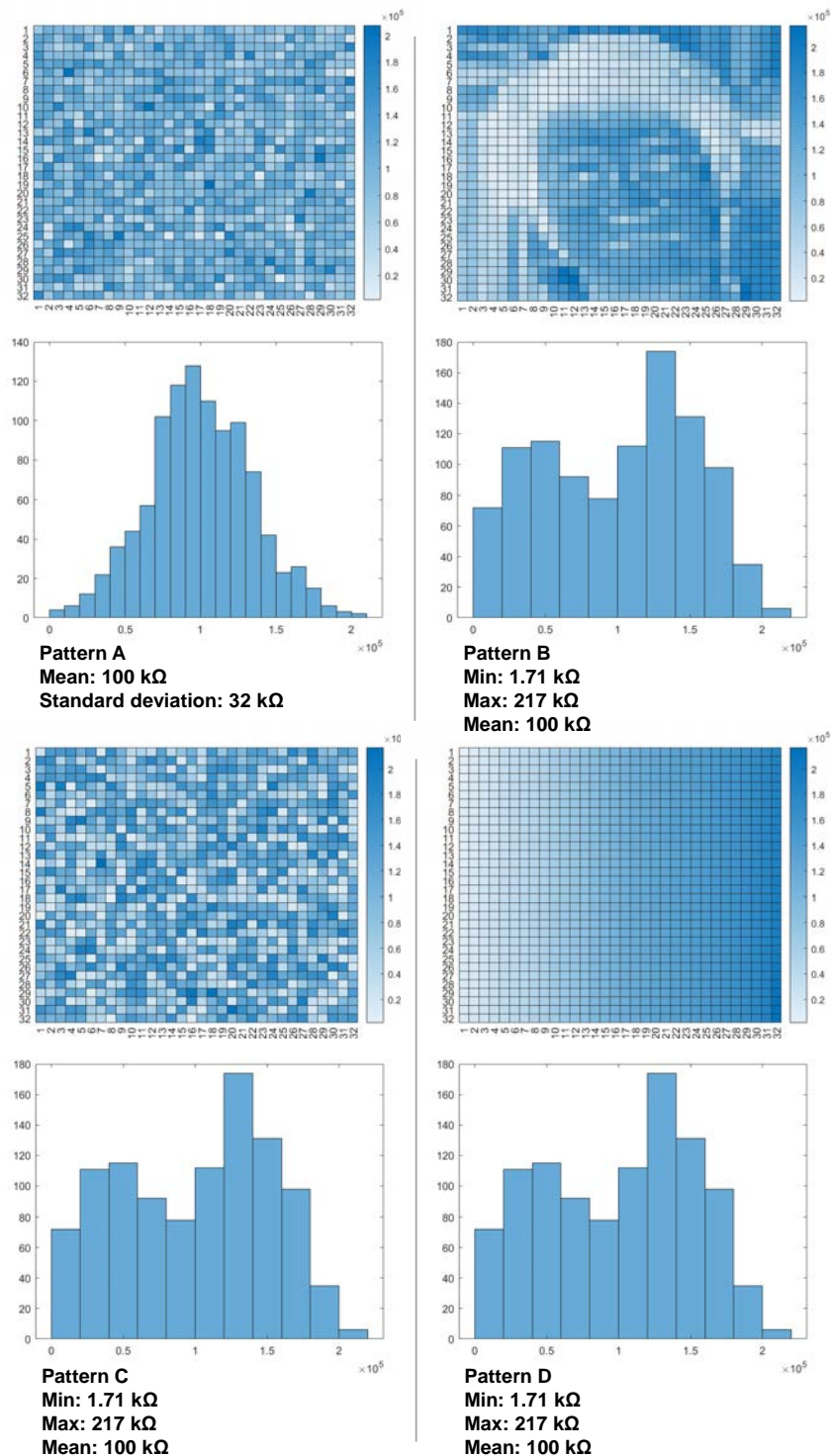


Figure 4.22 Tested resistance patterns: pattern A, generated by the `randn()` function in MATLAB, is normally distributed; pattern B is an image converted from the picture of a person's face; pattern C contains the same sensor resistances as pattern B, but it is randomly rearranged. Pattern D contains the same sensor resistances as pattern B, except the resistances are sorted. The histograms for each pattern are shown.

From the previous simulation results shown in Figure 4.20, these switch resistances correspond to around RMSE readout performance of 10^{-3} at minimum. The selected standard deviation of sensor resistance was about 10^{-2} , 5×10^{-2} , 10^{-1} , 5×10^{-1} , \dots , 10^1 , and in each step, five different distributions were generated. It is concluded from these results that the 10% distribution of the sensor resistances degrades readout accuracy, but still quantized error determines overall readout accuracy significantly.

As explained in Section 4.3.5, readout accuracy in the case of SPCR is related to resistance distribution. Although the measured electrode voltages in the case of SPCR are less than those in the case of ASPCR, resistance can be precisely calculated if the resistances are not largely distributed so that Equation 4.25 holds. The relation between resistance variation and readout RMSE was investigated.

Table 4.1 Readout error with SPCR

	A	B	C	D		
SPCR	8-bit	21.5	> 100	> 100	31.5	RMSE (%)
	10-bit	4.42	27.0	15.3	9.30	
	12-bit	1.59	32.0	6.22	6.99	
	14-bit	1.13	29.5	5.71	6.61	
	16-bit	1.09	28.8	5.61	6.62	
	double	1.10	28.7	5.63	6.62	

Table 4.2 Readout error with ASPCR

	A	B	C	D		
ASPCR	8-bit	11.9	30.5	31.1	15.1	RMSE (%)
	10-bit	2.97	4.57	4.84	3.56	
	12-bit	0.691	1.15	1.10	0.975	
	14-bit	0.177	0.332	0.287	0.270	
	16-bit	4.69×10^{-2}	0.248	8.56×10^{-2}	0.153	
	double	1.14×10^{-2}	0.249	5.10×10^{-2}	0.145	

As shown in Figure 4.22, four different resistance patterns were tested. Pattern A is normally distributed and generated in the same way as the previous simulations. The rest of the patterns were generated from the same resistances. Pattern B is generated from a picture. Pattern C is randomly arranged. Pattern D is generated from sorting the values of resistances. Each resistance pattern was created and scanned by SPCR and ASPCR. RMSE of the simulated results is listed in Table 4.1 and Table 4.2. In these simulations, switch on-resistance was 100Ω and off-resistance was $10 \text{ G}\Omega$. Reference resistance R_{REF} was set to $1.5 \text{ k}\Omega$. It is shown that the inclination of the resistance pattern clearly caused the deterioration in readout accuracy in the case of SPCR. On the contrary, ASPCR avoided the effect of the pattern inclination. As for the same histogram sensor arrays, the randomly distributed pattern could be read more accurately than the other two patterns.

4.4 Demonstration

To measure sensor's resistance, an SPCR circuit was implemented with product ICs on a PCB. A developing sensor chip was measured and the heatmap was created with the system. However, most of the sensor chips had a few defects due to the early stage of development and several resistances were unexpectedly low. Moreover, the sensor resistance did not appear on output voltage because switch resistance and metal-wire resistance are high compared to the low resistance sensors. To avoid error of the measured voltage from propagated in a matrix equation, a linear interpolation was installed. If unexpected condition's sensor is detected, its resistance is calculated by the adjacent resistance. Figure 4.24 describes the data conditioning.

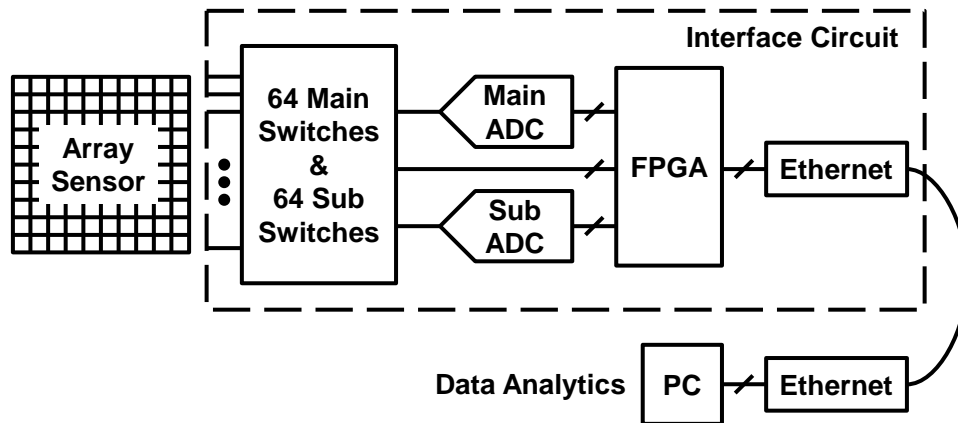


Figure 4.23 Block design of a developed system

4.4.1 Designed PCB

A block design of a developed system was shown in Figure 4.23. The size of a measured sensor chip is 32×32 , and 1,024 sensors are integrated into it. As the main switches and sub switches, ADG734 was selected, and to control its select pins, ADG732 was selected. Since ADG734 includes 4 analog switches in one package, 16 of them are mounted on the PCB. As ADCs, 12-bit ADC, ADCS7476, was used.

The data acquisition sequence was controlled by an FPGA board, called Cmod A7-35T. At the first sequence, PC sends a command to FPGA via an ethernet. Then, the FPGA receives a command and starts an operation of data acquisition from a sensor. After 1,024 states of switch configurations are formed and their output voltages are measured by ADCs, the data are streamed to the PC via ethernet. Matrix equations based on the measured voltages are established and calculated in the PC. The PCB was designed with KiCAD, an EDA tool, and the schematic is shown in Figure 4.25. An implemented PCB and a sensor chip are shown in Figure 4.26. After calculating each resistance with Python, a heatmap of sensor resistances was created (Figure 4.27).

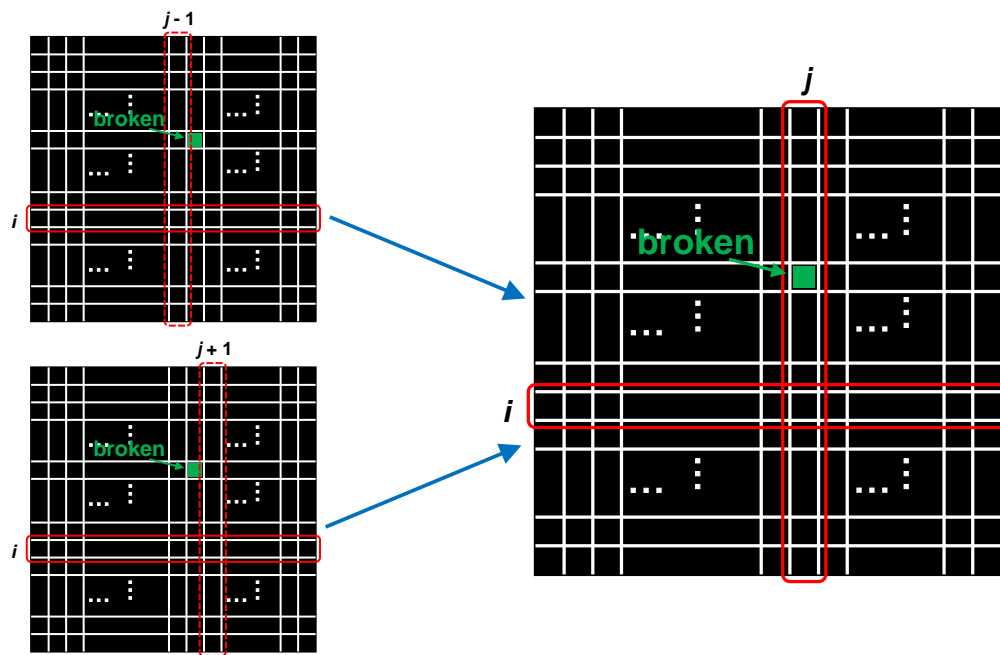


Figure 4.24 Pre-complementation

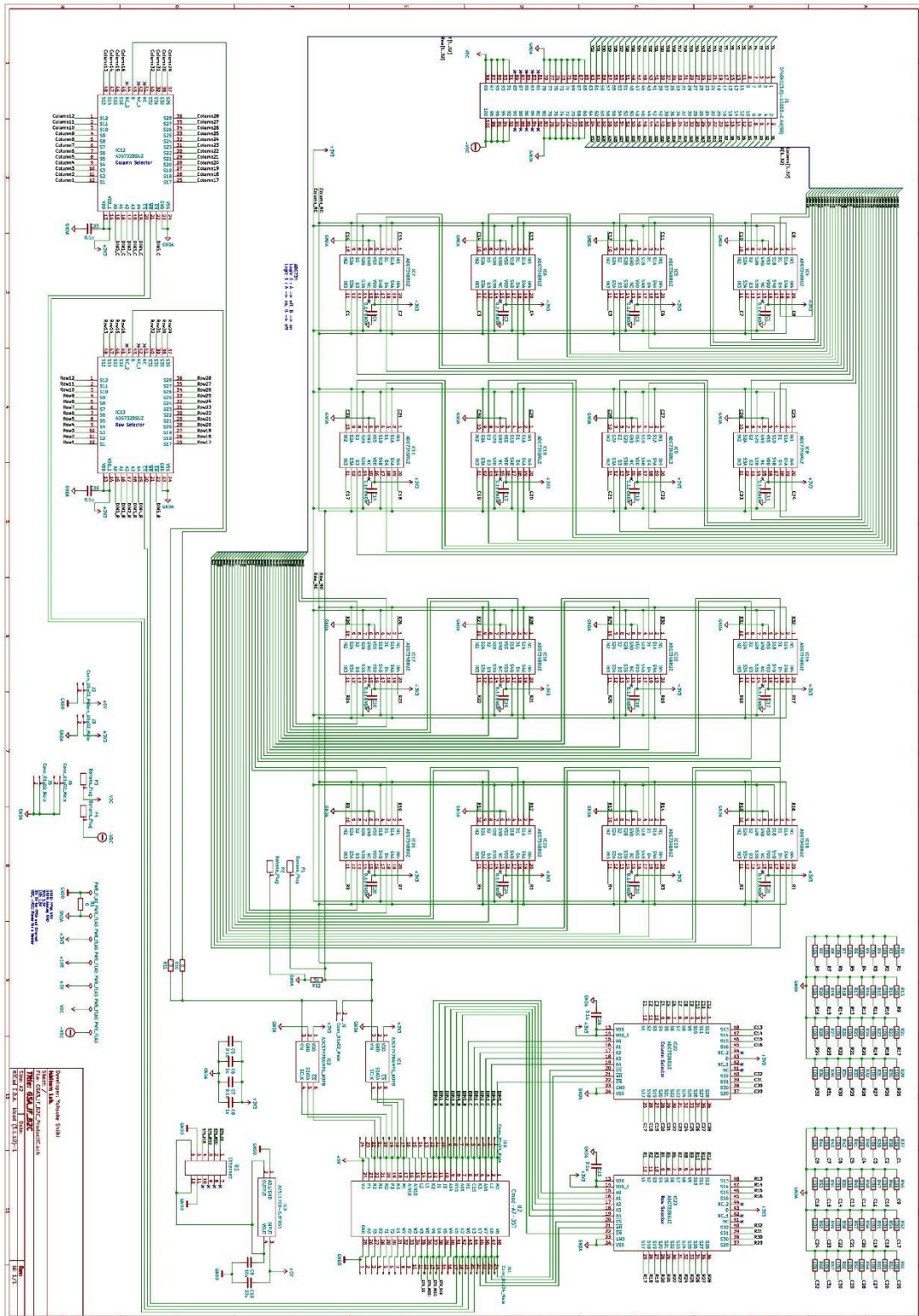


Figure 4.25 Schematic of a designed PCB.

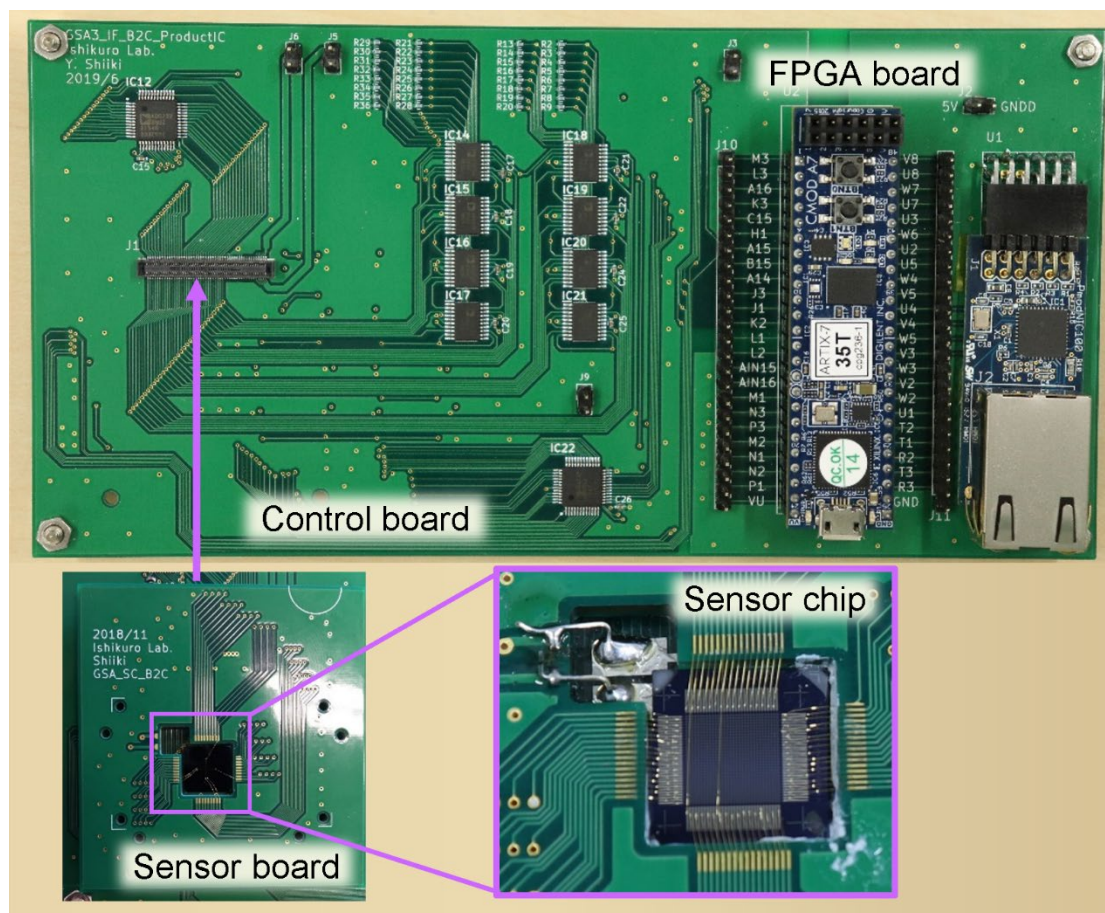


Figure 4.26 A developed PCB and a sensor chip

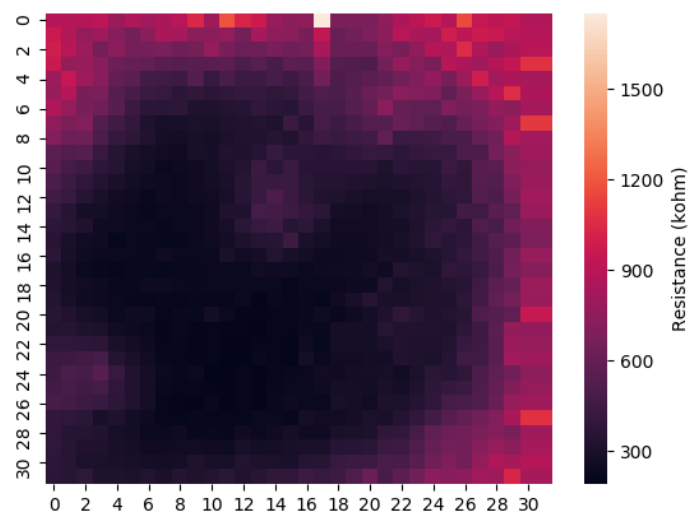


Figure 4.27 Heatmap of measured resistances with SPCR

Chapter 5

System for Integrated Self-Heated Sensors

It is challenging to fabricate hundreds of types of sensors into a small chip with many materials. Using the temperature dependency of the metal-oxide sensors is one of the practical ways to integrate various types of sensors. With the temperature dependency, it is possible to utilize the same type of sensors as if they were different. This approach is referred to as “sensor emulation” in this context. From the perspective of hardware implementation, its interface circuit of the sensors has an important role to control the different temperatures. However, generating various voltages to set a target temperature for sensors makes the sensory system large. Moreover, the power consumption would increase proportionally as the number of the sensor rises if the sensor is operated independently in a conventional way. Therefore, a new pulse-measurement system is considered which performs in the way described in Section 2.2.3. In this chapter, the constant-power and pulse-measurement system is implemented and evaluated. In the last section of this chapter, the developed self-heated sensors are measured which compact model is created in Chapter 3. In addition to this, data comparisons are made between a conventional continuous measurement and the proposed pulse measurement to ensure the sensor emulation is achieved.

5.1 Circuit Design

To use an electronic nose in real-time applications or IoT devices, power consumption should be kept as low as possible, and the size of the system should be maintained small. For IoT application, the input voltage of the whole circuit is determined as 3.3 V, which can be extracted from a Li-ion battery. Although self-heated sensors are operated with mW-power consumption, the total consumption becomes large as the number of sensors increases. Moreover, it is required to drive each sensor at different temperatures. Because temperatures are determined by the power consumption in a self-heating sensor, it is necessary to generate various voltages that are applied to each sensor. However, since sensor resistance depends on its temperature, the sensor resistance must be monitored for a feedback loop to heat up to target power consumption. Creating the various independent bias voltages which follow the sensor resistances makes overall circuit scale large. Besides, since the bias voltage is 5-15V, an up-converter are required for each sensor to generate the voltages from 3.3 V supply voltage. An array of the up-converters increases power-consumption and size of the whole system. To create the reasonable sensory system, pulse-heating operation is adopted. The 16 self-heated sensors are mounted and biased by a single DC-DC converter. One sensor is selected at each heating time. During the heating time, a voltage converter is enabled, and the flowing current through a sensor is monitored to keep constant power. In addition, a PID controller is developed to follow changing resistance. After the sensors are heated for a short time, a readout circuit is enabled. The thermal control circuit is disabled to reduce power consumption and decrease noise power during the reading operation. In the following sections, a heating method and a readout method are explained in detail.

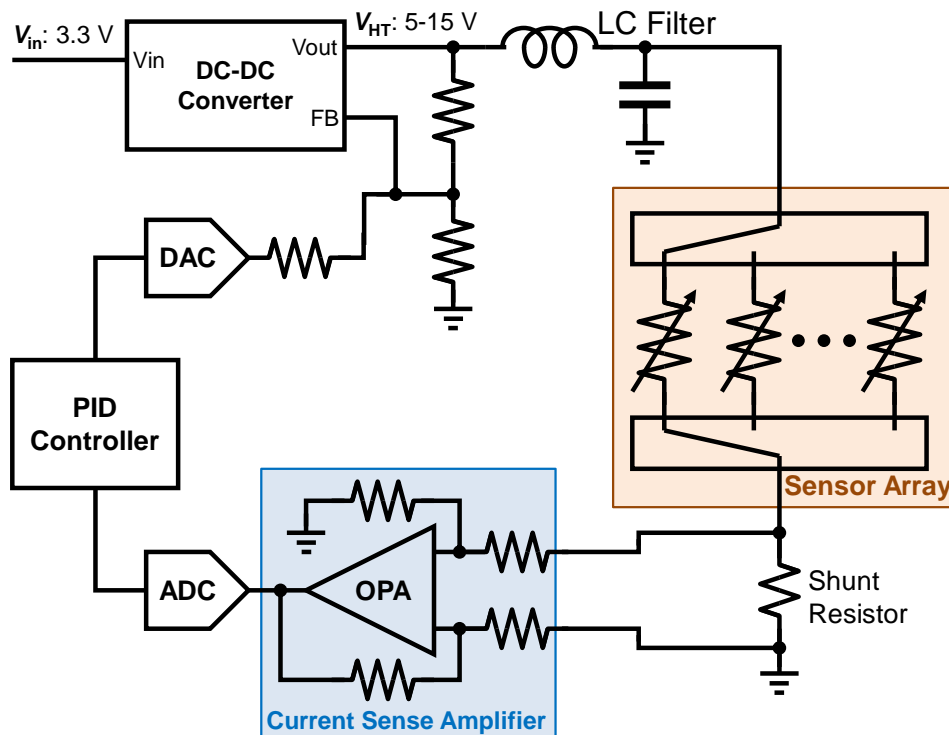


Figure 5.1 Thermal control circuit.

5.1.1 Thermal Control Circuit

It has been known that the resistance range of the metal-oxide sensors is around between 5-50 k Ω . To increase temperature up to 100 $^{\circ}\text{C}$, 5-6 mW power is required for self-heating. From the given information on the resistance and the power, the range of bias voltage of the sensor is determined as 5-15 V. Since the system input voltage is 3.3 V, a DC-DC converter is installed. To control the output voltage of the DC-DC converter while monitoring the sensor's current, DAC is placed with an output resistor before the feedback input of the DC-DC converter. A shunt resistor is inserted between a sensor and the ground to measure a flowing current through the sensor. The voltage through the shunt resistor is measured by ADC after it is gained by a current sense amplifier. The thermal control circuit is shown in Figure 5.1. One sensor is selected by multiplexers and the others are disconnected at a heat timing. Bias voltage V_{HT} is calculated from a DAC value. Therefore, consumed power at a selected sensor is calculated from

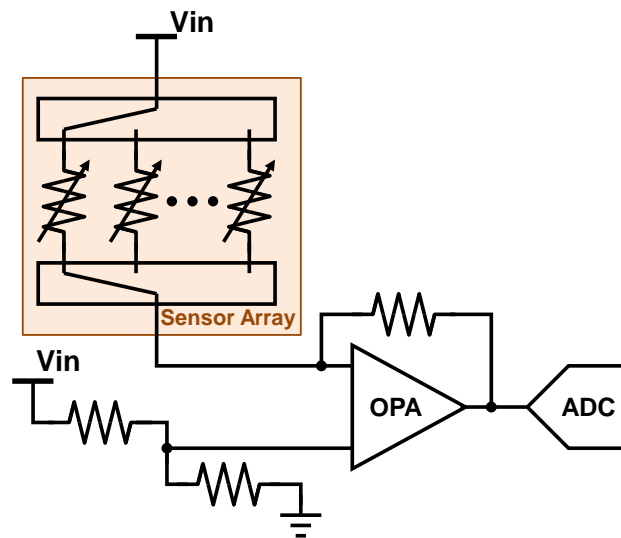


Figure 5.2 Readout circuit.

V_{HT} and current measured by the ADC. Because the resistance of a self-heating sensor depends on its temperature, a PID controller is required to follow resistance change and reach target power. In practice, switching noise from a DC-DC converter is large because the sensor resistance is high. Thus, a low-pass filter is placed before a sensor array to decrease the noise. The frequency of the switching noise is high, and it is practically difficult to eliminate the noise using an RC filter with putting an output capacitor. Thereby, an LC filter is selected as a low-pass filter.

5.1.2 Readout Circuit

To read sensor resistance with 0.1 % order of error, a readout circuit is also implemented. It is true that the thermal control circuit can read sensor resistance by bias voltage and sensor current, which are observed by DAC and ADC. However, the estimated value of output voltage is not accurate because it depends on the offset voltage of feedback of a DC-DC converter, mismatch of feedback resistors, and resolution of DAC. Besides, generating voltage through a DC-DC converter requires extra power consumption. Therefore, a separate readout circuit is required.

In Figure 5.2, a designed readout circuit is shown. An op-amp is used for a trans-impedance amplifier. The sensor resistance can be changed during readout because reading bias voltage can cause self-heating. The bias voltage is generated by a voltage divider circuit and the voltage is adjusted. The input-offset voltage of the op-amp affects the bias voltage of the sensor and readout accuracy. However, the absolute value of bias voltage is not required to be accurate compared to the relative value. In addition, a readout error derived from the input offset can be calibrated easily. On the contrary, it is effective to suppress 1/f noise by an op-amp to improve sensitivity for molecules because the sensors suffer from drift effects to the extent that it hides gas response.

5.1.3 Overall Circuit Design

To make the overall circuit, a difference in the operating voltages should be considered carefully. The thermal control circuit (5.1.1) uses up to 15 V, while the readout circuit (5.1.2) is operated at 3.3 V. Therefore, high-voltage-tolerant switches must be used. Four states of a sensor are configured in a whole measurement flow as shown in Table 5.1. In idle operation, no current flows into the sensors. There are several ways to operate the sensors in the idle state. Regarding a high side of a sensor, it can be connected to three nodes: V_{HT} , V_{in} , and GND. As for the low side of the sensor, it is connected to a shunt resistor when the sensor is heated, or connected to a trans-impedance amplifier (TIA) when the sensor is read. Otherwise, it is disconnected for the idle operation.

Table 5.1 Possible sensor states in measurement operation.

State	Idle A	Idle B	Heat	Read
High side	GND	V_{in}	V_{HT}	V_{in}
Low side	don't care	float	shunt resistor	TIA

Therefore, high-voltage tolerant, 3PST analog switches are selected for high-side switches. As low-side switches, a 16:1 multiplexer (MUX) is used.

The overall circuit was designed with the above consideration. The schematic and selected IC part numbers are shown in Figure 5.3. High side switch, ADG1439 is driven by V_{HT} , and other components are driven by V_{in} . As a feedback DAC, 10-bit DAC is selected. V_{HT} is determined by a DAC value as follows:

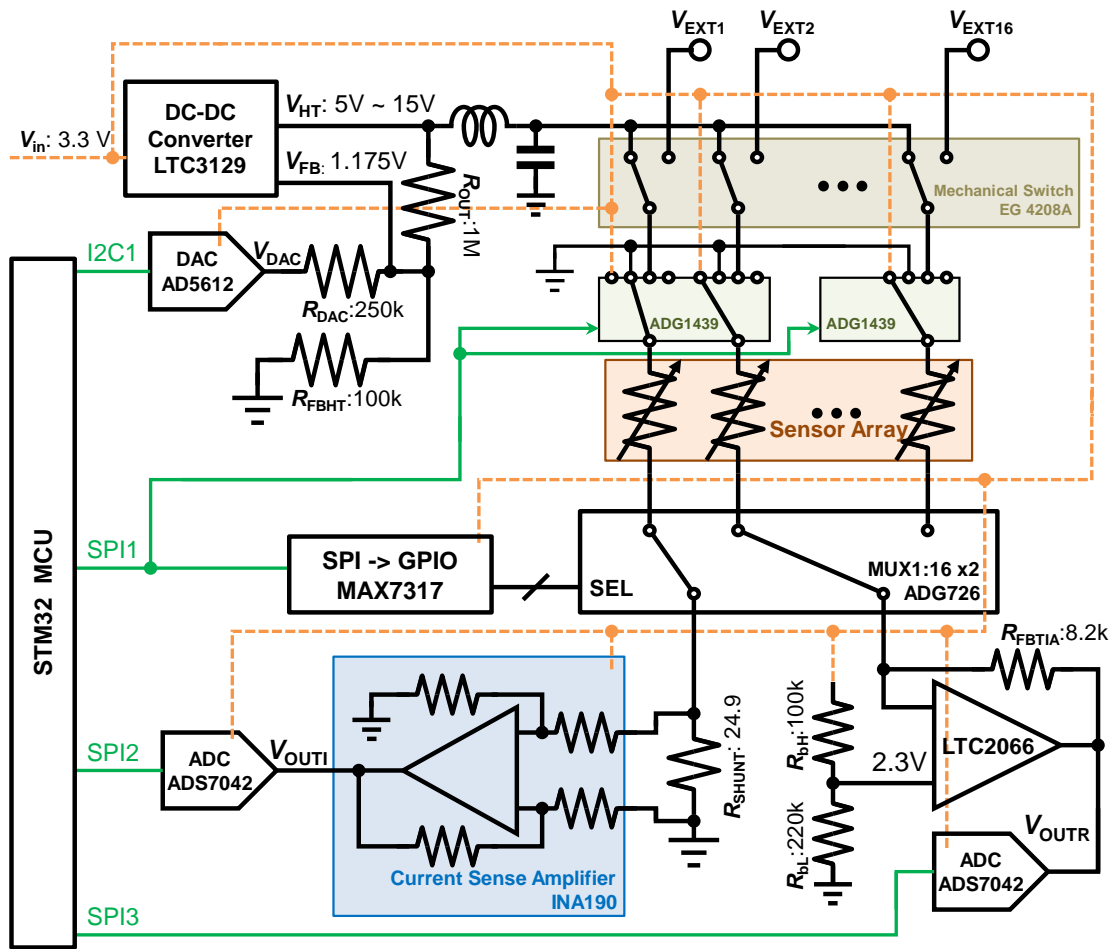


Figure 5.3 Overall circuit design for a constant-power and pulse-measurement system.

$$V_{\text{DAC}} = V_{\text{in}} \cdot \frac{D_{\text{DAC}}}{2^{10} - 1} \quad (5.1)$$

$$V_{\text{HT}} = R_{\text{OUT}} \cdot \left(\frac{V_{\text{FB}}}{R_{\text{FBHT}}} - \frac{V_{\text{DAC}} - V_{\text{FB}}}{R_{\text{DAC}}} \right) + V_{\text{FB}} \quad (5.2)$$

where D_{DAC} denotes a digital value of DAC. R_{OUT} , R_{DAC} , and R_{FBHT} are set to 1 M Ω , 250 k Ω , and 100 k Ω , respectively. Thus, the resolution of V_{HT} which is controlled by DAC is

$$V_{\text{HTLSB}} = 13 \text{ mV} \quad (5.3)$$

As ADCs of heat current sensing and resistance readout, 12-bit ADC is selected. A shunt resistor R_{SHUNT} is 24.9 and the gain of a current sense amplifier is 50 (INA190A2). Heat current, I_{heat} , is calculated as follows:

$$I_{\text{heat}} = \frac{V_{\text{OUTI}}}{A_{\text{INA190}} \cdot R_{\text{SHUNT}}} \quad (5.4)$$

where A_{INA190} expresses the gain of the current sense amplifier. Thus, the resolution of the heat current is expressed as follows:

$$I_{\text{heatLSB}} = 647 \text{ nA} \quad (5.5)$$

For the trans-impedance amplifier in the readout circuit, a zero-drift amplifier, LTC2066 is selected. The sensor resistance is calculated as follows:

$$R_{\text{sensor}} = \frac{R_{\text{FBTIA}}}{1 - \frac{V_{\text{OUTR}}}{V_{\text{in}}} \cdot \frac{R_{\text{bL}}}{R_{\text{bH}}}} - R_{\text{SW}} \quad (5.6)$$

$$V_{\text{OUTR}} = V_{\text{in}} \cdot \frac{D_{\text{ADCR}}}{2^{12} - 1} \quad (5.7)$$

where R_{SW} denotes total parasitic resistance, which is in analog switches and metal wires, and D_{ADCR} expresses a digital value of ADC in the readout circuit.

The mechanical switch, EG 4208A, is not related to the pulse measurement system. However, it was used to input external voltage or measure the current through a sensor resistance. During pulse heating measurement, all poles are connected to the DC-DC converter. The circuit is developed with KiCAD. The schematic is shown in Figure 5.4.

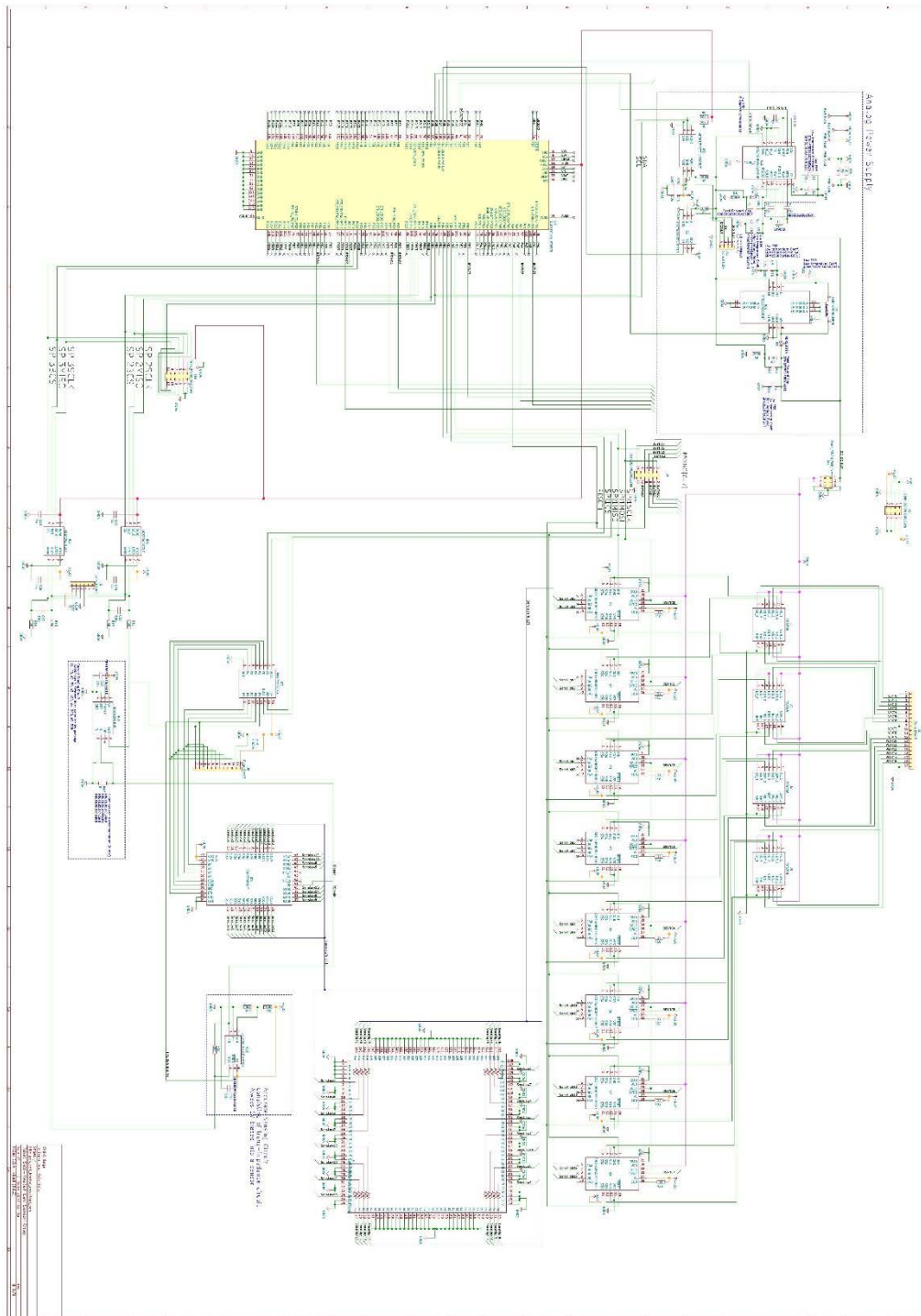


Figure 5.4 Schematic of constant-power and pulse-measurement system.

5.2 Operation Flow

To obtain molecule information under various temperature conditions, every sensor is set to a different target power. However, making various voltages independently increases the size and power consumption of the interface circuit because independent DC-DC converters are required. Therefore, analog switches are inserted between a DC-DC converter and heated sensors. One sensor is selected and heated by the switches, and other sensors are kept idle. After the sensor is heated, the resistances of the other sensors are read by the readout circuit. While the readout circuit is enabled, the heating stops to avoid the 15 V line from inducing large noises into the readout circuit. A graph of the operation sequences is shown in Figure 5.5. A heated sensor is switched in order, and resistance is read with around 1 V of bias voltage in intervals of heating. During heating, constant power is put into a sensor. It is possible to calculate sensor resistance from the ADC and the DAC values. However, the bias voltage that is determined by DAC is inaccurate compared to the readout circuit. Particularly, a DC-DC converter consumes much larger power than the readout circuit. Thus, it is inappropriate to use the heating circuit to read resistance.

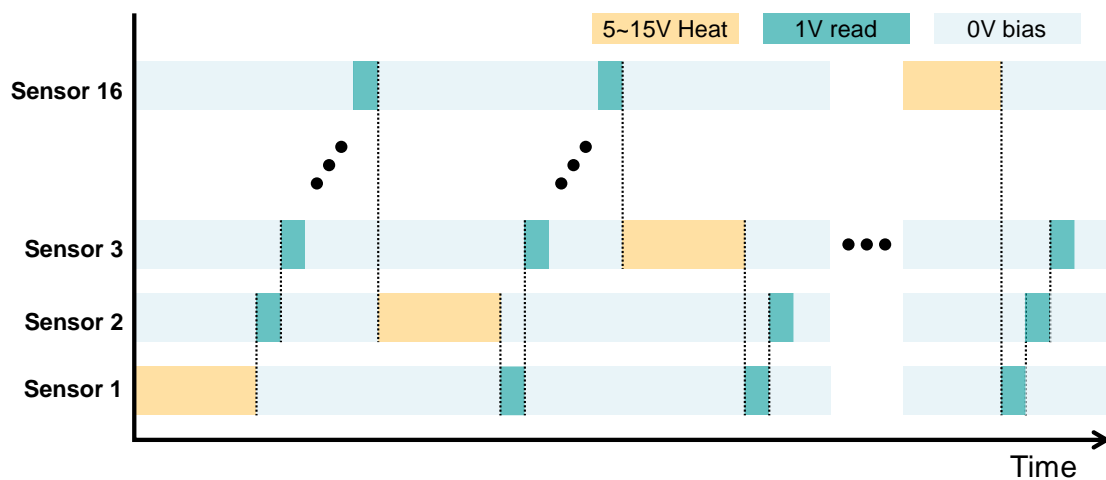


Figure 5.5 Operation sequence.

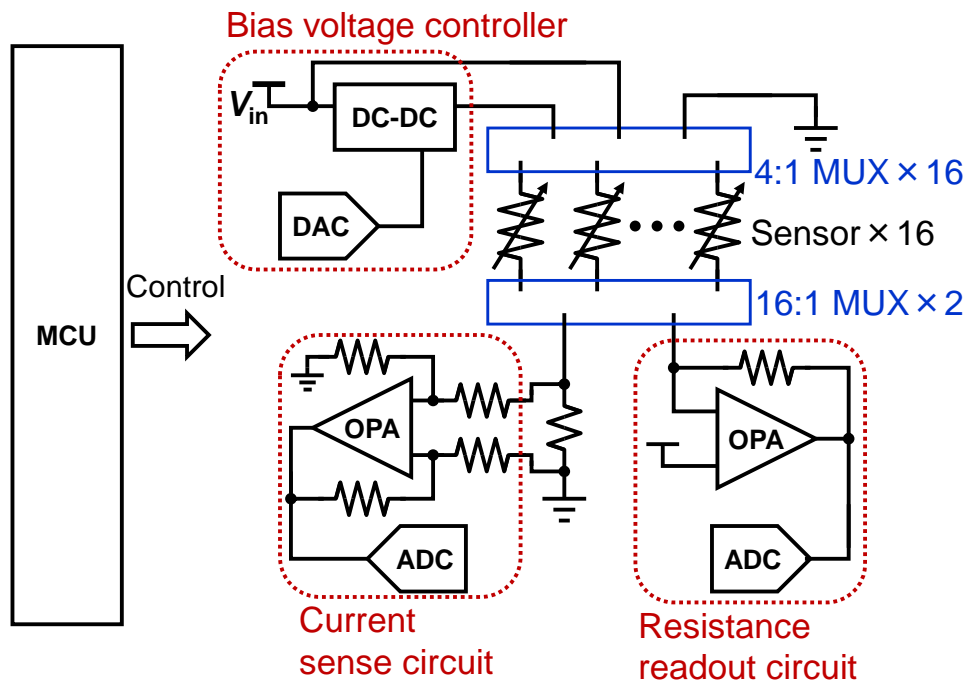


Figure 5.6 Functional block.

Based on the operation flow in Figure 5.5, each functional block is turned on and turned off to optimize the system's power consumption. In Figure 5.6, an outline drawing of the schematic is shown. MCU controls all the ICs, and the power consumption can be saved by disabling ICs. It should be noted that adequate start-up operation is required before entering the heat-and-read sequences. When V_{in} is inputted and MCU wakes up, all the functional ICs turn off. The power consumption is the lowest. This state of the circuit is named "idle state" as shown in Figure 5.7. In the experiment, V_{in} was always 3.3 V.

After the idle state, the operation moves to "first readout". During the first readout operation, all the initial sensor resistances are measured. In this operation, the upper side of each sensor is connected to V_{in} and the other side is connected to the readout circuit. The readout circuit and the analog switches are enabled. The result of the first readout is used for choosing which target power is applied for a sensor. A low-resistance sensor requires a lower voltage than a high-resistance sensor when it comes to applying the same power. Thus, the array of

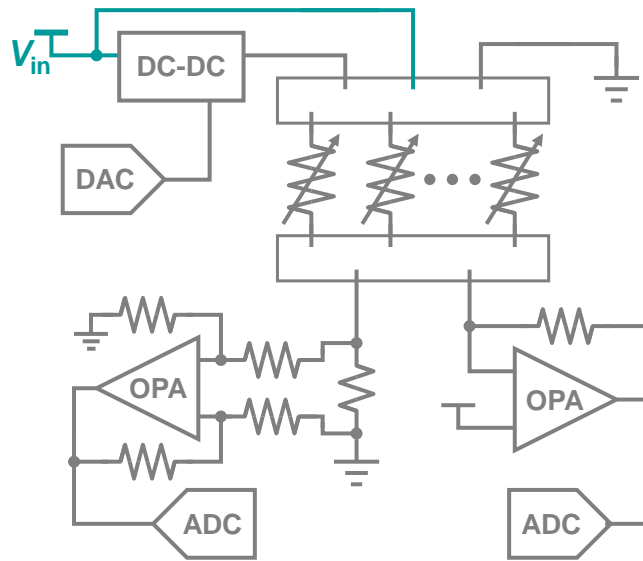


Figure 5.7 Idle state, which is right after the V_{in} is inputted.

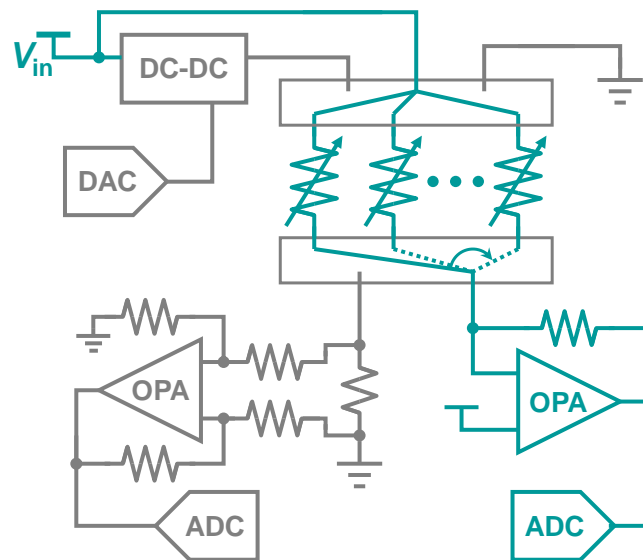


Figure 5.8 Circuit for the first readout operation.

the target powers defined by a user is rearranged to an order of resistance values. This operation is shown in Figure 5.9 by a specific example.

Then, the heating operation starts as shown in Figure 5.5. The circuit is configured with three patterns: “PMIC wake-up”, “Readout operation”, and “Readout operation”. These configuration loops after starting “PMIC wake-up”. In “PMIC wake-up” the operation flow is as follows (Figure 5.10):

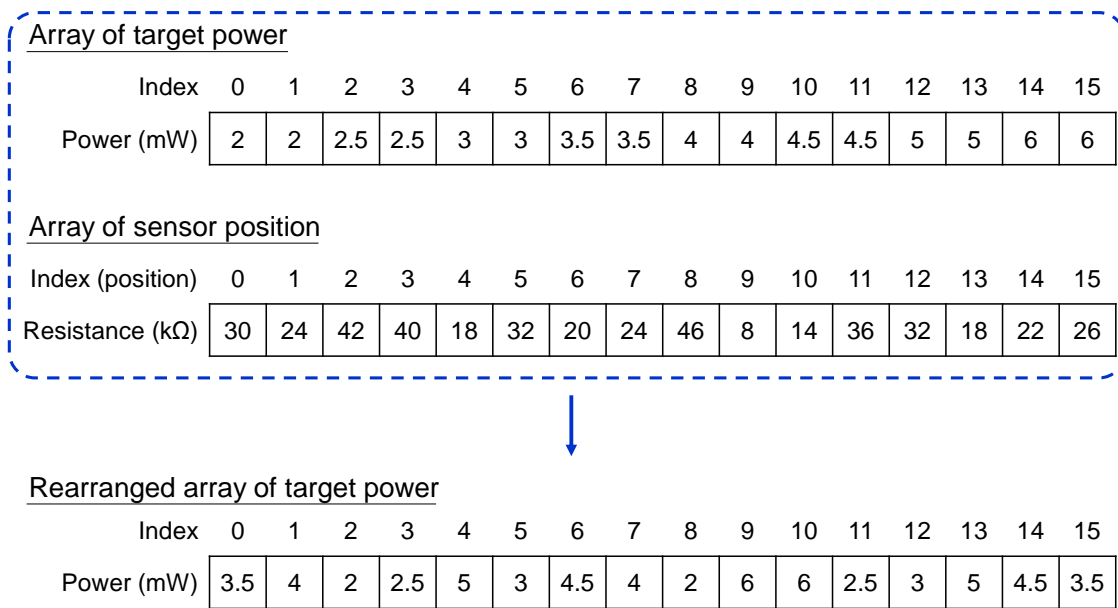


Figure 5.9 Example of power rearrangement.

- ① All the sensors are connected to ground to prevent high voltage generated from the DC-DC converter from causing crosstalk to readout circuits.
- ② The readout circuit is disabled.
- ③ The DC-DC converter and DAC are turned on.

After the DC-DC converter wakes up, selected sensor is heated with the following operations (Figure 5.11):

- ④ 16:1 MUX connects a current sense circuit with a heated sensor. The other pole of 16:1 MUX is connected to another sensor.
- ⑤ 4PST switches connect the DC-DC converter with the heated sensor. The other sensors are connected to V_{in} .
- ⑥ Switch configurations ④ and ⑤ are done, the current sense amplifier is turned on and MCU starts a PID control via the ADC and DAC values.

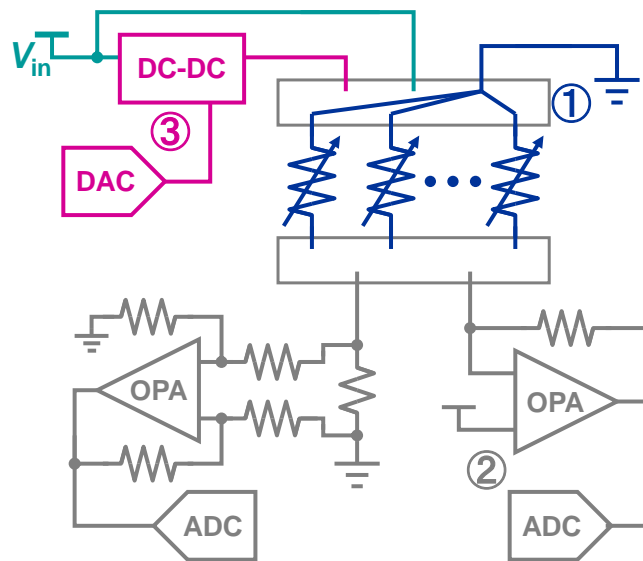


Figure 5.10 PMIC wake-up.

It should be noted that switching timing of analog switches is carefully configured because high voltage may break low-voltage ICs. In the experiment, the heating time was around 100 msec. After heating time passed, the DC-DC converter is disabled, and the resistance readout operation begins. The readout operation is carried out as the following operations (Figure 5.12):

- ⑦ The DC-DC converter and DAC are disabled.
- ⑧ The current sense amplifier is disabled.
- ⑨ The trans-impedance amplifier is enabled.
- ⑩ 1:16 MUX connects a non-heated sensor with the readout circuit. Non-heated sensors are selected one by one after measuring output voltage with ADC.

After the readout operation finishes, the operation is back to the “PMIC wake-up” configuration.

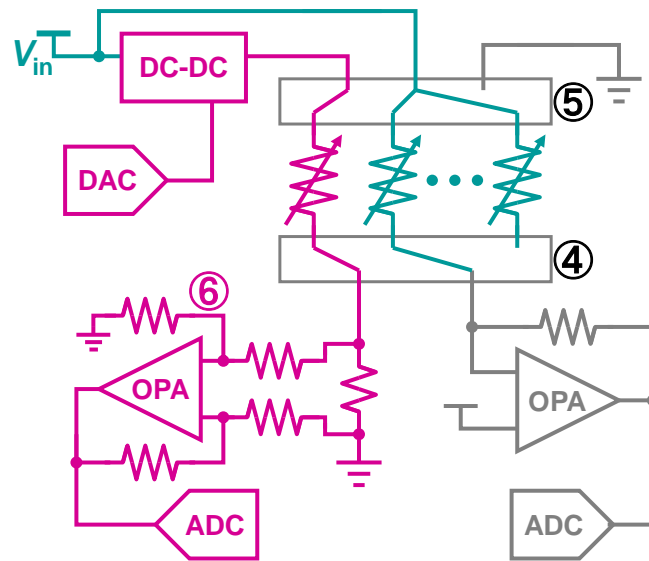


Figure 5.11 Heating operation.

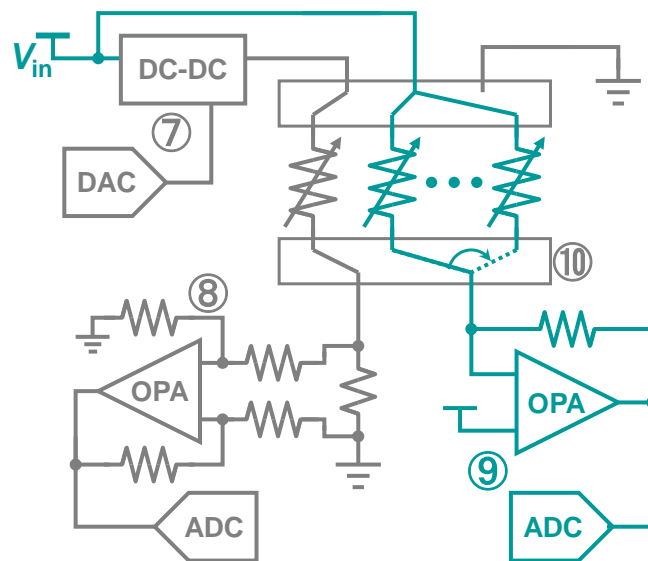


Figure 5.12 Readout operation.

5.3 Measurements

To verify that input power into a target sensor is exact and accuracy of reading resistance is high enough, it is necessary to evaluate the circuit performance. Important items of evaluation are the accuracy of the readout circuit, the estimation of the power consumption of the sensors, the operation of the PID controller, the noise of the DC-DC converter, and power consumption under each operating configuration. In the measurements, fixed resistors are used as dummy sensors. Since its resistance is unchanged, DC characteristics are evaluated.

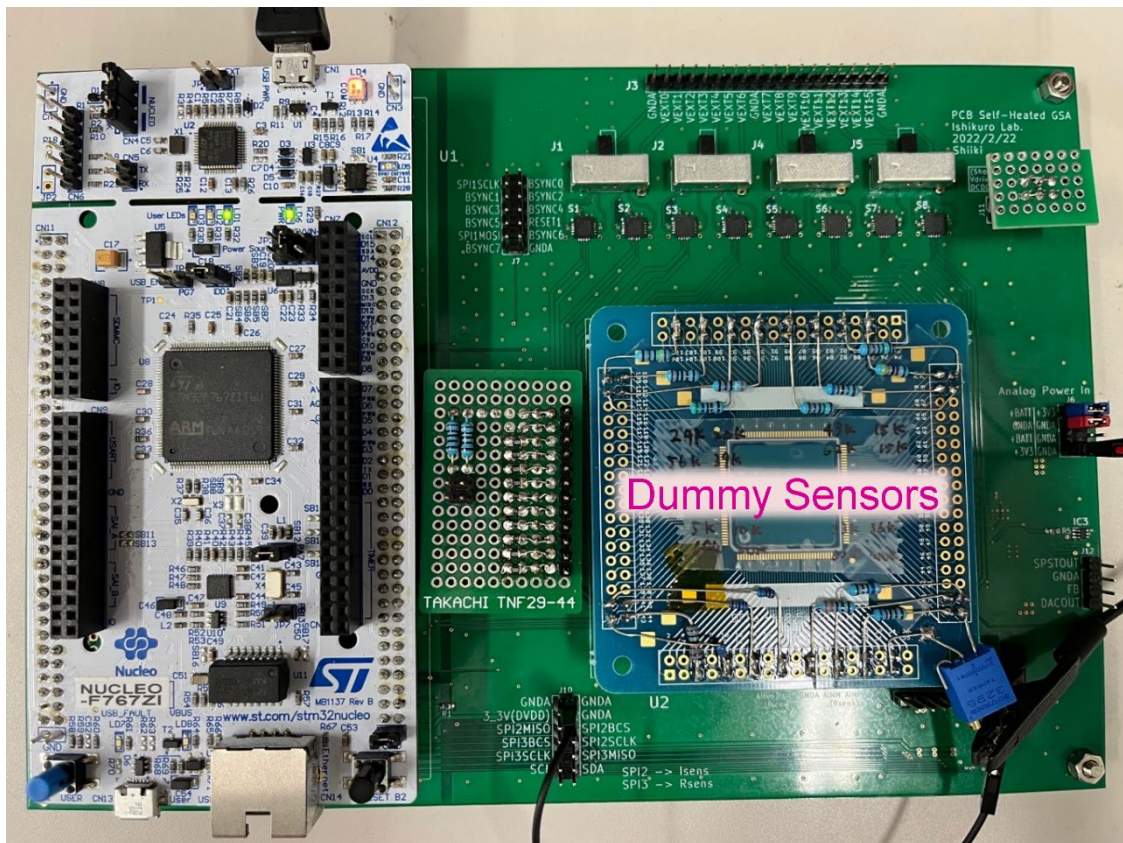


Figure 5.13 PCB of constant-power and pulse-measurement system with dummy sensors mounted.

Index (position)	0	1	2	3	4	5	6	7
Resistance (k Ω)	67.9	20.0	5.09	9.97	56.2	38.9	24.0	20.0
Index (position)	8	9	10	11	12	13	14	15
Resistance (k Ω)	42.8	15.0	61.6	15.0	33.2	36.0	61.7	5.27

Figure 5.14 dummy sensor's resistances and their positions.

5.3.1 Developed PCB

An implemented PCB is shown in Figure 5.13. Its size is 21 cm \times 14.5 cm. Nucleo-F767ZI is used for the MCU, and it controls measurement operations. As dummy sensors, 15 fixed resistors and 1 variable resistor is implemented. The resistance values are selected randomly to meet the condition that they are between 5 k Ω to 70 k Ω . The resistances are checked with a digital multimeter, PC7000, Sanwa. The results are shown in Figure 5.14. The analog power-supply V_{in} was 3.3 V, which is generated by E3631A, Keysight. During all measurements and experiments, MCU is connected to a PC with a USB cable and a power supply for the digital circuits: 3.3 V was generated on the MCU board.

5.3.2 Readout Accuracy

DC characteristic of ADC is firstly measured. In the readout circuit, ADC is used with a trans-impedance amplifier. Therefore, ADC resolution is checked by creating a histogram. Using dummy resistance values, around 8,000 plots of ADC outputs for each dummy resistor are gathered. As the representative histograms, the 3rd and 6th resistors' histograms are shown in Figure 5.15.

To evaluate the readout accuracy, the obtained values of ADCR are averaged. Around 8,000 data are collected for each resistor, and 16 dummy resistors are

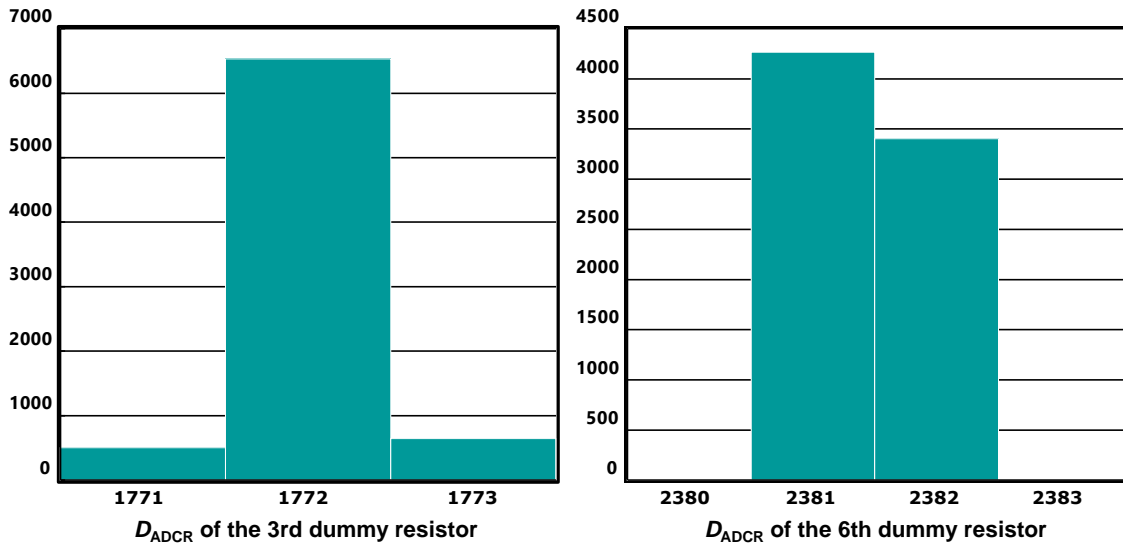


Figure 5.15 Histograms of output values of ADC in the readout circuit.

measured in one measurement. Resistance is calculated based on Equations 5.6 and 5.7. However, the true values of R_{FBTIA} , R_{bL} , and R_{bH} are unknown. In addition, switch resistance R_{SW} is relatively unreliable from a data sheet. Therefore, those parameters are estimated by optimization, and typical values are used as initial value conditions. For the optimization, Equations 5.6 and 5.7 are used to express resistance value and the following evaluation function is minimized:

$$\left| \frac{R_{\text{Measured}} - R_{\text{True}}}{R_{\text{True}}} \right| \quad (5.8)$$

Table 5.2 Initial parameters used for resistance calculation.

Variables	R_{FBTIA}	R_{bL}	R_{bH}	R_{SW}
Values	8.2 k Ω	220 k Ω	100 k Ω	0 Ω

Table 5.3 Fitted parameters for resistance calculation.

Variables	R_{FBTIA}	R_{bL}	R_{bH}	R_{SW}
Values	8.1850 k Ω	220.08 k Ω	99.920 k Ω	47.553 Ω

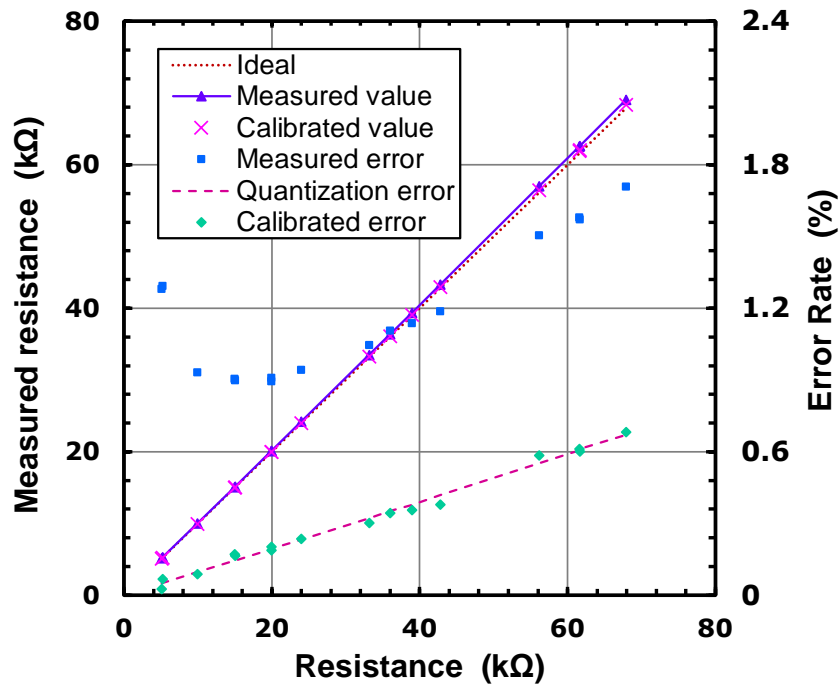


Figure 5.16 Error evaluation in the readout circuit.

where, R_{Measured} is the calculated results with estimated parameters and R_{True} is the measured value with a digital multimeter shown in Figure 5.14. By executing optimization, the fitted parameters are obtained. The initial value and the fitted parameters are shown in Table 5.2 and Table 5.3.

With the fitted parameters, the readout performance shown in Figure 5.16 is obtained. The vertical axis on the left expresses resistance and the vertical axis on the right expresses its error rate in %. The “Ideal” line and “Quantization error” dot line show the true resistance value and theoretically minimum error rate determined by 12-bit ADC resolution. “Measured value” and “Measured error” show resistance calculated by the initial parameters in Table 5.2 and its readout error. It is shown that the error rate increased in the high-resistance region between 20-70 k Ω because of quantization error. On the contrary, in the low-resistance region, the error rate increased rapidly. This is caused by the switch resistance offset. “Calibrated value” and “Calibrated error” show the resistance value calculated with the fitted parameters and its readout error. Compared with

the “Quantization error” dot line, the readout error apparently decreases to the theoretically minimum value. Besides, from the fitted parameters shown in Table 5.3, the fitted values are within 1 % of their typical values. The switch resistance also has a possible value based on the analog switches [113], [114]. Therefore, it was concluded that the optimization was successfully applied and the expected performance was acquired.

5.3.3 Input Power Accuracy

The input power accuracy is determined by the current sensing accuracy and the output accuracy of the DC-DC converter controlled by DAC. Since it would take excess time and effort to measure the input power directly, the performances of the current readout and DC-DC converter are evaluated separately. Although required performances depend on the temperature-circuit parameters of a sensor, the input of 1 mW corresponds to an increase of 10 K about the developed sensor.

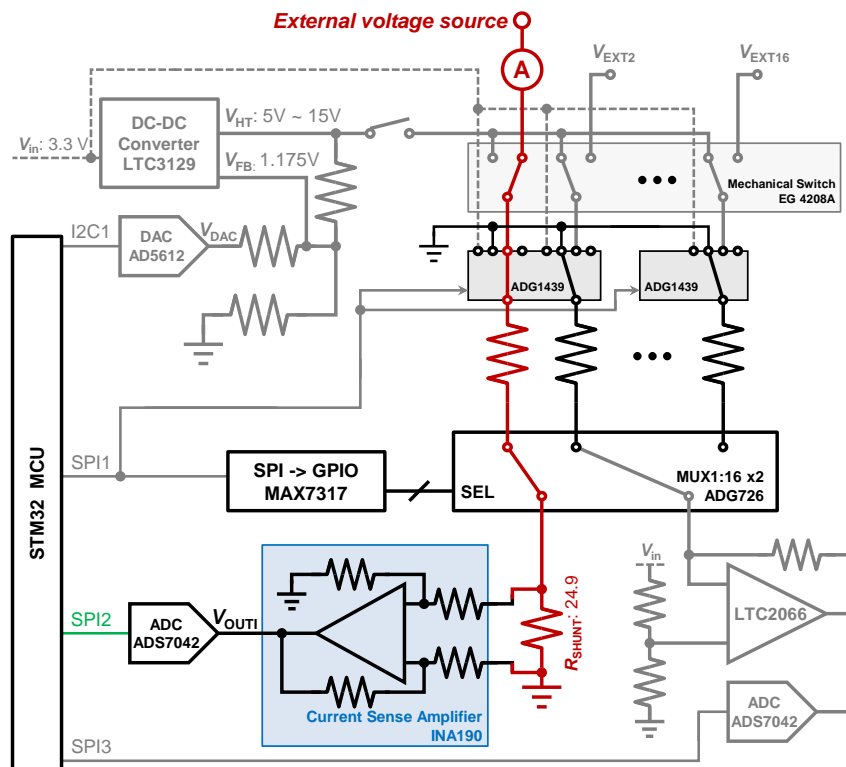


Figure 5.17 Circuit configuration to evaluate current sensing.

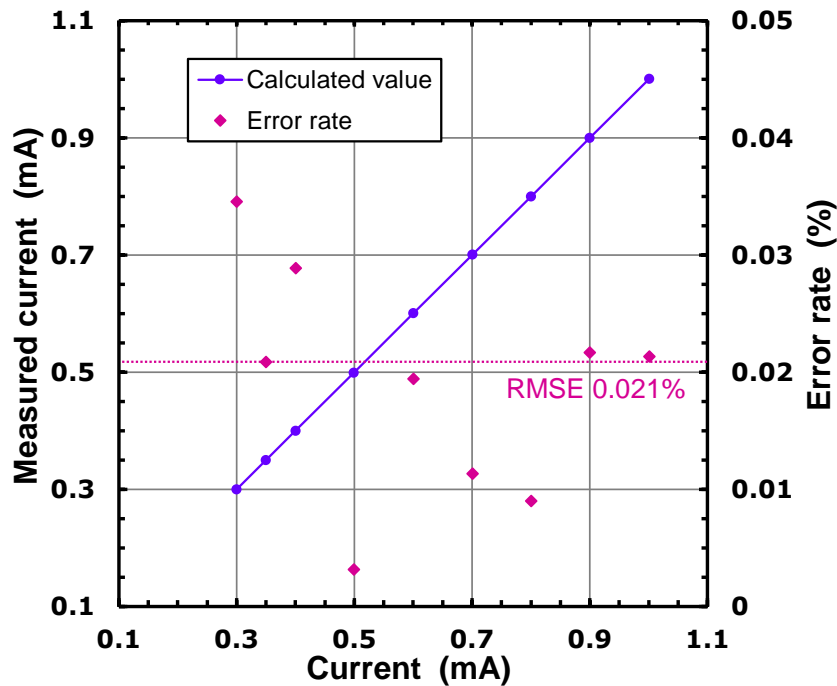


Figure 5.18 Current sensing accuracy.

In addition, it was reported that sensor temperature dependence appears in a 10 K difference [97]. Therefore, we aimed for an input-power resolution of 0.1 mW to control a 1 K difference.

To evaluate current sensing accuracy, a dedicated configuration is built as shown in Figure 5.17. To one pole of the mechanical switch, an ammeter and external voltage source is connected in series. In the figure, the flowing current through the 1st sensor is measured. 1:16 MUX connects the 1st sensor with the shunt resistor. Other dummy resistors connect to GND with the 4PST switches. As an ammeter, a digital multimeter, 34401A Keysight Technologies [115], was used. The output voltage of the current sense amplifier is measured by ADC. Since the same ADCs are used between the current sensing circuit and the readout circuit, the DC characteristics of ADC are the same as shown in Figure 5.15. Under this condition, the amount of current is measured between 0.3 mA and 1 mA with a 0.1 mA step. It should be noted that the resolution of the digital multimeter becomes worse than the current sense amplifier over a 1 mA range. A

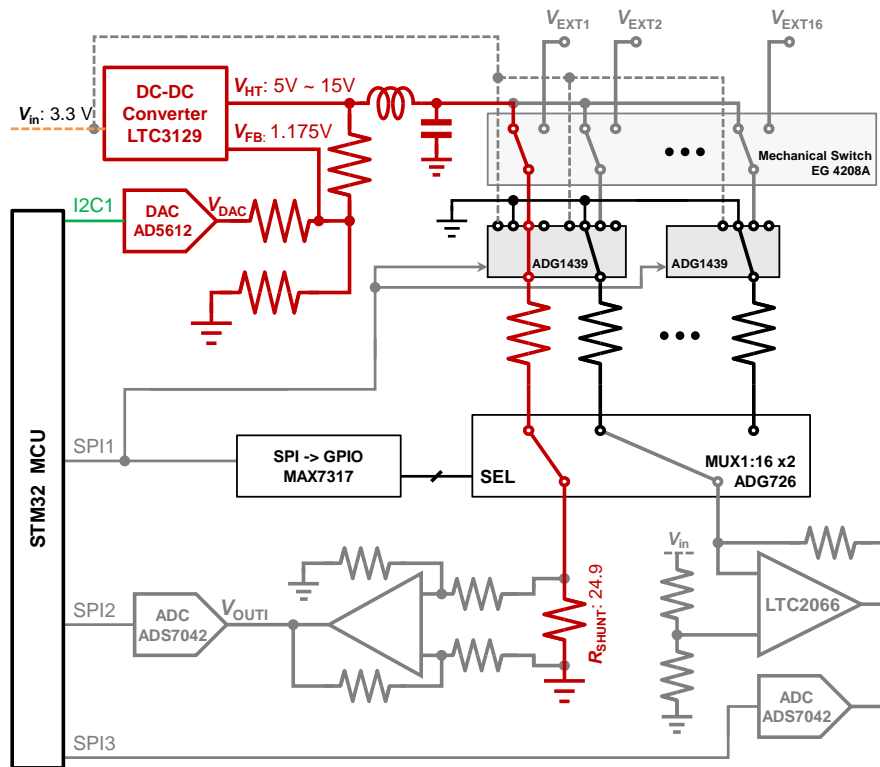


Figure 5.19 Circuit configuration to evaluate specification of controlling output voltage.

graph of result plots is shown in Figure 5.18. Each plot is calculated with Equation 5.4 after obtaining 8,196 ADC data and averaging them. The horizontal axis expresses the current that is measured by the ammeter. The vertical axis on the left expresses current measured by the current sensing circuit, and the vertical axis on the right expresses its error rate in %. According to the graph, RMSE is 0.021 %, which is accurate enough to achieve power control with 0.1 mW resolution.

Secondly, the accuracy to control DC-DC output by DAC was evaluated. The DC-DC converter and DAC are turned on and the 12th resistance, 33.2 k Ω , is selected as a load resistance. Analog switches are configured to connect the resistance with the DC-DC converter and the shunt resistor, while other dummy resistors are connected to GND. Other functional blocks: the current sense amplifier and the resistance readout circuit are turned off. This configuration is

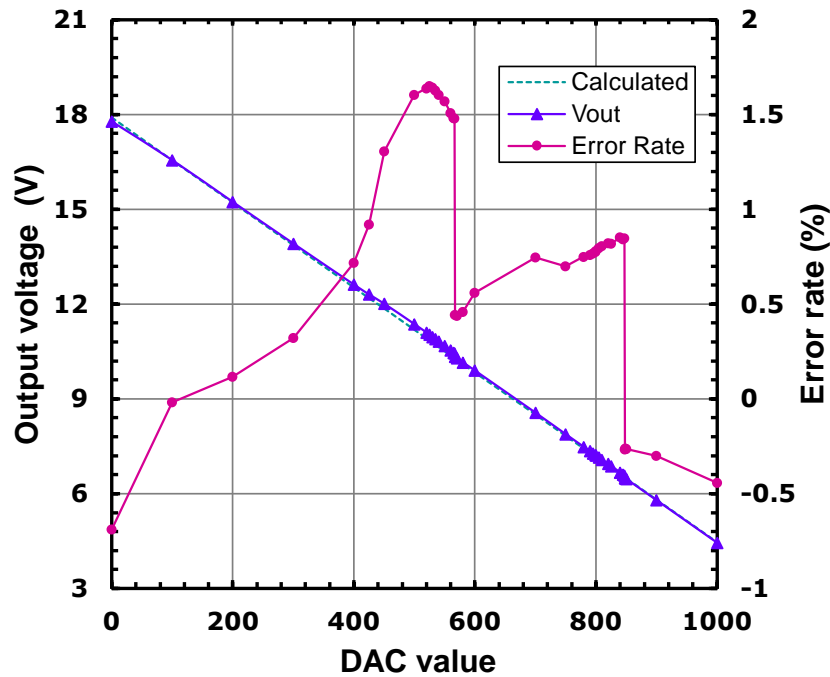
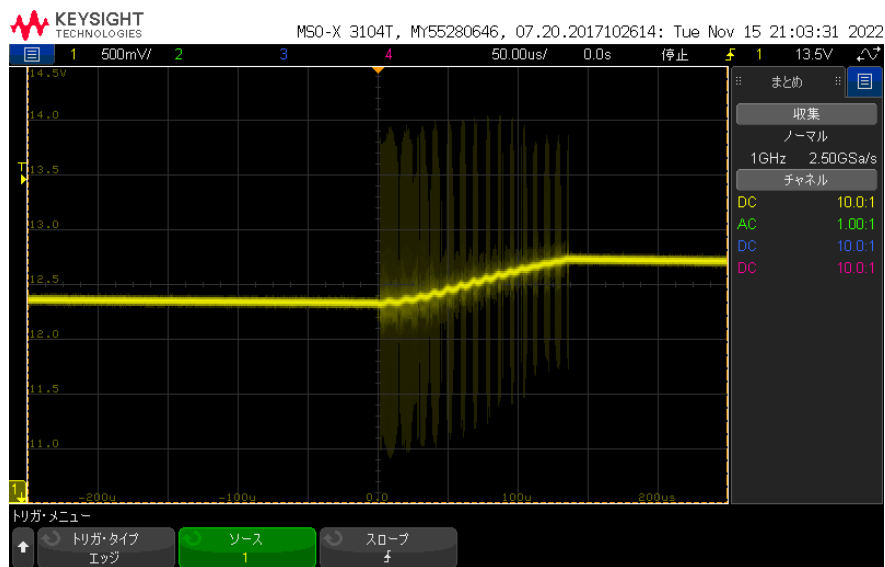


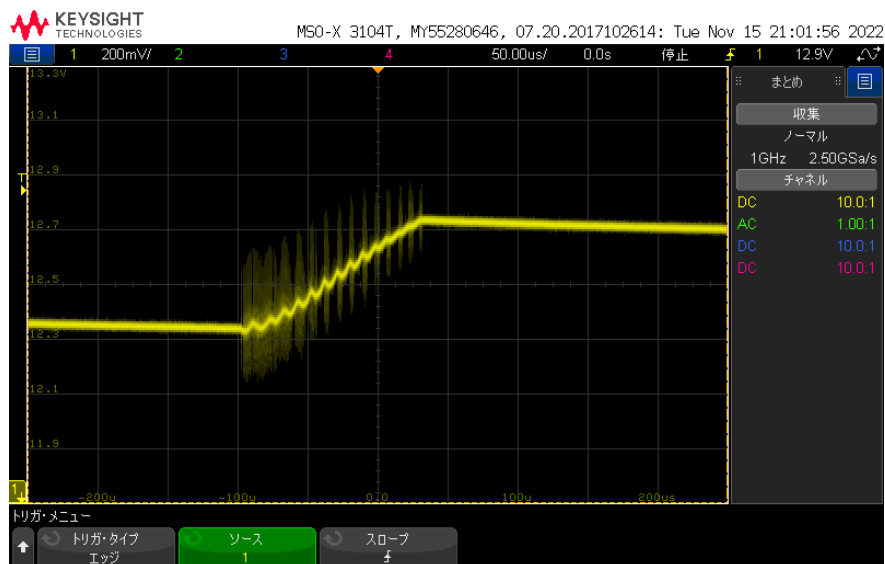
Figure 5.20 Accuracy of output voltage of a DC-DC converter configured by DAC.

shown in Figure 5.19. The DAC is configured from 0 to 1,000 and a step was variable. Output voltage V_{HT} is measured by the digital multimeter 34410A Keysight Technologies [115]. The measurement results are shown in Figure 5.20. The horizontal axis expresses configured DAC value and the vertical axis expresses the voltage of a DC-DC converter. The “ V_{out} ” line expresses the measured value. The “Calculated” dot line expresses the expected output voltage, which is calculated from a DAC value with Equations 5.1 and 5.2. The “Error Rate” line shows the relative error of the measured V_{out} and calculated V_{out} . According to the graph, the DC-DC output voltage can swing in the range of around 4-18 V with at most a 1.7% of error rate. However, the upper limit of the output voltage is 15 V from the datasheet of LTC3129 [116].

From the results shown in Figure 5.18 and Figure 5.20, it is concluded that the power consumption through a sensor can be calculated from the DAC and the ADC value with at most 1.7%. In this study, the input powers for the sensors are



(a)



(b)

Figure 5.21 Noise level of DC-DC output and LC filter output.

controlled between 3-6 mW. Within this range, the power can be set with 0.05-0.1 mW absolute error. Therefore, the heating circuit satisfies the required accuracy.

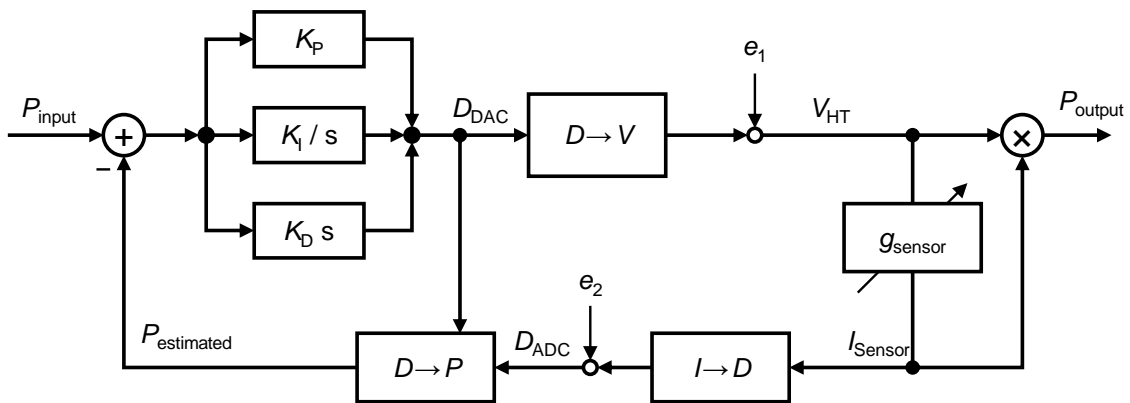


Figure 5.22 Block design of PID controller.

5.3.4 LC Filter

The noise level of a DC-DC converter was around $\pm 2\text{V}$ and the amplitude is determined by ESR of the output capacitor for the DC-DC converter. To decrease the noise level, an LC filter is inserted in front of the sensor array. The inductance value is 13 nH and the capacitance is 390 pF. To confirm that the noise decreases by a low-pass filter, the output voltage of the DC-DC converter and voltage behind the low-pass filter were monitored by an oscilloscope. Their screenshots are shown in Figure 5.21. As we can see, the noise level decreases to the extent that the amplitude is $\pm 200\text{ mV}$.

5.3.5 PID Control

In Section 5.3.3, we discussed the accuracy of input power monitoring. However, the sensor resistance depends on its temperature and the biasing voltage should follow the resistance change. To adjust the resistance change, PID control is adopted in this system. A system block design of the controller is shown in Figure 5.22. In the design, P_{input} expresses target power consumption and P_{output} expresses power consumption that is applied to a selected sensor. $P_{\text{estimated}}$ is the calculated power by ADC and DAC. Thus, the PID controller operates to eliminate the difference between P_{input} and $P_{\text{estimated}}$. The controlled object is

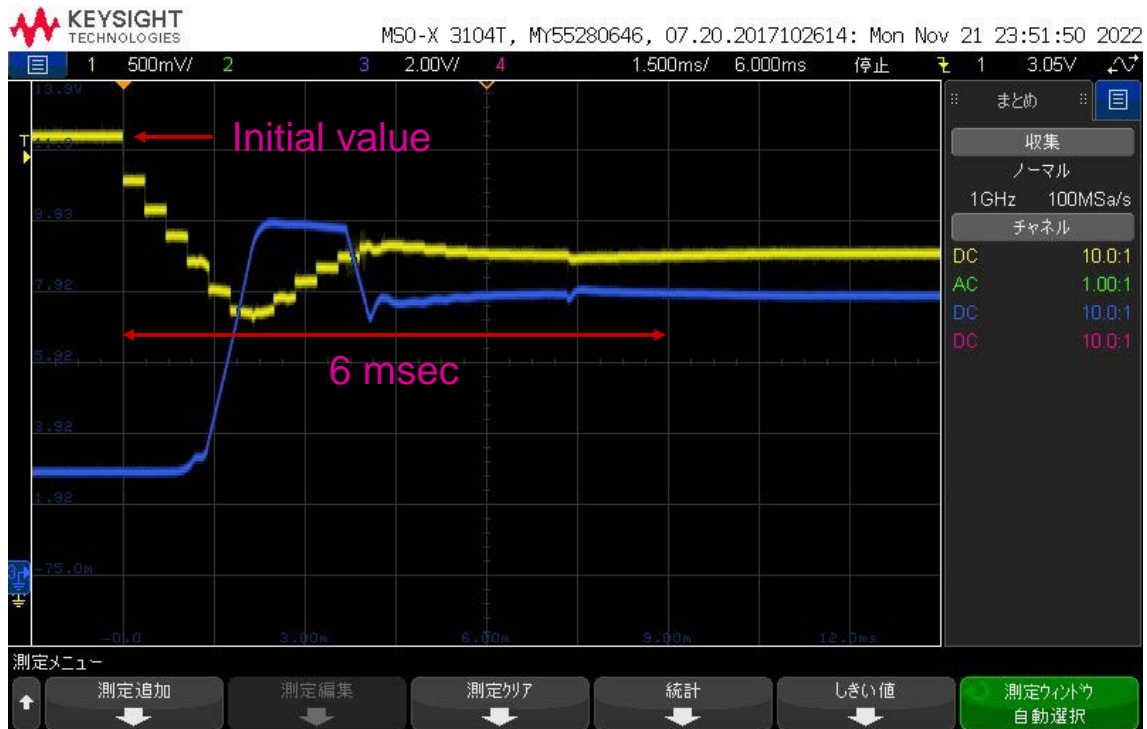


Figure 5.23 PID controller operation

expressed as the conductance of the sensor, g_{sensor} and it is expressed variable parameter. Error that is caused by calculating physical quantity from a digital value of ADC or DAC is expressed as e_1 and e_2 , which value is already discussed in Section 5.3.3. From the error rate, P_{output} can be predicted from $P_{\text{estimated}}$ with a 1.7 % error. The PID parameters, K_P , K_I , and K_D are optimized manually. At last, the optimized PID controller is programmed in MCU and its operation is monitored by an oscilloscope as shown in Figure 5.23. The yellow line is the voltage at the DAC output node, and the blue line is the voltage at the output of the DC-DC converter. As the load resistance, the 12th position's resistor was selected. As shown in the figure, it takes 6 msec to reach its stable state.

5.3.6 Power Consumption

While the metal-oxide sensors consume 3-10 mW to increase operating temperature, overall power consumption should be suppressed to the extent that the power of the interface circuit keeps as low energy as the sensor. The circuit

IC that uses the largest power is a DC-DC converter. It loses excessive power to increase a voltage from 3.3 V to up to 15 V. In particular when sensor resistance is high, the efficiency of voltage conversion decreases. Although the power consumption while a heating operation is high, it is possible to decrease overall consumption by pulse heating. Therefore, we can create a low-power system by keeping consumption during the idle state and the resistance readout operation. From all of the IC data sheets, a table of expected power consumption is created as shown in Table 5.4. The DC-DC converter has a shutdown function. It wakes up while the system is in “PMIC turn-on” and “heating” operations. The power efficiency depends on its load current, and it is assumed that the sensor resistance is 30 k Ω and the input power is 3 mW. DAC has also an enable pin. It is enabled at the same time as the PMIC. During the “heating” operation, ADC for reading and a current-sense amplifier are enabled. ADCs for “reading” and “heating” are

Table 5.4 Expected power-consumption during each operation according to IC data sheets.

	Idle	PMIC turn-on	Heating (9V)	Readout
DC-DC (BURST ON)	10 nA (Shutdown)	< 6mW	6 mW (Eff = 50%)	10 nA (Shutdown)
DAC	150nA (Power down)	60 μ A	60 μ A	150nA (Power down)
Current-Sense Amplifier	10 nA (Disabled)	10 nA (Disabled)	48 μ A	10 nA (Disabled)
ADC for heating	n/a	n/a	1 μ W	n/a
Zero-Drift OPA	90 nA (Shutdown)	90 nA (Shutdown)	90 nA (Shutdown)	7.5 μ A
ADC for reading	n/a	n/a	n/a	1 μ W
SPI->GPIO (Pull-up resistors)	13 μ A	13 μ A	13 μ A	13 μ A
PMIC's FB-resistors	3 μ A	3 μ A	3 μ A	3 μ A
Sensor bias creation	10 μ A	10 μ A	10 μ A	10 μ A
Sensor (30k)	n/a	n/a	3 mW	33 μ W

the same. Their sampling frequencies are different, but the power consumption at 10 kHz sampling frequency is written in the table. During the “reading” operation, a zero-drift amplifier and ADC for reading are enabled. Since a sensor is biased with 1 volt, 33 uW is consumed during the “reading” operation. An IO expansion is used to control GPIO pins via SPI. Its power consumption is dominated by pull-up resistors because the output of MAX7317 is open-drain. The value in the figure is calculated with the assumption that the pull-up resistors are 1 M Ω . If the pull-up resistances increase, HIGH-logic voltage decreases and the speed of the analog switches becomes slow. PMIC’s FB-resistors are used to control the output voltage of PMIC. This resistance affects the response speed of PMIC. Sensor bias creation is a voltage-divider circuit to create 1 V of biasing voltage. The large value of the resistance can become a noise source for sensor readout. According to the table, external resistors are mainly consuming power in the idle state, while in “heating” operation, power consumption is determined by DAC and PMIC, and in “reading” operation, sensor and external resistances dominate the overall power consumption.

The results of measurements of power consumption are shown in Table 5.5. Although the “PMIC turn-on” operation was not measured due to its difficulty, the power consumption of the other operations was measured. The period of one pulse was set to 100 ms because it takes around 6 ms until the output of the PID controller becomes stable. Also, the heated sensor resistance was the 12th, which resistance was 33.2 k Ω . The time of “reading” operation is determined by the RC

Table 5.5 Results of power consumption measurements.

	Idle	PMIC Turn-on	Heating (9V)	Reading
Time	n/a	n/a	100 ms per a pulse	50 us
Power Consumption $V_{in} = 3.3\text{ V}$	33.5 uA	n/a	43.9 mA (PWM) 6.27 mA (Burst)	71.1 uA

time constant of sensor resistance and parasitic capacitance. As expected, “idle” and “reading” operations do not spend power as much as the “heating” operation. Therefore, it is important to figure out how often “heating” is required and how long “heating” time is spared in the pulsed measurement.

5.4 Experimental Results

In Section 5.3, the performance of the interface circuit is discussed by using the dummy sensors. In this section the self-heated metal-oxide sensor is measured with the developed PCB and the constant-power and pulse-heating method is applied to the sensor. First of all, the experimental setup is explained. Since the sensor is still developing stage and high input power breaks the sensor itself, experiments were conducted while an external heater increased the ambient temperature up to 200 °C. Under the biased temperature condition, the sensor temperatures were controlled by self-heating. The major difference between the dummy sensor and the metal-oxide sensor in terms of developing PCB is that its load resistance gradually changes after the sensor surface is exposed to target molecules while sensor resistance is dynamically changing based on its self-heated temperature. To confirm that the PCB is operating properly, the constant power control is verified with the sensor. Then, experiments responding to two gases, N₂ and NO₂, were carried out.

5.4.1 Setup

Since the sensor cannot increase temperature up to 200-300 °C with only a self-heating effect, an external heater is placed below the sensor and ambient temperature is controlled. The sensor is heated by an external heater and self-heating. In Figure 5.24, the sensor connection is drawn. The mounting PCB called a “sensor board” has a hole for the sensor chip. The external heater is attached to the bottom of the PCB and the sensor chip is placed on the heater. Gold wires connect the PCB with the sensor chip and the heater. When using the external

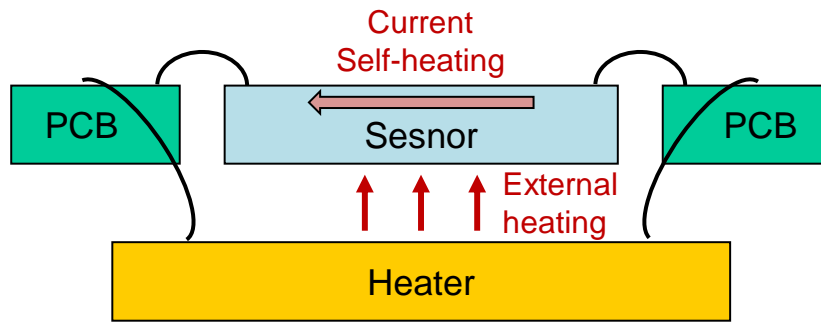


Figure 5.24 Sensor connection.

heater, every experiment starts a few minutes after the heater turns on. The photo of the experimental setup is shown in Figure 5.25. The sensor board is mounted on the controller board. The STM32 MCU is connected to a PC. There are two power lines: digital VDD (DVDD) and analog VDD (AVDD). DVDD is supplied from the PC through the MCU board. AVDD is supplied from a DC voltage source instrument. The sensor is as sensitive to molecule concentration as to gas flow. The effects appear as noise, and it is difficult to remove the noise by simple signal processing. To suppress this environmental noise, the sensors are covered by a chamber. The whole system including the power supply and PC is shown in Figure 5.26.

5.4.2 PID Control Monitor

To check the PID control with an actual sensor, data of the current readout ADC and the DAC are captured during the PID operation. It should be noted that accuracy is around 0.01-0.04 % to monitor heating current and around 0.5-1.5 % to monitor heating voltage as discussed in 5.3.3. For the test of the PID controller, target power is switched with a fixed period as the following sequence:

$$2.5 \text{ mW} \rightarrow 3 \text{ mW} \rightarrow 3.5 \text{ mW} \rightarrow 3 \text{ mW} \rightarrow 2.5 \text{ mW} \rightarrow 3 \text{ mW} \rightarrow \dots \quad (5.9)$$

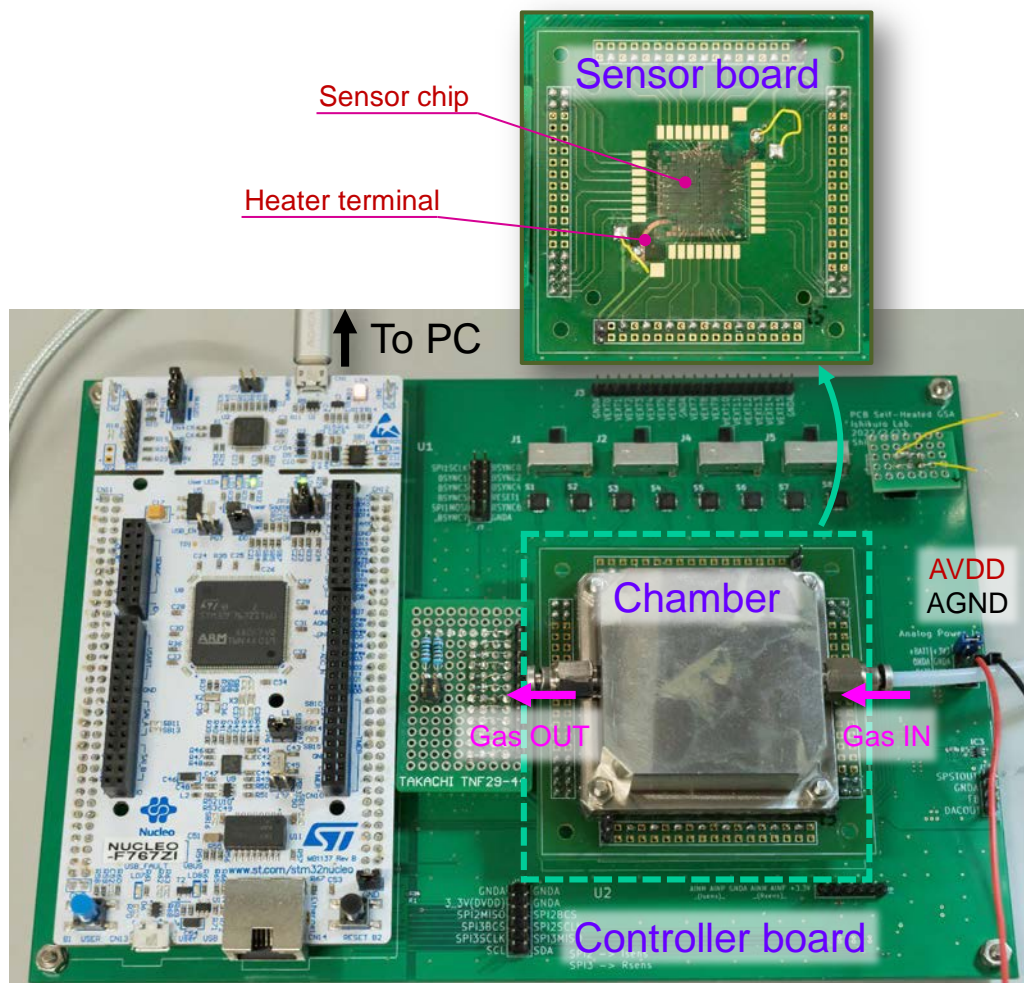


Figure 5.25 Experimental setup of PCB.

During this operation, the external heater was power-off. sensor resistance is also calculated with ADC and DAC values. The results of the monitor are shown in Figure 5.27(a). In this measurement, 10,000 data points are obtained in 15.4 sec. Its left axis expresses input power and the right axis expresses the resistance of the heated sensor. According to the graph, sensor resistance is changed depending on the input power, and the PID controller follows the resistance change. The plot data between 2.97-3.01 sec is zoomed as shown in Figure 5.27(b). The target power changed from 2.99 sec and the transition of the input power and sensor resistance starts at the same time. According to the graph, the input power reaches the target power within 8 msec. Since resistance fluctuation is larger than 1 % of

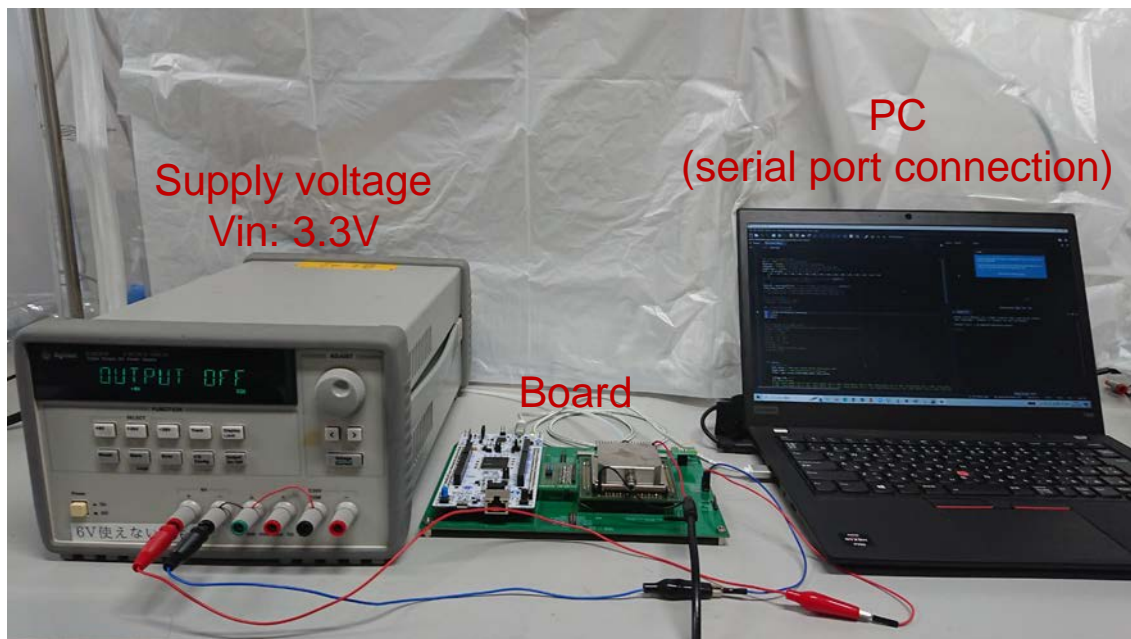


Figure 5.26 Overall experimental setup.

itself, it is assumed that this resistance change is caused by environmental noise. From the obtained results, it is concluded that the PID controller satisfactorily follows a rapid change of the sensor resistance and the time constant of the controller is almost the same as the results in which the dummy resistors are tested. Moreover, we can see that the thermal time constant of the sensor is faster than that of the controller.

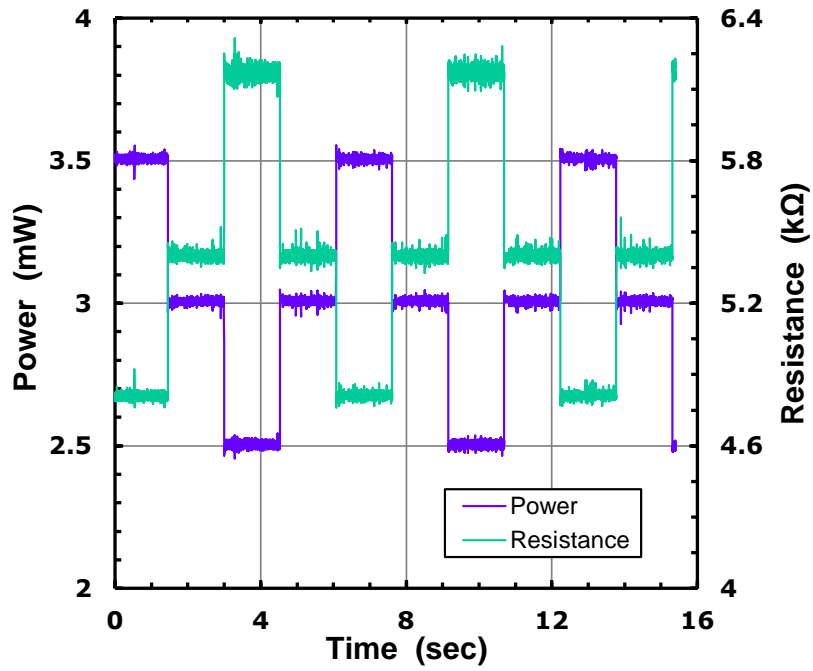
5.4.3 Sensor Measurement

Constant-power, pulse-heating measurements were conducted with the actual sensors. In this measurement, 16 sensors were implemented on the sensor board and target powers ranging between 2-6 mW were inputted. However, since developing sensors were still unstable and fragile, the same target power was set to multiple sensors and better sensors are selected. Relations between the sensor's position, resistance, and target power are shown in Table 5.6. In the table, it is shown that the sensors on the red-colored column are broken and those on the green-colored column are selected sensors.

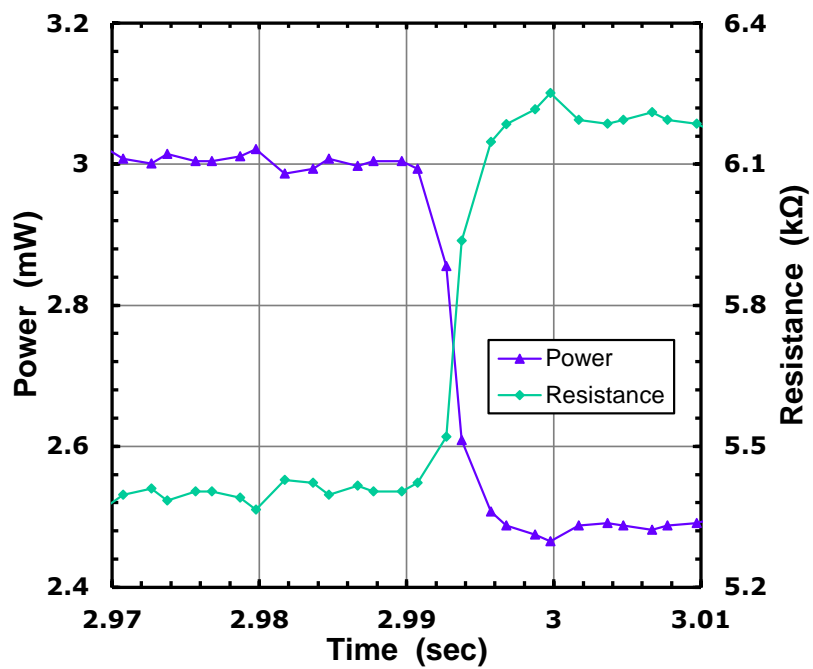
Table 5.6 Sensors' information used in the experiment about position, resistance, and target power.

Index (position)	0	1	2	3	4	5	6	7
Resistance (k Ω)	13.9	7.13	13.3	12.2	6.91	11.0	12.5	overflow
Power (mW)	4	6	5	5	3	6	6	0
Index (position)	8	9	10	11	12	13	14	15
Resistance (k Ω)	10.6	26.5	16.9	20.1	4.1	15.7	10.4	7.63
Power (mW)	5	5	2	3	4	4	2	6

To verify pulse-heated measurement, comparative experiments were conducted with a conventional continuous-heated method. Figure 5.28 shows measured data from the 2nd sensor. results. In the measurements, the sensors were always driven by pulse heating. The temperature of the external heater was kept at 200°C. Gas flow was controlled through gas-IN and gas-OUT holes on the chamber: At Time = 0, N₂ was filled with the chamber for about 180 secs, and at the same time, N₂ flows from the gas-IN hole. Then at around Time = 180 (sec), NO₂ flowed into the chamber from the gas-In hole. After NO₂ inflow, input gas was switched to N₂, and it was kept until Time = 400 (sec). As explained in Section 5.2, the sensor's resistance while heating is not measured by the readout circuit. Thus, this line plot shows measured data while the sensor is not biased. It is known that the resistance of the sensor decreases while the sensor is heated. The reason is that the heated temperature slowly decreases why measured resistance values increase right after the sensor is heated. It should be noted that the time constant of temperature change of the sensor is different between increasing and decreasing slopes. The sensor is heated every 15 readouts. The readout period is much shorter than the resistance response time to the molecules. Since it is assumed that the difference of the consecutive 15 data mainly expresses a temperature change of the sensors, the resistance plots are decimated to remove the change.



(a)



(b)

Figure 5.27 Measurement of monitoring the PID controller with an actual sensor.

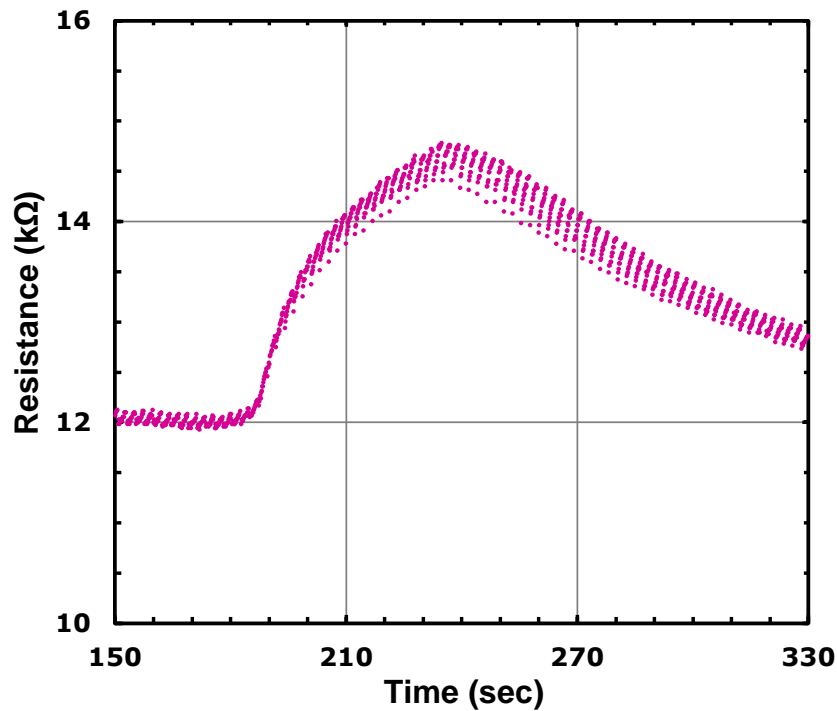
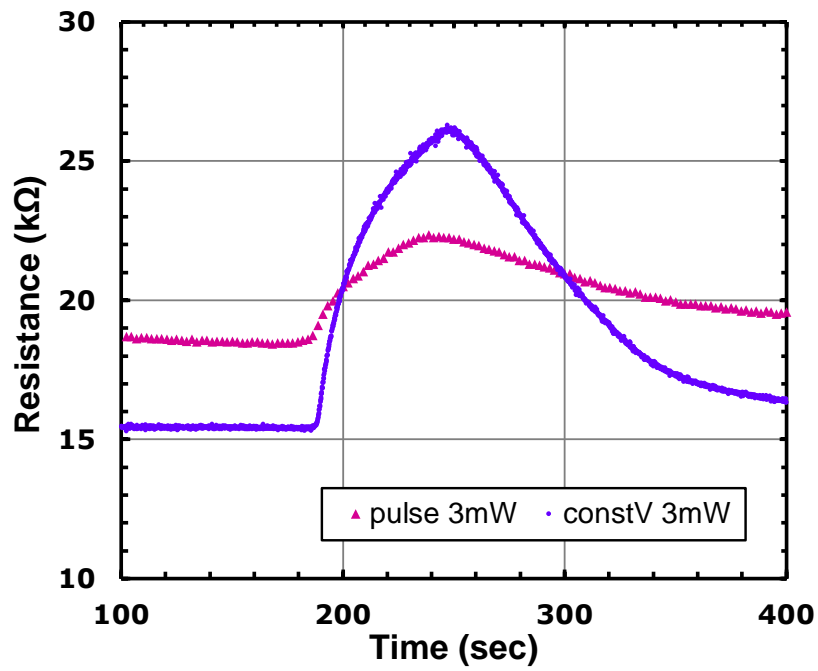


Figure 5.28 Measured resistance by pulse-heating measurement.

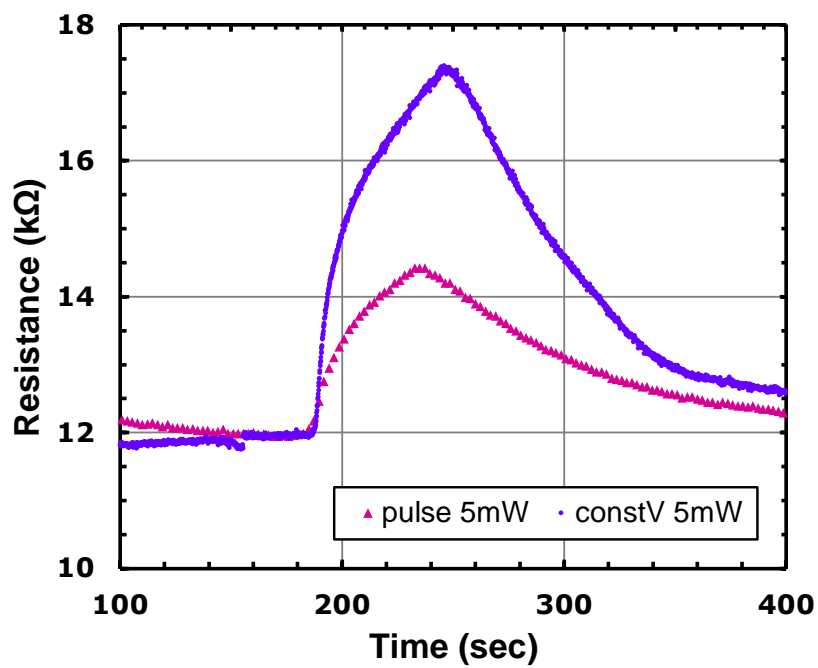
Continuous-heating measurement was carried out after the pulse-heating measurements to compare their results. The gas control was the same, and the input power to the sensor is controlled to keep constant power. Graphs for the comparison are shown in Figure 5.29. Since the sensors were not so stable that the continuous method overheated the sensor and some of the sensors were broken during measurements, the 2nd and 11th sensors are compared. According to the graph, the resistance of the sensor increases after the sensor is exposed to NO_2 . It is shown that sensor response to NO_2 is successfully obtained for both methods. Although measured sensitivity decreases in the pulse-heating method, the duty rate for max temperature and base temperature decreases to 1/16. It should be noticed that it is difficult to make surfaces of the sensors refreshed for all the measurements. In Figure 5.29(a), the baseline of the resistance was different before NO_2 comes, but this frequently occurred in these experiments. The main causes were considered that sensor characteristics were gradually changed due to exposure to surrounding gases and repetitive experiments. To

calibrate the base resistance change, the change rate of the resistance was normally recorded as the gas response rate.

Finally, sensitivity dependency on several input powers is testified using the pulse-heating measurement. As listed in Table 5.6, input powers ranged from 2 mW to 6 mW. Gas-flow control in the experiments was the same as the previous experiments. The 16 sensors were heated, and their resistances were measured for around 400 secs. The response results are shown in Figure 5.30. Since their base resistances were different from each other, the measured resistances were converted to their resistance change rate. In other words, resistance values just before NO₂ inflow were defined as 1, and other values are expressed as its ratio. The sensors properly operated were selected in the graph. According to the graph, the sensor response rate is highest when the input power is 4 mW, and the response rate gradually decreases as values of the input powers move from 4 mW increases. The difference of the output results shows the sensors at different temperature exhibited the temperature dependency of the metal-oxide sensor. Although the metal-oxide sensors were driven with pulse-heating, the measurement system achieved the sensor emulation.



(a)



(b)

Figure 5.29 Comparison results between the proposed pulse measurement and continuous measurement

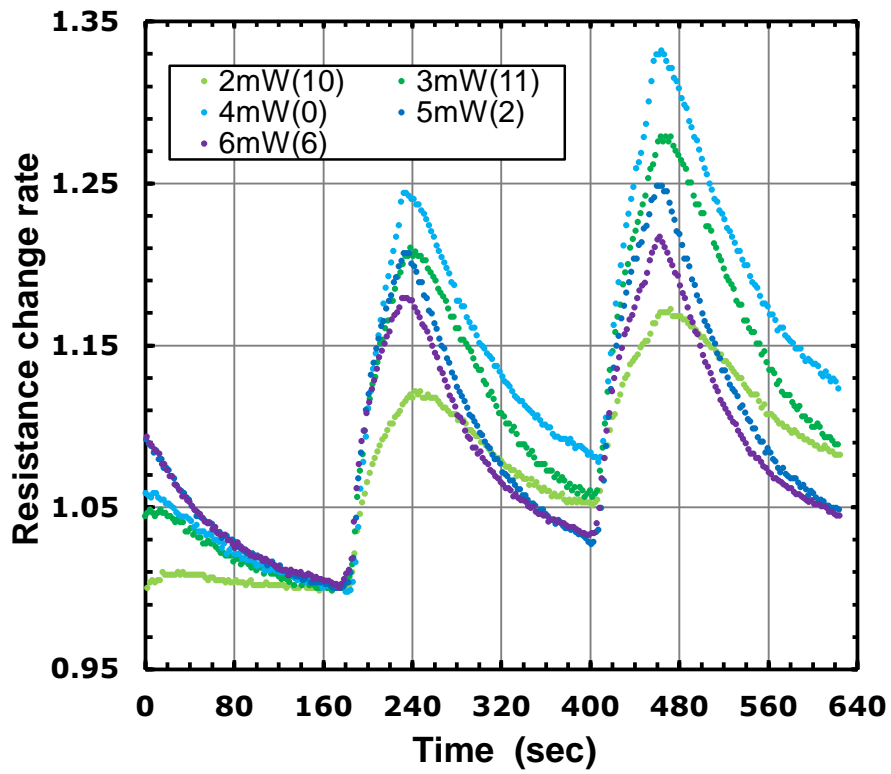


Figure 5.30 Sensor responses measured by the constant-power, pulse-heated measurement.

Chapter 6

Conclusion

In this chapter, we conclude this thesis with our future perspectives.

6.1 Thesis Summary

Artificial olfaction is applicable to wide range of solutions, as evident from past work examples. At the same time, these research achievements have shed light on the challenges of creating olfaction performance equivalent to that of mammals. As discussed in Chapter 1, an electronic nose is composed of sensors, interface circuits, and recognition algorithms. By examining the history of electronic nose implementation, it was discovered that there are significant challenges in integrating sensors on a large scale that corresponds to olfactory receptors in mammals; as well as in designing circuits and systems to extract data from these sensors. Towards the realization of an electronic nose, we proposed the concept of novel nose hardware. Research on circuits and systems for integrated metal-oxide sensors are conducted in parallel with the sensor research carried out by Yanagida Laboratory at the University of Tokyo. We addressed three research topics by subdividing the challenges of the novel nose hardware: compact model of self-heated metal-oxide sensors, readout circuits for a cross-point resistive array, and constant-power and pulse-measurement system for sensory emulation.

We worked on implementing a compact model for a self-heated metal-oxide sensor by advancing the simulation models of previously implemented metal-oxide gas sensors in Chapter 3. A new model was proposed embedding a feedback loop by self-heating effects. In addition, we assumed that the model parameters were determined without experimental results of self-heating effect. Thereby, the electrical characteristics of the static response gain was confirmed by the measurements using the external heater. Besides, thermal characteristics were obtained from the thermal simulations in COMSOL. Even though model parameters were fitted by the indirect method, the outputs of the compact model followed the sensor response affected by self-heating. It was also found that there was a relatively a large gap between the simulated resistance and a measured resistance due to a drift particularly when the sensor was operated in an inert gas.

To address the readout deterioration by sneak currents in a matrix sensor array, new readout methods were analyzed and proposed with MATLAB simulations in Chapter 4. It was discovered the op-amp nonidealities mostly affect the readout accuracy in the conventional VFMs or ZPMs from the simulation results. To eliminate the negative impacts from the op-amp, we proposed sneak-path-controlled readout (SPCR) and accurate SPCR (ASPCR). The methods relieved the tradeoff between circuit complexity and computational complexity. Although analog switches and a couple of ADCs were contained in the methods, SPCR with 12-bit ADC measured each resistance with less than 1 % error for a 32×32 resistive array. Since typical responses of metal-oxide sensors were around 10 % change in their resistance, we confirmed the SPCR had appropriated readout performance. For the various patterns of resistance distribution, ASPCR achieved more stable readout accuracy than SPCR in the sacrifice of an additional ADC.

The novel measurement system using integrated self-heated metal-oxide sensor was described in Chapter 5. Combining the techniques of the self-heated sensor, temperature modulation, and pulse-driven sensor, a novel sensory

emulating system was proposed. Inherently small-size and low-power system was achieved, and the experimental hardware was created as a proof-of-concept. The experimental results with a reactive gas, NO₂, showed that sensor behaviors were successfully changed under different temperatures. Additionally, it was observed that the sensitivity of the sensors was not degraded under pulse-heating operation. It was interesting discovery because the equivalent sensitivity was acquired even though the power consumption of the interface circuit was decreased. From the results, at least the equivalent sensitivity was obtained while the heating power was decreased down to 1/16 per channel.

These studies have provided clear prospects and feasibility towards the realization of artificial olfaction. This represents a significant step towards addressing the major challenge of artificial olfaction, which is the realization of olfactory hardware through large-scale integrated sensors. We believe that with the advancement of real-time data visualization for complex gases, it will lead to a broader research movement involving numerous data analysts.

6.2 Future Works

The research achievements in this work have enabled the creation of nose hardware capable of acquiring a vast amount of data using various sensors. Building upon these research achievements, future endeavors will focus on tackling more advanced challenges. Precisely, considering appropriate signal conditioning/processing will be desired. Securing stability of the sensor characteristics is one of the biggest topics. Even though metal-oxide sensors are more stable than polymer-based sensors, deterioration of sensor is a critical and unavoidable problem for long-term usage. The change in the characteristics of metal-oxide sensors is attributed to their oxidation and reduction of their surfaces caused by the influence of surrounding molecules such as oxygen and water vapor. Sensor designers will have strived to improve sensor materials for ensuring the stability of sensor characteristics. On the other hand, the development of remedial

techniques using signal processing is equally important. Besides, CMOS circuits exhibit a high affinity with signal processing. By achieving high integration and long-term stability simultaneously, we can approach the olfaction of the mammals. This leads to high reproducibility of data, contributing to the advancement of odor information science, which has been challenging for decades. In addition to this topic, future works are summarized the future research below:

- Creating platform for collecting massive data from the sensors.
- Exploration of signal conditioning/processing techniques for ensuring long-term stability and correcting fabricating variations of sensors.
- Exploration of classification algorithms to distinguish various odors.
- Realization of feedback system to adapt to surrounding environment by configuring sensor using temperature modulation.

In the pursuit of artificial olfaction research, one of the challenging aspects is dividing research areas. When the goal is to identify over 10,000 different odors, sensor designers face the difficulty of determining the number of sensors to integrate and selecting appropriate materials considering the trade-off between sensitivity and stability. For circuit designers, it is difficult to determine the readout accuracy of sensor response and how to drive the sensors, as these target specifications should be determined based on the identification accuracy achieved by the recognition algorithms. On the other hand, recognition algorithm designers would struggle with the variability of sensor data due to their reliance on the development-stage sensor data. It is important to have panoramic views and to enjoy studying while exploring new research areas.

References

- [1] R. W. Moncrieff, "An instrument for measuring and classifying odors," *J. Appl. Physiol.*, vol. 16, no. 4, pp. 742–749, Jul. 1961.
- [2] W. F. Wilkens and J. D. Hartman, "AN ELECTRONIC ANALOG FOR THE OLFACTORY PROCESSES," *Ann. N. Y. Acad. Sci.*, vol. 116, no. 2, pp. 608–612, Jul. 1964.
- [3] J. W. Gardner and P. N. Bartlett, "A brief history of electronic noses," *Sensors Actuators B Chem.*, vol. 18, no. 1–3, pp. 210–211, Mar. 1994.
- [4] K. Persaud and G. Dodd, "Analysis of discrimination mechanisms in the mammalian olfactory system using a model nose," *Nature*, vol. 299, no. 5881, pp. 352–355, Sep. 1982.
- [5] M. Kaneyasu, A. Ikegami, H. Arima, and S. Iwanaga, "Smell Identification Using a Thick-Film Hybrid Gas Sensor," *IEEE Trans. Components, Hybrids, Manuf. Technol.*, vol. 10, no. 2, pp. 267–273, Jun. 1987.
- [6] I. Akira and K. Masayoshi, "Olfactory detection using integrated sensors," in *International Conference on Solid-State Sensors and Actuators (Transducers '85)*, Philadelphia, PA. USA, 1985, pp. 136–139.
- [7] Y. Niimura and M. Nei, "Extensive Gains and Losses of Olfactory Receptor Genes in Mammalian Evolution," *PLoS One*, vol. 2, no. 8, p. e708, Aug. 2007.
- [8] L. B. Buck, "Unraveling the Sense of Smell (Nobel Lecture)," *Angew. Chemie Int. Ed.*, vol. 44, no. 38, pp. 6128–6140, Sep. 2005.
- [9] I. Gaillard, S. Rouquier, and D. Giorgi, "Olfactory receptors," *Cell. Mol. Life Sci.*, vol. 61, no. 4, pp. 456–469, Feb. 2004.
- [10] F. K. Che Harun, J. E. Taylor, J. A. Covington, and J. W. Gardner, "An electronic nose employing dual-channel odour separation columns with large chemosensor arrays for advanced odour discrimination," *Sensors Actuators B Chem.*, vol. 141, no. 1, pp. 134–140, Aug. 2009.
- [11] M. M. Mahmud, C. Seok, X. Wu, E. Sennik, A. O. Biliroglu, O. J. Adelegan, I. Kim, J. S. Jur, F. Y. Yamaner, and O. Oralkan, "A Low-Power Wearable E-Nose System Based on a Capacitive Micromachined Ultrasonic Transducer (CMUT) Array for Indoor VOC Monitoring," *IEEE Sens. J.*,

- vol. 21, no. 18, pp. 19684–19696, 2021.
- [12] J. Huang, N. Duan, P. Ji, C. Ma, F. Hu, Y. Ding, Y. Yu, Q. Zhou, and W. Sun, “A Crowdsourcing-Based Sensing System for Monitoring Fine-Grained Air Quality in Urban Environments,” *IEEE Internet Things J.*, vol. 6, no. 2, pp. 3240–3247, Apr. 2019.
- [13] P. Kumar, S. K. Mohanty, S. Guruswamy, Y. R. Smith, and M. Misra, “Detection of Food Decay Products Using Functionalized One-Dimensional Titania Nanotubular Arrays,” *IEEE Sensors Lett.*, vol. 1, no. 4, pp. 1–4, Aug. 2017.
- [14] K. R. Mallires, D. Wang, V. V. Tipparaju, and N. Tao, “Developing a Low-Cost Wearable Personal Exposure Monitor for Studying Respiratory Diseases Using Metal–Oxide Sensors,” *IEEE Sens. J.*, vol. 19, no. 18, pp. 8252–8261, Sep. 2019.
- [15] F. Tsow, E. Forzani, A. Rai, R. Wang, R. Tsui, S. Mastroianni, C. Knobbe, A. J. Gandolfi, and N. J. Tao, “A Wearable and Wireless Sensor System for Real-Time Monitoring of Toxic Environmental Volatile Organic Compounds,” *IEEE Sens. J.*, vol. 9, no. 12, pp. 1734–1740, Dec. 2009.
- [16] L. Dutta, C. Talukdar, A. Hazarika, and M. Bhuyan, “A Novel Low-Cost Hand-Held Tea Flavor Estimation System,” *IEEE Trans. Ind. Electron.*, vol. 65, no. 6, pp. 4983–4990, Jun. 2018.
- [17] C. Yan, A. Lu, and D. Song, “A Residual Dense Lightweight Group Convolution Neural Network for Identifying the Gas Information of Different Levels of Tea,” *IEEE Sens. J.*, vol. 23, no. 8, pp. 8138–8145, Apr. 2023.
- [18] H. Yu, J. Wang, H. Xiao, and M. Liu, “Quality grade identification of green tea using the eigenvalues of PCA based on the E-nose signals,” *Sensors Actuators B Chem.*, vol. 140, no. 2, pp. 378–382, Jul. 2009.
- [19] W. Zhang, T. Liu, A. Brown, M. Ueland, S. L. Forbes, and S. W. Su, “The Use of Electronic Nose for the Classification of Blended and Single Malt Scotch Whisky,” *IEEE Sens. J.*, vol. 22, no. 7, pp. 7015–7021, 2022.
- [20] K.-T. Tang, S.-W. Chiu, C.-H. Pan, H.-Y. Hsieh, Y.-S. Liang, and S.-C. Liu, “Development of a Portable Electronic Nose System for the Detection and Classification of Fruity Odors,” *Sensors*, vol. 10, no. 10, pp. 9179–9193, Oct. 2010.
- [21] M. J. Oates, J. D. Gonzalez-Teruel, M. C. Ruiz-Abellon, A. Guillamon-Frutos, J. A. Ramos, and R. Torres-Sanchez, “Using a Low-Cost Components e-Nose for Basic Detection of Different Foodstuffs,” *IEEE Sens. J.*, vol. 22, no. 14, pp. 13872–13881, Jul. 2022.
- [22] H. Li, Q. Chen, J. Zhao, and Q. Ouyang, “Non-destructive evaluation of pork freshness using a portable electronic nose (E-nose) based on a colorimetric sensor array,” *Anal. Methods*, vol. 6, no. 16, pp. 6271–6277, Aug. 2014.
- [23] J. Li, H. Feng, W. Liu, Y. Gao, and G. Hui, “Design of A Portable

- Electronic Nose system and Application in K Value Prediction for Large Yellow Croaker (*Pseudosciaena crocea*),” *Food Anal. Methods*, vol. 9, no. 10, pp. 2943–2951, Oct. 2016.
- [24] N. El Barbri, E. Llobet, N. El Bari, X. Correig, and B. Bouchikhi, “Application of a portable electronic nose system to assess the freshness of Moroccan sardines,” *Mater. Sci. Eng. C*, vol. 28, no. 5–6, pp. 666–670, Jul. 2008.
- [25] M. O’Connell, G. Valdora, G. Peltzer, and R. Martín Negri, “A practical approach for fish freshness determinations using a portable electronic nose,” *Sensors Actuators B Chem.*, vol. 80, no. 2, pp. 149–154, Nov. 2001.
- [26] G. Zambotti, M. Soprani, E. Gobbi, R. Capuano, V. Pasqualetti, C. Di Natale, and A. Ponzoni, “EARLY DETECTION OF FISH DEGRADATION BY ELECTRONIC NOSE,” in *2019 IEEE International Symposium on Olfaction and Electronic Nose (ISOEN)*, 2019, pp. 1–3.
- [27] H. GholamHosseini, D. Luo, H. Liu, and G. Xu, “Intelligent Processing of E-nose Information for Fish Freshness Assessment,” in *2007 3rd International Conference on Intelligent Sensors, Sensor Networks and Information*, 2007, pp. 173–177.
- [28] A. McWilliams, P. Beigi, A. Srinidhi, S. Lam, and C. E. MacAulay, “Sex and Smoking Status Effects on the Early Detection of Early Lung Cancer in High-Risk Smokers Using an Electronic Nose,” *IEEE Trans. Biomed. Eng.*, vol. 62, no. 8, pp. 2044–2054, Aug. 2015.
- [29] Shih-Wen Chiu, Jen-Huo Wang, Kwang-Han Chang, Ting-Hau Chang, Chia-Min Wang, Chia-Lin Chang, Chen-Ting Tang, Chien-Fu Chen, Chung-Hung Shih, Han-Wen Kuo, Li-Chun Wang, Hsin Chen, Chih-Cheng Hsieh, Meng-Fan Chang, Yi-Wen Liu, Tsan-Jieh Chen, Chia-Hsiang Yang, Herming Chiueh, Juyo-Min Shyu, and Kea-Tiong Tang, “A Fully Integrated Nose-on-a-Chip for Rapid Diagnosis of Ventilator-Associated Pneumonia,” *IEEE Trans. Biomed. Circuits Syst.*, vol. 8, no. 6, pp. 765–778, Dec. 2014.
- [30] V. S. Kodogiannis, J. N. Lygouras, A. Tarczynski, and H. S. Chowdrey, “Artificial Odor Discrimination System Using Electronic Nose and Neural Networks for the Identification of Urinary Tract Infection,” *IEEE Trans. Inf. Technol. Biomed.*, vol. 12, no. 6, pp. 707–713, Nov. 2008.
- [31] T. Tanaka, T. Yanagida, K. Uchida, K. Tabuchi, K. Tatehara, Y. Shiiki, S. Nakagawa, T. Takahashi, R. Shimizu, H. Ishikuro, and T. Kuroda, “Low-Power and ppm-Level Multimolecule Detection by Integration of Self-Heated Metal Nanosheet Sensors,” *IEEE Trans. Electron Devices*, vol. 66, no. 12, pp. 5393–5398, Dec. 2019.
- [32] L. Díaz de León-Martínez, R. Flores-Ramírez, C. M. López-Mendoza, M. Rodríguez-Aguilar, G. Metha, L. Zúñiga-Martínez, O. Ornelas-Rebolledo, and L. E. Alcántara-Quintana, “Identification of volatile organic compounds in the urine of patients with cervical cancer. Test concept for timely screening,” *Clin. Chim. Acta*, vol. 522, no. August, pp. 132–140,

- Nov. 2021.
- [33] H.-Y. Yang, Y.-C. Wang, H.-Y. Peng, and C.-H. Huang, “Breath biopsy of breast cancer using sensor array signals and machine learning analysis,” *Sci. Rep.*, vol. 11, no. 1, p. 103, Jan. 2021.
 - [34] Z. Haddi, A. Amari, H. Alami, N. El Bari, E. Llobet, and B. Bouchikhi, “A portable electronic nose system for the identification of cannabis-based drugs,” *Sensors Actuators B Chem.*, vol. 155, no. 2, pp. 456–463, Jul. 2011.
 - [35] D. Matatagui, F. A. Bahos, I. Gràcia, and M. D. C. Horrillo, “Portable Low-Cost Electronic Nose Based on Surface Acoustic Wave Sensors for the Detection of BTX Vapors in Air,” *Sensors*, vol. 19, no. 24, p. 5406, Dec. 2019.
 - [36] A. Nake, B. Dubreuil, C. Raynaud, and T. Talou, “Outdoor in situ monitoring of volatile emissions from wastewater treatment plants with two portable technologies of electronic noses,” *Sensors Actuators B Chem.*, vol. 106, no. 1, pp. 36–39, Apr. 2005.
 - [37] S. Fuchs, P. Strobel, M. Siadat, and M. Lumbreras, “Evaluation of unpleasant odor with a portable electronic nose,” *Mater. Sci. Eng. C*, vol. 28, no. 5–6, pp. 949–953, Jul. 2008.
 - [38] F. C. Tian, C. Kadri, L. Zhang, J. W. Feng, L. H. Juan, and P. L. Na, “A Novel Cost-Effective Portable Electronic Nose for Indoor-/In-Car Air Quality Monitoring,” in *2012 International Conference on Computer Distributed Control and Intelligent Environmental Monitoring*, 2012, pp. 4–8.
 - [39] H.-K. Hong, C. H. Kwon, S.-R. Kim, D. H. Yun, K. Lee, and Y. K. Sung, “Portable electronic nose system with gas sensor array and artificial neural network,” *Sensors Actuators B Chem.*, vol. 66, no. 1–3, pp. 49–52, Jul. 2000.
 - [40] Qi Wang, Kai Song, and Tiandong Guo, “Portable Vehicular Electronic Nose System for Detection of Automobile Exhaust,” in *2010 IEEE Vehicle Power and Propulsion Conference*, 2010, pp. 1–5.
 - [41] B. Charumporn, S. Omatu, M. Yoshioka, T. Fujinaka, and T. Kosaka, “Fire Detection Systems by Compact Electronic Nose Systems Using Metal Oxide Gas Sensors,” in *2004 IEEE International Joint Conference on Neural Networks*, Budapest, Hungary, 2004, pp. 1317–1320.
 - [42] G. Gong and H. Zhu, “A portable embedded explosion gas detection and identification device based on intelligent electronic nose system,” *Sens. Rev.*, vol. 36, no. 1, pp. 57–63, Jan. 2016.
 - [43] R. Rousier, S. Bouat, T. Bordy, H. Grateau, M. Darboux, J. Hue, G. Gaillard, S. Besnard, F. Veignal, P. Montméat, G. Lebrun, and A. Larue, “T-REX: a portable device to detect and identify explosives vapors,” *Procedia Eng.*, vol. 47, pp. 390–393, 2012.
 - [44] “PEN3 Portable Electronic Nose,” *Airsense Analytics GmbH*. [Online]. Available: https://airsense.com/sites/default/files/flyer_pen.pdf.

- [45] M. Cole, J. . Gardner, A. W. . Lim, P. . Scivier, and J. . Brignell, “Polymeric resistive bridge gas sensor array driven by a standard cell CMOS current drive chip,” *Sensors Actuators B Chem.*, vol. 58, no. 1–3, pp. 518–525, Sep. 1999.
- [46] J. W. Gardner, M. Vidic, P. Ingleby, A. C. Pike, J. E. Brignell, P. Scivier, P. N. Bartlett, A. J. Duke, and J. M. Elliott, “Response of a poly(pyrrole) resistive micro-bridge to ethanol vapour,” *Sensors Actuators B Chem.*, vol. 48, no. 1–3, pp. 289–295, May 1998.
- [47] J. García-Guzmán, N. Ulivieri, M. Cole, and J. W. Gardner, “Design and simulation of a smart ratiometric ASIC chip for VOC monitoring,” *Sensors Actuators B Chem.*, vol. 95, no. 1–3, pp. 232–243, Oct. 2003.
- [48] J. García-Guzmán, J. W. Gardner, and M. Cole, “A duo-type smart gas sensor ASIC chip for use with resistive nanomaterials,” *Procedia Eng.*, vol. 5, pp. 176–179, 2010.
- [49] R. Perello-Roig, J. Verd, S. Bota, and J. Segura, “Resonant Inertial Mass Sensing for VOCs—CMOS-Compatible SoC Integration Advantages and Challenges: A Review,” *IEEE Sens. J.*, vol. 23, no. 1, pp. 34–52, Jan. 2023.
- [50] C. Hagleitner, D. Lange, A. Hierlemann, O. Brand, and H. Baltes, “CMOS Single-Chip Gas Detection System Comprising Capacitive, Calorimetric and Mass-Sensitive Microsensors,” *IEEE J. Solid-State Circuits*, vol. 37, no. 12, pp. 1867–1878, Dec. 2002.
- [51] C. Hagleitner, A. Hierlemann, D. Lange, A. Kummer, N. Kerness, O. Brand, and H. Baltes, “Smart single-chip gas sensor microsystem,” *Nature*, vol. 414, no. 6861, pp. 293–296, Nov. 2001.
- [52] D. M. Karabacak, Ling Sieben-Xu, M. Vandecasteele, Y. van Andel, D. Wouters, M. C. Calama, and S. H. Brongersma, “Toward a Miniaturized Low-Power Micromechanical Electronic Nose,” *IEEE Sens. J.*, vol. 12, no. 11, pp. 3184–3188, Nov. 2012.
- [53] J. Pettine, V. Petrescu, D. M. Karabacak, M. Vandecasteele, M. Crego-Calama, and C. Van Hoof, “Power-Efficient Oscillator-Based Readout Circuit for Multichannel Resonant Volatile Sensors,” *IEEE Trans. Biomed. Circuits Syst.*, vol. 6, no. 6, pp. 542–551, Dec. 2012.
- [54] V. Petrescu, J. Pettine, D. M. Karabacak, M. Vandecasteele, M. C. Calama, and C. Van Hoof, “Power-Efficient Readout Circuit for Miniaturized Electronic Nose,” in *IEEE International Solid-State Circuits Conference*, 2012, pp. 318–320.
- [55] A. K. Murray, J. R. Meseke, N. Bajaj, and J. F. Rhoads, “Addressing the Practical Limitations of Volatile Organic Compound Sensors Through an Oscillator-Based Sensing Array,” *IEEE Sens. J.*, vol. 21, no. 2, pp. 2169–2175, Jan. 2021.
- [56] K.-T. Tang and R. M. Goodman, “Electronic Olfaction System on a Chip,” in *SCI2001/ISAS2001 International Conference on Information Systems*, 2001.

- [57] K.-T. Tang, S.-W. Chiu, M.-F. Chang, C.-C. Hsieh, and J.-M. Shyu, "A Low-Power Electronic Nose Signal-Processing Chip for a Portable Artificial Olfaction System," *IEEE Trans. Biomed. Circuits Syst.*, vol. 5, no. 4, pp. 380–390, Aug. 2011.
- [58] C.-P. Chang and C.-L. Yuan, "The fabrication of a MWNTs–polymer composite chemoresistive sensor array to discriminate between chemical toxic agents," *J. Mater. Sci.*, vol. 44, no. 20, pp. 5485–5493, Oct. 2009.
- [59] K.-T. Tang, S.-W. Chiu, M.-F. Chang, C.-C. Hsieh, and J.-M. Shyu, "A Wearable Electronic Nose SoC for Healthier Living," in *2011 IEEE Biomedical Circuits and Systems Conference (BioCAS)*, 2011, pp. 293–296.
- [60] T.-I. Chou, S.-W. Chiu, K.-H. Chang, Y.-J. Chen, C.-T. Tang, C.-H. Shih, C.-C. Hsieh, M.-F. Chang, C.-H. Yang, H. Chiueh, and K.-T. Tang, "Design of a 0.5 V 1.68mW nose-on-a-chip for rapid screen of chronic obstructive pulmonary disease," in *2016 IEEE Biomedical Circuits and Systems Conference (BioCAS)*, 2016, pp. 592–595.
- [61] J. Wang, J. Yang, D. Chen, L. Jin, Y. Li, Y. Zhang, L. Xu, Y. Guo, F. Lin, and F. Wu, "Gas Detection Microsystem With MEMS Gas Sensor and Integrated Circuit," *IEEE Sens. J.*, vol. 18, no. 16, pp. 6765–6773, Aug. 2018.
- [62] T.-I. Chou, K.-H. Chang, J.-Y. Jhang, S.-W. Chiu, G. Wang, C.-H. Yang, H. Chiueh, H. Chen, C.-C. Hsieh, M.-F. Chang, and K.-T. Tang, "A 1-V 2.6-mW Environmental Compensated Fully Integrated Nose-on-a-Chip," *IEEE Trans. Circuits Syst. II Express Briefs*, vol. 65, no. 10, pp. 1365–1369, Oct. 2018.
- [63] T. J. Koickal, A. Hamilton, T. C. Pearce, S. L. Tan, J. A. Covington, and J. W. Gardner, "Analog VLSI Design of an Adaptive Neuromorphic Chip for Olfactory Systems," in *2006 IEEE International Symposium on Circuits and Systems*, 2006, vol. 1, pp. 4547–4550.
- [64] H. S. Abdel-Aty-Zohdy, J. N. Allen, and R. L. Ewing, "Spiking Neural Network E-Nose Classifier Chip," in *Proceedings of the IEEE 2010 National Aerospace & Electronics Conference*, 2010, pp. 374–378.
- [65] K. T. Ng, F. Boussaid, and A. Bermak, "A CMOS Single-Chip Gas Recognition Circuit for Metal Oxide Gas Sensor Arrays," *IEEE Trans. Circuits Syst. I Regul. Pap.*, vol. 58, no. 7, pp. 1569–1580, Jul. 2011.
- [66] Hung-Yi Hsieh and Kea-Tiong Tang, "VLSI Implementation of a Bio-Inspired Olfactory Spiking Neural Network," *IEEE Trans. Neural Networks Learn. Syst.*, vol. 23, no. 7, pp. 1065–1073, Jul. 2012.
- [67] N. Imam, T. A. Cleland, R. Manohar, P. A. Merolla, J. V. Arthur, F. Akopyan, and D. S. Modha, "Implementation of Olfactory Bulb Glomerular-Layer Computations in a Digital Neurosynaptic Core," *Front. Neurosci.*, vol. 6, no. JUN, pp. 1–13, 2012.
- [68] H.-Y. Hsieh and K.-T. Tang, "An on-chip learning, low-power probabilistic spiking neural network with long-term memory," in *2013 IEEE Biomedical*

- Circuits and Systems Conference (BioCAS)*, 2013, pp. 5–8.
- [69] P.-C. Huang and J. M. Rabaey, “A Bio-Inspired Analog Gas Sensing Front End,” *IEEE Trans. Circuits Syst. I Regul. Pap.*, vol. 64, no. 9, pp. 2611–2623, Sep. 2017.
- [70] H. Chen, D. Huo, and J. Zhang, “Gas Recognition in E-Nose System: A Review,” *IEEE Trans. Biomed. Circuits Syst.*, vol. 16, no. 2, pp. 169–184, Apr. 2022.
- [71] J. Yun, M. Cho, K. Lee, M. Kang, and I. Park, “A review of nanostructure-based gas sensors in a power consumption perspective,” *Sensors Actuators B Chem.*, vol. 372, no. August, p. 132612, 2022.
- [72] S. Y. Park, Y. Kim, T. Kim, T. H. Eom, S. Y. Kim, and H. W. Jang, “Chemoresistive materials for electronic nose: Progress, perspectives, and challenges,” *InfoMat*, vol. 1, no. 3, pp. 289–316, Sep. 2019.
- [73] B. Tise, “A compact high resolution piezoresistive digital tactile sensor,” in *Proceedings. 1988 IEEE International Conference on Robotics and Automation*, 1988, pp. 760–764.
- [74] J. Liang, J. Wu, H. Huang, W. Xu, B. Li, and F. Xi, “Soft Sensitive Skin for Safety Control of a Nursing Robot Using Proximity and Tactile Sensors,” *IEEE Sens. J.*, pp. 1–1, Dec. 2019.
- [75] P. T. Hoang, H. Phung, C. T. Nguyen, T. Dat Nguyen, and H. R. Choi, “A Highly Flexible, Stretchable and Ultra-thin Piezoresistive Tactile Sensor Array using PAM/PEDOT:PSS,” in *2017 14th International Conference on Ubiquitous Robots and Ambient Intelligence, URAI 2017*, 2017, pp. 950–955.
- [76] S. Yue and W. A. Moussa, “A Piezoresistive Tactile Sensor Array for Touchscreen Panels,” *IEEE Sens. J.*, vol. 18, no. 4, pp. 1685–1693, Feb. 2018.
- [77] Y.-J. Yang, M.-Y. Cheng, S.-C. Shih, X.-H. Huang, C.-M. Tsao, F.-Y. Chang, and K.-C. Fan, “A 32×32 temperature and tactile sensing array using PI-copper films,” *Int. J. Adv. Manuf. Technol.*, vol. 46, no. 9–12, pp. 945–956, Feb. 2010.
- [78] S. Y. Hong, Y. H. Lee, H. Park, S. W. Jin, Y. R. Jeong, J. Yun, I. You, G. Zi, and J. S. Ha, “Stretchable Active Matrix Temperature Sensor Array of Polyaniline Nanofibers for Electronic Skin,” *Adv. Mater.*, vol. 28, no. 5, pp. 930–935, Feb. 2016.
- [79] M. Bernabei, K. C. Persaud, S. Pantalei, E. Zampetti, and R. Beccherelli, “Large-Scale Chemical Sensor Array Testing Biological Olfaction Concepts,” *IEEE Sens. J.*, vol. 12, no. 11, pp. 3174–3183, 2012.
- [80] N. Shinmyo, T. Iwata, K. Hashizume, K. Kuroki, and K. Sawada, “Development of potentiometric miniature gas sensor arrays feasible for small olfactory chips and gas recognition from their response patterns,” in *2017 IEEE SENSORS*, Glasgow, Scotland, UK, 2017, pp. 1–3.
- [81] A. Serb, W. Redman-White, C. Papavassiliou, and T. Prodromakis,

- “Practical Determination of Individual Element Resistive States in Selectorless RRAM Arrays,” *IEEE Trans. Circuits Syst. I Regul. Pap.*, vol. 63, no. 6, pp. 827–835, 2016.
- [82] A. Serb, W. Redman-White, C. Papavassiliou, R. Berdan, and T. Prodromakis, “Limitations and precision requirements for read-out of passive, linear, selectorless RRAM arrays,” *Proc. - IEEE Int. Symp. Circuits Syst.*, vol. 2015-July, pp. 189–192, 2015.
- [83] Y. Youn, K. Kim, J. Y. Sim, H. J. Park, and B. Kim, “Investigation on the Worst Read Scenario of a ReRAM Crossbar Array,” *IEEE Trans. Very Large Scale Integr. Syst.*, vol. 25, no. 9, pp. 2402–2410, 2017.
- [84] M. Cicioni, L. Bissi, P. Placidi, A. Shehu, A. Scorzoni, E. Cozzani, I. Elmi, S. Zampolli, and G. C. Cardinali, “Interface circuit for an ultra low power gas sensor,” in *International Instrumentation and Measurement Technology Conference*, Singapore, Singapore, 2009.
- [85] L. Bissi, M. Cicioni, P. Placidi, S. Zampolli, I. Elmi, and A. Scorzoni, “A Programmable Interface Circuit for an Ultralow Power Gas Sensor,” *IEEE Trans. Instrum. Meas.*, vol. 60, no. 1, pp. 282–289, Jan. 2011.
- [86] H. Liu, Y.-F. Zhang, Y.-W. Liu, and M.-H. Jin, “Measurement errors in the scanning of resistive sensor arrays,” *Sensors Actuators A Phys.*, vol. 163, no. 1, pp. 198–204, Sep. 2010.
- [87] R. Yarahmadi, A. Safarpour, and R. Lotfi, “An Improved-Accuracy Approach for Readout of Large-Array Resistive Sensors,” *IEEE Sens. J.*, vol. 16, no. 1, pp. 210–215, 2016.
- [88] J. A. Hidalgo-Lopez, J. Romero-Sanchez, and R. Fernandez-Ramos, “New Approaches for Increasing Accuracy in Readout of Resistive Sensor Arrays,” *IEEE Sens. J.*, vol. 17, no. 7, pp. 2154–2164, Apr. 2017.
- [89] Y. Shiiki and H. Ishikuro, “Interface with Opamp Output-Impedance Calibration Technique for a Large Integrated 2-D Resistive Sensor Array,” in *2019 IEEE International Symposium on Circuits and Systems (ISCAS)*, Sapporo, Japan, 2019.
- [90] Y. Shiiki and H. Ishikuro, “Simulation and Calibration of Op-Amp Nonidealities in the Voltage Feedback Method for a Cross-Point Resistive Sensor Array,” *IEEE Sens. J.*, vol. 21, no. 15, pp. 16790–16797, 2021.
- [91] H. Alirezaei, A. Nagakubo, and Y. Kuniyoshi, “A Tactile Distribution Sensor Which Enables Stable Measurement Under High and Dynamic Stretch,” in *2009 IEEE Symposium on 3D User Interfaces*, 2009, pp. 87–93.
- [92] F. Lorussi, W. Rocchia, E. P. Scilingo, A. Tognetti, and D. De Rossi, “Wearable, Redundant Fabric-Based Sensor Arrays for Reconstruction of Body Segment Posture,” *IEEE Sens. J.*, vol. 4, no. 6, pp. 807–818, Dec. 2004.
- [93] Lin Shu, Xiaoming Tao, and D. D. Feng, “A New Approach for Readout of Resistive Sensor Arrays for Wearable Electronic Applications,” *IEEE Sens.*

- J.*, vol. 15, no. 1, pp. 442–452, Jan. 2015.
- [94] J. A. H. Lopez, O. Oballe-Peinado, and J. A. Sanchez-Duran, “A Proposal to Eliminate the Impact of Crosstalk on Resistive Sensor Array Readouts,” *IEEE Sens. J.*, vol. 20, no. 22, pp. 13461–13470, Nov. 2020.
- [95] Y. Shiiki and H. Ishikuro, “A High Accuracy Opamp-less Interface Circuit for 2-D Cross-Point Resistive Sensor Array with Switch Resistance Calibration,” in *2019 IEEE Asia Pacific Conference on Circuits and Systems (APCCAS)*, 2019, pp. 105–108.
- [96] T. Tanaka, K. Tabuchi, K. Tatehara, Y. Shiiki, S. Nakagawa, T. Takahashi, R. Shimizu, H. Ishikuro, T. Kuroda, T. Yanagida, and K. Uchida, “Low-Power and ppm-Level Detection of Gas Molecules by Integrated Metal Nanosheets,” in *2019 Symposium on VLSI Circuits*, 2019, vol. 2019-June, pp. T158–T159.
- [97] H. Liu, Y. He, K. Nagashima, G. Meng, T. Dai, B. Tong, Z. Deng, S. Wang, N. Zhu, T. Yanagida, and X. Fang, “Discrimination of VOCs molecules via extracting concealed features from a temperature-modulated p-type NiO sensor,” *Sensors Actuators B Chem.*, vol. 293, no. January, pp. 342–349, Aug. 2019.
- [98] H. Liu, G. Meng, Z. Deng, K. Nagashima, S. Wang, T. Dai, L. Li, T. Yanagida, and X. Fang, “Discriminating BTX Molecules by the Nonselective Metal Oxide Sensor-Based Smart Sensing System,” *ACS Sensors*, vol. 6, no. 11, pp. 4167–4175, 2021.
- [99] F. Hossein-Babaei and A. Amini, “A breakthrough in gas diagnosis with a temperature-modulated generic metal oxide gas sensor,” *Sensors Actuators B Chem.*, vol. 166–167, pp. 419–425, May 2012.
- [100] C. Seok, M. M. Mahmud, M. Kumar, O. J. Adelegan, F. Y. Yamaner, and O. Oralkan, “A Low-Power Wireless Multichannel Gas Sensing System Based on a Capacitive Micromachined Ultrasonic Transducer (CMUT) Array,” *IEEE Internet Things J.*, vol. 6, no. 1, pp. 831–843, Feb. 2019.
- [101] B. Lee, M. Lim, and V. Misra, “Wearable skin vapor sensing system for continuous monitoring of various health and lifestyles,” in *2021 IEEE Sensors*, 2021, vol. 2021-October, pp. 1–4.
- [102] H. Y. Chae, J. Cho, R. Purbia, C. S. Park, H. Kim, Y. Lee, J. M. Baik, and J. J. Kim, “Environment-Adaptable Edge-Computing Gas Sensor Device with Analog-Assisted Continual Learning Scheme,” *IEEE Trans. Ind. Electron.*, 2022.
- [103] K. Park, S. Choi, H. Y. Chae, C. S. Park, S. Lee, Y. Lim, H. Shin, and J. J. Kim, “An Energy-Efficient Multimode Multichannel Gas-Sensor System With Learning-Based Optimization and Self-Calibration Schemes,” *IEEE Trans. Ind. Electron.*, vol. 67, no. 3, pp. 2402–2410, Mar. 2020.
- [104] A. Dey, “Semiconductor metal oxide gas sensors: A review,” *Mater. Sci. Eng. B*, vol. 229, no. November 2017, pp. 206–217, Mar. 2018.
- [105] H. Honda, T. Takahashi, Y. Shiiki, H. Zeng, K. Nakamura, S. Nagata, T.

- Hosomi, W. Tanaka, G. Zhang, M. Kanai, K. Nagashima, H. Ishikuro, and T. Yanagida, "Impact of Lateral SnO₂ Nanofilm Channel Geometry on a 1024 Crossbar Chemical Sensor Array," *ACS Sensors*, vol. 7, no. 2, pp. 460–468, Feb. 2022.
- [106] H. Ji, C. Mi, Z. Yuan, Y. Liu, H. Zhu, and F. Meng, "Multicomponent Gas Detection Method via Dynamic Temperature Modulation Measurements Based on Semiconductor Gas Sensor," *IEEE Trans. Ind. Electron.*, vol. 70, no. 6, pp. 6395–6404, Jun. 2023.
- [107] G. Meng, F. Zhuge, K. Nagashima, A. Nakao, M. Kanai, Y. He, M. Boudot, T. Takahashi, K. Uchida, and T. Yanagida, "Nanoscale Thermal Management of Single SnO₂ Nanowire: pico-Joule Energy Consumed Molecule Sensor," *ACS Sensors*, vol. 1, no. 8, pp. 997–1002, Aug. 2016.
- [108] J. Yun, C. Y. Jin, J.-H. Ahn, S. Jeon, and I. Park, "A self-heated silicon nanowire array: selective surface modification with catalytic nanoparticles by nanoscale Joule heating and its gas sensing applications," *Nanoscale*, vol. 5, no. 15, p. 6851, 2013.
- [109] F. Palacio, J. Fonollosa, J. Burgues, J. M. Gomez, and S. Marco, "Pulsed-temperature metal oxide gas sensors for microwatt power consumption," *IEEE Access*, vol. 8, pp. 70938–70946, 2020.
- [110] K. Suematsu, W. Harano, T. Oyama, Y. Shin, K. Watanabe, and K. Shimano, "Pulse-Driven Semiconductor Gas Sensors Toward ppt Level Toluene Detection," *Anal. Chem.*, vol. 90, no. 19, pp. 11219–11223, Oct. 2018.
- [111] E. Llobet, X. Vilanova, J. Brezmes, D. López, and X. Correig, "Electrical equivalent models of semiconductor gas sensors using PSpice," *Sensors Actuators, B Chem.*, vol. 77, no. 1–2, pp. 275–280, 2001.
- [112] H. Zeng, T. Takahashi, M. Kanai, G. Zhang, Y. He, K. Nagashima, and T. Yanagida, "Long-Term Stability of Oxide Nanowire Sensors via Heavily Doped Oxide Contact," *ACS Sensors*, vol. 2, no. 12, pp. 1854–1859, Dec. 2017.
- [113] "Data Sheet ADG1438/ADG1439," *Analog Devices Inc.* [Online]. Available: <https://www.analog.com/jp/products/adg1439.html>.
- [114] "Data Sheet ADG726/ADG732," *Analog Devices Inc.* [Online]. Available: <https://www.analog.com/jp/products/adg726.html>.
- [115] "DATA SHEET 34410A and 34411A Multimeters," *Keysight Technologies.* [Online]. Available: <https://www.keysight.com/jp/ja/product/34410A/digital-multimeter-6-digit.html>.
- [116] "Data Sheet LTC3129," *Analog Devices Inc.* [Online]. Available: <https://www.analog.com/jp/products/ltc3129.html>.